# New U-Th/Pb constraints on timing of shearing and long-term slip-rate on the Karakorum fault.

Franck Valli (1), Philippe Hervé Leloup (2), Jean-Louis Paquette (3), Nicolas Arnaud (4), Haibing Li (1-5), Paul Tapponnier (1), Robin Lacassin (1), Stéphane Guillot (6),Dunyi Liu (5), Etienne Deloule (7), Zhiqin Xu (5), Gweltaz Mahéo (2).

(1) Laboratoire de mécanique de la lithosphère, Institut de Physique du Globe de Paris, CNRS UMR 75252, Paris, France, (2) Laboratoire des sciences de la terre, CNRS UMR5570, Université de Lyon, 69622, Villeurbanne, France, (3) Laboratoire magmas et volcans, CNRS UMR 6524- université Blaise Pascal, 63038 Clermont-Ferrand, France, (4) Géosciences Montpellier, Université Montpellier 2, CNRS UMR 5243, 34095, Montpellier, France (5) Institute of Geology CAGS, 100037, Beijing, China, (6) Laboratoire de géologie des chaînes alpines, CNRS UMR 5025 Université de Grenoble 38031 Grenoble, France, (7) Centre de Recherches Pétrographiques et Géochimiques CNRS UPR 2300, 54501, Nancy, France.

**Abstract**

Zircons and monazites from 6 samples of the North Ayilari dextral shear zone (NAsz), part of the Karakorum fault zone (KFZ), have been dated with the U-Th-Pb method, using both ID-TIMS and SIMS techniques. The ages reveal (a) inheritance from several events spanning a long period between the late Archean and the Jurassic; (b) an Eocene-Oligocene magmatic event (~35-32Ma); (c) an Oligo-Miocene magmatic event (~25-22 Ma), at least partly synkinematic to the right-lateral deformation (d) a period of metamorphism metasomatism (~22-14 Ma) interpreted as thermal and fluid advection in the shear zone.

The Labhar Kangri granite located ~375 km farther Southeast along the KFZ is dated at 21.1±0.3 Ma. Such occurrence of several Oligo-Miocene granites along the KFZ, some of which show evidence for synkinematic emplacement, suggests that the fault zone played an important role in the genesis and /or collection of crustal melts.

We discuss several scenarios for the onset and propagation of the KFZ, and offset estimates based on the main sutures zones. Our preferred scenario is an Oligo-Miocene initiation of the fault close to the NA range, and propagation along most of its length prior to

~19Ma. In its southern half, the averaged long-term fault-rate of the KFZ is greater than 8 to 10 mm/yr, in good agreement with some shorter-term estimates based on the Indus river course, or Quaternary moraines and geodesy. Our results show the KFZ cannot be considered as a small transient fault but played a major role in the collision history.

Keywords: U/Pb dating, ductile strike-slip deformation, Karakorum fault zone, Tibet.

## 1. Introduction

Whether strike-slip shear zones in continental collision domains are long-term lithospheric features, steadily accommodating large amounts of strain during long time spans, or short-lived and more transient features participating in distributed regional deformation of the crust remains a topic of debate. In the case of the India-Eurasia collision, interest focus on the main strike-slip faults bounding, or cutting across, the Tibetan plateau (inset Figure 1). Some consider that such faults play a major role in absorbing the convergence [e.g. *Tapponnier et al.*, 1986, 2001], while other think that they are negligible [e.g. *England*, 1986].

In northern and eastern Tibet, far from the Indus-Tsangpo suture zone and the Himalayas, large finite motions along major strike-slip faults are well documented. The sinistral Ailao Shan – Red River Shear Zone appears to have moved for 700±200 km [*Leloup et al.*, 1995], since at least 33 Ma until ~17 Ma [*Briais et al.*, 1993; *Leloup et al.*, 2001, *Gilley et al.*, 2003]. Along the northern boundary of Tibet, the Altyn Tagh fault accrued ~375 km of sinistral offset since the Early Miocene at the longitude ~90ºE [*Ritts and Biffi*, 2000; *Yue et al.*, 2001; *Ritts et al.*, 2004]. More to the west, at ~83°E, it offsets up to ~600 km a Permian batholith [e.g., *Tapponnier et al.*, 2001; *Ritts and Biffi*, 2000; *Yue et al.*, 2001; *Ritts et al.*, 2004]. These two faults are long-lasting boundaries allowing lateral motion of large portions of the continental lithosphere.

In western Tibet, much closer to the Himalayas, it is still disputed if a major long-lasting strike-slip boundary developed and remained stable for several tens of millions of years in a context of thick and hot continental crust. To this respect, key points are the timing of initiation, the rate(s), the finite offsets, and the propagation history of the 1000-km long, active Karakorum Fault zone (KFZ). Proposed timing for the onset of the KFZ varies between less than 5Ma ago to possibly more than 32 Ma [*Searle*, 1996; *Searle et al.*, 1998; *Phillips et al.*, 2004; *Searle and Phillips* 2004, 2007; *Murphy et al.*, 2000; *Valli et al., 2007*; *Lacassin et al.*, 2004a, 2004b; *Rolland et al.,* in press].

Such age constraints are mostly derived from the study of ductile deformation along the KFZ in the Pangong area, as well as in the North Ayilari range (NA range) ~200km further to the SE (Figure 1). Here, we present new U-Th-Pb ages obtained by Isotopic Dilution and Thermo Ionisation Mass Spectrometry (ID-TIMS) and Secondary Ion Mass Spectrometry (SIMS), on zircon and monazite grains from the NA range. Combined with structural evidence our ages bring constraints on the time relationships between magmatism, metamorphism and right-lateral deformation in the NA range and allow discussion on the long-term fault rates of the Karakorum fault zone.

## 2. Geological setting of the North Ayilari (NA) range.

### *2.1. The Karakorum fault zone*

The Karakorum fault zone (KFZ) is a major right-lateral active fault, stretching for more than 1000km from the Pamir to the Indus-Tsangpo suture zone suture (Figure 1) *[e.g., Armijo et al., 1986; 1989; Ratschbacher et al., 1994; Chevalier et al., 2005; Lacassin et al., 2004a].*

Near Gar, the North Ayilari active fault (NAaf) segment of the KFZ trends more northerly and has a normal component of slip, leading to the subsidence of the Gar pull-apart, and the uplift of the ~6000 m high North Ayilari (NA) range (Figures 1 and 2) [e.g., *Armijo et* *al*., 1986; 1989; *Chevalier et al*., 2005]. Such recent uplift induced the exhumation of granitoids and gneisses corresponding to a ~5 km wide shear zone parallel to the NAaf: the North Ayilari shear zone (NAsz). This shear zone corresponds to a deep portion of the KFZ [*Matte et al.*, 1996; *Lacassin et al*., 2004a], continuously deformed, cooled and exhumed since ~21Ma [*Valli et al., 2007*] (Figure 2). Most samples of this study come from the NA range (Figure 2).

Further to the SE, the KFZ prolongates along the Indus-Tsangpo suture zone eastward of the Kailas range (Figure 1). No other gneisses are found along the fault trace but dextrally sheared schist outcrop south of the Mt Kailas [*Lacassin et al*. 2004a]. Farther East the active strand of the KFZ bounds the Labhar Kangri granite to the north (Figure 1). In order to discus the age of that granitoid and its relationship with shearing along the KFZ sample K2P30 was taken from its undeformed southern margin.

### *2.2. Ductile deformation linked with the Karakorum fault zone: the North Ayilari shear zone (NAsz).*

Ductile deformation in the NAsz is described by Lacassin et al. [2004a], and Valli et al. [2007, section 3, Figures 4, 5 and 6]. Along the NA range northeastern margin most rocks are mylonitized and show a steep high temperature (HT) foliation, striking almost parallel to the NAaf (Figure 2a). That foliation becomes flatter in the core of the range where deformation is milder (Figure 2). Close to the NAaf, the HT foliation is overprinted by a green schist foliation and by brittle-ductile deformation related to the active fault zone (Figure 2). The HT foliation bears a nearly horizontal stretching lineation, which is everywhere parallel to the NAaf even when foliation is flat (Figure 2). Deformation is unambiguously rotational, and shear senses are right-lateral where the foliation is steep (Figure 3c, d), and top to the southeast where the foliation is nearly horizontal (Figure 3b). Such geometry with flat foliation away from the core of the shear zone is observed in major strike-slip zones as the Ailao Shan Red River in SE Asia (e.g. Leloup et al., 1995), and is consistent with an overall dextral ductile shearing in a ~5 km wide shear zone parallel to the NAaf: the North Ayilari shear zone (NAsz) [*Valli et al*. 2007].

From the study of quartz and feldspar microstructures, *Valli et al*. [2007] concluded that dextral shearing in the NAsz was continuous from 700-400°C to temperatures lower than 250°C. Unfortunately, in the absence of index minerals, particularly garnet, and due to the overprinting of early structures by lower temperature ones, the peak temperature reached during shearing can not be precisely documented but is clearly above 400°C.

### ***2.3. Relationships between magmatic and mylonitic rocks. Structural setting of dated samples.***

Locally, undeformed granites and leucocratic dykes crosscut the HT foliation. For example, in the southwest part of section 1, a large granite body intrudes migmatitic gneisses (Fig. 1) that show top to the SE directed shearing parallel to the NAsz on flat-lying foliation. The migmatitic gneisses can be found as panels within the granite. Sample L89 corresponds to the leucosome of migmatitic gneisses outside of the granite (Figures 3a, b). Undeformed leucocratic veins cut across both the granite and the migmatitic gneisses (Figure 3h).

Closer to the NAaf, for example in the NE part of sections 2 and 3, such leucocratic veins are strongly sheared (Figure 3e) and inter-layered with right-lateraly sheared, biotite-rich and two-mica mylonites (Figure 3g). P20 (K1P20 of *Lacassin et al*. [2004]) corresponds to such biotite rich (~40%) orthogneiss (Figure 2). P18, located ~300m farther NE is a dextrally sheared two micas orthogneiss (Figure 2; Figure 3c). In a similar structural location, P34 (Figure 2) is a leucocratic mylonitic orthogneiss (Figure 3d) located in the NE part of section 2.

Along section 3, the density of leucocratic veins increases towards the SW. Outcrop 3-A exhibits a large amount of leucocratic dykes, either deformed and transposed parallel to the foliation within the gneisses (T) or mildly to undeformed dykes (C) that crosscuts the foliation and the deformed dykes at high angle (Figure 3f). These field relationships indicate that the dykes are synkinematic to the right-lateral deformation. Sample C32 (K1C32 of *Lacassin et al*. [2004]) is a mildly deformed crosscutting dyke (Table 1, Figures 2, 3f).

Five kilometers to the SE, Section 4 is exclusively made of sheared leucocratic orthogneisses with steep foliation in the NE that shallows to the SW (Figure 2). C43 leucocratic orthogneiss, was sampled where foliations are flatter and deformation mild (Figure 2) but shows top to the southeast shear sense.

The field relationships described above can be summarized as follows. 1) The migmatitic gneisses (L89) are sheared within the NAsz but are intruded by the granite outcropping in section 1. 2) The leucocratic dykes (C32) intrude all units, including the granite and the dextrally sheared rocks (P18, P34), but 3) Close to the NAaf they are all strongly sheared and transposed parallel to the right-lateral HT foliation and appear synkinematic to the right-lateral ductile deformation [Valli et al., 2007].

## 3. Geochronology analytical methods

Zircon and monazite grains were separated using a Wilfley table, heavy liquids and a Frantz magnetic barrier separator. The final selection of grains according to color and morphology was done using a binocular microscope. The fractions selected for ID-TIMS dating (C43 monazite, C32 zircon and monazite, and P30 zircon) were washed in hot 4 M $HNO_3$ and $H_2O$ respectively. The selected grains were dissolved using 29 M HF for zircons or 8 M HCl for monazites in PFA Teflon Ludwig-type Savillex microcapsules [*Parrish*, 1987] at 220°C, during 24h (monazite) to 60h (zircon). Chemical separation and mass spectrometry were performed according to *Paquette and Pin* [2001]. The U and Pb isotopes were measured on a VG Sector 54W mass spectrometer in multi-collector static mode. The isotopic ratios are corrected for mass discrimination (0.1 ± 0.015% per amu for Pb and U), isotopic tracer contribution and analytical blanks: 7 ± 2.5 pg for Pb and less than 1 pg for U. Initial common Pb is corrected for each fraction using the *Stacey and Kramers* [1975] two-step model. Data errors (2σ) of the zircon fractions and ages were calculated using the PBDAT 1.24 and Isoplot/Ex 3.23 programs [*Ludwig* 1993, 2005].

For in situ ion microprobe analyses, the selected grains were mounted together with standard in epoxy resin. The mounts were then abraded and polished to expose at the surface the middle part of the crystals. Each grain was imaged using cathodoluminescence (CL) and backscattered electron (BSE) scanning microscope to characterize the zoning patterns and inner structures. In-situ dating of monazite was also performed from rock thin sections, which allows preserving the potential links between the measured ages and the textural location of the grains. Using a diamond saw specific zones from the thin sections containing the radiogenic minerals were extracted. Pieces were then mounted together with zircon and/or monazite standard in epoxy resin and then polished. MOACIR monazite standard [*Seydoux-Guillaume et al*., 2002] and 91500 zircon standard [*Wiedenbeck et al*., 1995] were used for samples P20, and TEMORA 1 for all the others [*Black et al*., 2003]. Zircons in samples P18, P34, C43, L89 and monazites in sample L89 were analysed for U, Th and Pb isotopes using the sensitive high resolution ion microprobes (SHRIMP II) at the Institute of Geology of Beijing, China, while zircons in sample P20 and monazites in sample P18 were measured using the Cameca IMS 1270 at CRPG in Nancy, France. Calibration parameters, data acquisition and age correction are described in *Compston et al*. [1984] for the SHRIMP II, and in *Deloule et al*. [2001] for the Cameca IMS 1270. The error on the calibration curve is taken into account for the age uncertainty calculation. The spot size was between 30 and 60 μm, and their contours were precisely drawn after each analytical session using secondary and backscattered electron (BSE) images.

Ion probe U-Th-Pb dating of young minerals is an analytical challenge because of the very small amounts of radiogenic daughter isotopes ($^{206}$Pb, $^{207}$Pb, $^{208}$Pb). In case of recent minerals, it is now usual for most geochronologists to consider the $^{238}$U/$^{206}$Pb ages as the most reliable for zircons (e.g., [*Stern and Amelin*, 2003]), and the $^{232}$Th/$^{208}$Pb ages for monazites (e.g., [*Catlos et al.,* 2004]). The isotopic systems of zircons and, to a lesser extent, monazites keep the memory of several distinct magmatic, metamorphic and hydrothermal events. This provides the opportunity to reconstruct complex geological histories but requires cautious interpretation of the analytical results to individualize the different populations.

Within a given population of ion probe data, it is important to distinguish meaningful ages from outliers, which can always occur in spite of careful selection of rocks and minerals, and of rigorous analytical conditions. Age disparity around a mean value may results either from (1) an overlap of the probe beam on zones of distinct ages, (2) large SIMS analytical errors related to low radiogenic Pb content in young zircon overgrowths [*Stern*, 1997], (3) the occurrence of common Pb, (4) $^{230}$Th radioactive disequilibrium in monazites [*Schärer*, 1984], (5) a partial lead loss due to (a) subsequent high temperature event(s), (6) a combination of these points. For example, zircon z227 of sample C43 gives significantly distinct ages at its two tips that should *a priori* give similar ages because they belong to the same growing band (z227-2 & -3, Table 4, Figure 4b). One of these two ages is among the youngest of its population while the other is the oldest. It is very difficult to determine which result is the most significant. Consequently, we consider that the best age estimate of a given population of ion probe data is its mathematical mean with a two standard deviation uncertainty, which will lower the influence of outlier(s).

## 4. U-Th-Pb data and interpretations:

The Tertiary SIMS data are plotted on the Tera-Wasserburg diagram [*Tera and Wasserburg*, 1972] (1σ error crosses for readability) while others data are plotted in concordia diagrams (2σ ellipse errors or larger symbols when ellipses are too small). Errors mentioned in the text are at the 2σ level, the weighted averages, and the associate 95% confidence errors, were calculated with Isoplot 3.23 of *Ludwig* [2005].

### *4.1. Top to the south sheared rocks in the core of the NA range*

#### *4.1.1 migmatitic leucosome L89*

4.1.1.1 Zircons

Sixteen zircons were imaged and in situ dated using SHRIMP II (Table 2). The zircon grains are euhedral to subhedral and exhibit distinct rim-core domains and oscillatory zoning (e.g. Figure 4).

Zircon z28 is euhedral and exhibits an oscillatory zoning pattern (Figure 4a). The crystal core is characterized by a magmatic Th/U ratio and yields a 34.7 ± 2.4 Ma $^{206}Pb/^{238}U$ age (Table 2). A small euhedral zircon grain (z34) also displaying a magmatic Th/U ratio is dated at 23.4 ± 4.0 Ma. Twelve grains are concordant and have inherited $^{206}Pb/^{238}U$ ages between 200 and 500 Ma, possibly representing several Triassic to Cambrian magmatic events or a rough discordia trajectory between 23-35 Ma intercepts and ~500-600 Ma (Figure 5). Two other analyzed grains (z29, z33) are significantly discordant indicating Proterozoic to Archean $^{207}Pb/^{206}Pb$ ages of 1.7 and 2.6 Ga. Owing to the very small size of the zircon grains, the probe beam often crosscut cores and overgrowth domains, implying that some ages may correspond to mixed values.

4.1.1.2. Monazites

Eleven subhedral to anhedral monazites coming from sample L89 were dated in thin section with the SHRIMP II. One grain (M1) shows Mesozoic inheritance (Table 3). The ten remaining monazite grains yield $^{208}$Pb/$^{232}$Th ages ranging from 25.4 ± 3.6 Ma to 13.1 ± 5.1 Ma (Figure 6). Note that the oldest monazites, found in inclusions within biotites and chlorites (M3-1, 2 and M25), have an average age broadly synchronous with magmatic zircon z34 suggesting the crystallization of the rock at ~24.2 ± 2.4 Ma (Figure 6). Younger ages can be related to several crystallization events between ~22-13 Ma, or to partial opening of the Th-Pb system at ≤13 Ma.

*4.1.2. C43* leucocratic orthogneiss.

Eleven zircon grains were selected for ID-TIMS and SHRIMP II dating. Zircon rims are dark in CL images indicating a higher U-content relative to their rounded or prismatic cores (Figure 4b). Ten zircon rims yield concordant ages ranging from 25.2 ± 1.7 Ma to 13.0 ± 0.8 Ma with a median value for the $^{206}$Pb/$^{238}$U ages of 17.8 +4.4/-3.4 Ma (Table 4, Figure 7a). The Th/U ratios are systematically low (0.01-0.05), pointing out for strong Th depletion relatively to U, which is often related to the (re)-crystallization of the rims during metamorphism or metasomatism [*Rubatto et al.*, 2001]. These rims are strongly U-enriched (6800 – 20,000 ppm), compared to the cores. This implies that the crystallization of the rims happened in equilibrium with a fluid enriched in trace elements and especially in U (e.g., [*Rubatto and Gebauer*, 1998]). This very high U concentration could have favoured Pb-loss, producing the discordance of the analytical points along a chord close to the Concordia. However this possibility is ruled out by the lack of any correlation between discordance level and U content, the rim growth is therefore most probably related to several hydrothermal pulses between ~25 and ~13 Ma. In addition, two monazite fractions analyzed by ID-TIMS are concordant at 14.4 ± 0.7 Ma (Table 5), implying the (re)crystallization of monazites at that time.

Among eleven spots on zircon cores, a single one (z244-1) yields a subconcordant age of ~22 Ma (Figure 7a) coinciding with zircon rims and displays intermediate Th/U ratio (0.09) and U-content (1379 ppm). All the other cores yield older ages ranging from $^{206}Pb/^{238}U$ ~170 Ma to $^{207}Pb/^{206}Pb$ ~3.0 Ga (Figure 7b). Most of these cores show high Th/U ratios (0.18-2.2) suggesting a magmatic origin (Table 5), but the analytical points are mostly discordant and it is impossible to distinguish a simple age pattern or to draw a significant discordia array (Figure 7b).

### *4.2. Right-laterally sheared gneisses in the core of the North Ayilari shear zone.*

#### *4.2.1. P34 leucocratic mylonitic orthogneiss*

Nine euhedral to subhedral grains (e.g. Figure 4c) were selected for in situ SHRIMP II dating. Most of the cores and rims exhibit oscillatory zoning, which are often disrupted in the complex and re-crystallized cores.

Five zircon rims characterized by low metamorphic Th/U ratio (0.01-0.08) yield concordant and nearly concordant tertiary $^{206}Pb/^{238}U$ ages ranging from 26.9 ± 1.6 to 18.2 ± 1.2 Ma with a mean of 22.1 ± 4.7 Ma (Table 6, Figure 8a). U contents are higher in the rims (1400-2500 ppm) than in the cores (170-1300 ppm). This suggests rim formation by (re)crystallization in equilibrium with a metamorphic fluid enriched in trace elements [*Hoskin and Schaltegger*, 2003; *Rubatto and Gebauer*, 1998]. One core (z120-1, not plotted in Figure 8 since no reliable $^{207}Pb/^{235}U$ age was obtained), characterized by low metamorphic Th/U ratio (0.01), and low U-content (230 ppm), and by the absence of oscillatory zoning, yielded a 20.9 ± 2.2 Ma $^{206}Pb/^{238}U$ age. Three cores (z147-1, z156-1, z153-1) and one rim (z145-1, 3) yielded concordant ages around 300 Ma (Figure 8b, Table 6). The five other analyzed cores are significantly discordant and indicate Proterozoic $^{207}Pb/^{206}Pb$ ages between 0.9 Ga and 1.8 Ga.

*4.2.2. P18 two-mica orthogneiss*

4.2.2.1 Zircons

Twenty-four ages where obtained from ten zircon crystals using the SHRIMP II (table 7). All zircons are euhedral, colourless, non-fractured, and contain rounded to prismatic cores. On CL images, eight of these crystals show rims much darker than cores (e.g., Figure 4D) indicative of higher U-content at their borders [*Hanchar and Rudnick*, 1995; *Rubatto and Gebauer*, 1998]. Some cores or rims exhibit clear oscillatory zoning. Only two zircons crystals (z8 & z41) present uniform oscillatory zoning patterns over the whole grain without any rim-core transition (Figure 4d). The $^{206}Pb/^{238}U$ ages measured in the central parts of these two grains are similar and yield a mean value of 34.4 ± 1.3 Ma (Table 7, Figure 9a). Their Th/U ratios (0.21 to 1.40) rather favour a magmatic origin for the zircons [*Rubatto and Gebauer*, 1998]) as well as their continuous oscillatory-zoning patterns [*Gebauer*, 1996; *Rubatto and Gebauer*, 1998; *Schärer et al.*, 1995; *Vavra et al.*, 1996]. This suggests that magmatic zircons crystallized around 34 Ma are present in sample P18.

Twelve analyses of the rims were performed, all ages being concordant or sub-concordant within 2σ error limits, with $^{206}Pb/^{238}U$ ages spanning between 27.4 ± 1.9 and 19.8 ± 1.4 Ma (Table 7, Figure 9a) with a $^{206}Pb/^{238}U$ median age of 23.3 +4.0/-2.2 Ma.

Six zircon cores yield concordant $^{206}Pb/^{238}U$ ages spreading between 181 ± 13 and 438 ± 27 Ma (Table 7). Such ages could correspond either to several Lower Jurassic to Cambro-Ordovician magmatic events, or to a discordia line between ~34 - 23 Ma and ~500 Ma intercepts (Figure 9b). Two cores give older $^{207}Pb/^{206}Pb$ apparent ages at ~1.0 and ~1.8 Ga, suggesting inheritance from Proterozoic magmas.

4.2.2.2. Monazites

Sixteen subhedral to anhedral monazites were dated *in situ* within thin sections (Table 8) using the SHRIMP II. On BSE images the grains display concentric to patchy zoning patterns (Figure 10). $^{208}$Pb/$^{232}$Th apparent ages span between 27.9 ± 3.6 Ma and 13.5 ± 1.7 Ma with a relationship between the ages and the textural position of the grains (Figure 11, Table 8). The four oldest monazites are included in biotite or feldspar crystals, with a mean $^{208}$Pb/$^{232}$Th age of 25.2 ± 1.6 Ma, whereas the twelve remaining interstitial monazite grains display ages ranging from 23.7 ± 3.0 Ma to 13.5 ± 1.7 Ma with a mean of 18.8 ± 2.8 Ma.

Included monazites are broadly synchronous with zircon magmatic rims which favour the hypothesis of the crystallization of the rock at ~25-23 Ma. Th-Pb ages of interstitial monazites are younger, down to 13.5 ± 1.7 Ma (Figure 11). This could be related to the occurrence of one or several thermal pulses between ~23 and 13 Ma, as interstitial monazites are potentially more sensitive to hydrothermal fluids than the included grains. The Th/Pb dating providing only apparent ages, this 25-13 Ma spread in age could also be related to the discordancy of the analysed spots towards a lower intercept at ≤13 Ma.

*4.2.3. P20 biotite-rich gneiss*

Four zircon grains were dated in thin sections with the Cameca IMS 1270. $^{206}$Pb/$^{238}$U ages range between 23.9 ± 6.9 Ma and 19.9 ± 1.6 Ma with an average value of 21.7 ± 3.6 Ma (Table 9 and Figure 12). The high Th/U ratios suggest crystallization or re-crystallization of magmatic zircon grains at ~22Ma.

***4.3. C32 Leucocratic dyke***

Five zircon fractions were selected for ID-TIMS dating. The most acicular zircon grains (z1) yield a concordant age of 22.7 ± 0.1 Ma, while the four other fractions are discordant, and define a chord yielding a lower intercept at 32.5 ± 2.6 Ma and an upper intercept at 1296 ± 120 Ma (Figure 13, Table 5).

The concordant fraction at ~23 Ma most likely represents the crystallization of zircons during a high temperature event. The lower intercept at ~33 Ma may represent either a high temperature event, or may be related to a fortuitous alignment of inherited zircon grains affected by multi-episodic Pb loss. The good alignment and the position of the analytical points close to the lower intercept rather favour the first hypothesis. The syn-kinematic leucogranite C32 crystallized at ~23 Ma and probably represents the result of partial melting of a ~33 Ma old magmatic intrusion. The upper intercept at ~1300 Ma is poorly defined by discordant fractions and may reflect either a single crystallization event or the average of a complicate inheritance pattern.

Two monazite fractions were dated by ID-TIMS (m1 & m2, Table 5). The concordant, slightly overlapping analytical ellipse errors yield a mean age of 15.8 ± 0.2 Ma (2$\sigma$) (Figure 13). This implies the primary crystallization of newly formed hydrothermal or metamorphic monazite crystals or the resetting of older magmatic grains within the leucogranite C32 at that time.

4.4. Labhar Kangri granite K2P30

In sample P30, the zircons are colourless and translucent needle-shaped crystals, as well as elongated light pink and yellow short-prismatic euhedral grains. Six fractions were selected for ID-TIMS dating (Figure 14). One fraction of acicular grains yield a concordant age of 21.1 ± 0.3 Ma (Table 10), comparable to those measured on westernmost granitoids from the

Ayilari range. The five remaining fractions are discordant and indicate two different inherited component with upper intercept ages at 494 ± 45 Ma and 1447 ± 38 Ma.

## 5. Summary and discussion

### *5.1. Summary of U-Th-Pb data in the NA range.*

All U-Th/Pb ages obtained in the Ayilari range are summarized in Table 11 and Figure15. All samples unless P20 reveal at least three magmatic or metamorphic / metasomatic episodes. All samples record Cenozoic ages comprised between 35 and 14 Ma. The age inheritance patterns derive from several events spanning a long period between the late Archean (~3Ga) and the Jurassic ( ~ 170 Ma). Three samples (C32, P18 and L89) indicate an Eocene-Oligocene (~35-32 Ma) magmatic episode. These three samples also show a younger Oligo-Miocene magmatic event for which populations of monazite and zircon grains yield average ages between ~25 and 23 Ma. This magmatic event is also indicated by P20 zircons (21.7±3.6 Ma). A ~25-22 Ma magmatic event is thus recorded in most samples of the NAsz.

In samples P34 and C43, metamorphic zircons, characterized by low or intermediate U/Th ratio and U-contents, crystallized around 21 Ma. Hydrothermal zircons characterized by high to very high U-content, and very low U/Th ratio crystallized between ~22 and 17 Ma while monazite populations in samples L89, P34, C32, P18 and C43 yield ages between ~19 and ~14 Ma. We interpret these ages as the result of metamorphism and metasomatism either during several pulses during the ~22-14 Ma time period, or as a single ~14 Ma event producing partial Pb loss and discordance of the analytical points.

The cooling history of the NA range is constrained by Ar/Ar, U-Th/He and fission track data (Figure 16) [*Valli et al., 2007*; *Lacassin et al.*, 2004a]. These data reveal rapid cooling below ~350°C starting at ~15 Ma along section 1 and at ~13 Ma in all other sections. Such cooling history fits well with the fact that no zircon, nor monazite populations, gives U-Th/Pb age younger than ~14 Ma.

The picture that emerges is that major Oligo-Miocene (23.4 ± 1.4 Ma) magmatic, event(s) affected rocks containing Eocene-Oligocene and pre-Mesozoic inherited zircons. These rocks were then affected by metamorphism and metasomatism, and after ~15 Ma rapidly cooled below 350°C (Figure 16).

### *5.2. Age of deformation in the Ayilari Range.*

Because C32 leucocratic dyke is synkinematic to the right-lateral deformation (see 2.3. and Figures 3e, f, g), *Lacassin et al*. [2004] inferred that deformation started prior to the emplacement of that dyke. At a larger scale, the fact that numerous undeformed leucocratic dykes cut across the deformed migmatites (Figure 3a) corroborate that such dykes postdate the onset of deformation in the NAsz. An age of 22.7 ± 0.1 Ma is given to C32 by the youngest concordant zircon fraction it contains (Figure 13, Table 5). This age is a lower bound for the onset of right-lateral shear.

The three other samples that record Oligo-Miocene magmatism (L89, P18, and P20) have been affected by ductile deformation related to the NAsz. Their U/Pb ages spanning from 25 to 21 Ma could thus be interpreted as an upper bound for the onset of shearing (i.e. the age of the protolith prior to deformation). However, the fact that these ages are identical within errors to that of C32 (Figure 15), and that S-C fabrics, typical of shear under high to medium-grade temperature conditions and often of syn-kinematic granitoid (e.g., [*Gapais*, 1989a; 1989b; *Gapais and Barbarin*, 1986]), are ubiquitous in the NAsz (Figure 3), suggest that migmatisation (L89) and Oligo-Miocene magmatism (P18 and P20) are at least partly synkinematic. This implies that the magmatic ages of these rocks do not provide a strict upper bound, but that deformation started some time during or prior to the Oligo-Miocene magmatic episode at 22-25 Ma. On the other hand, there is no clear argument to link the older Eocene-

Oligocene phase of magmatism seen in samples L89, C32 and P18 (35-32 Ma) to right-lateral deformation deformation along the KFZ.

These conclusions are in agreement with the cooling histories based on Ar/Ar data that suggest that the shear zone temperature dropped below 400°C before 15 to 21 Ma depending on the samples considered (Figure 16) [*Valli et al., 2007*], thus implying that ductile deformation was chiefly acquired prior to 21 Ma at least for some part of the shear zone. This interpretation is however strongly contested by authors that consider that there is no evidence for synkinematic partial melting, and thus that right-lateral shear should have started after, not before, ~21 Ma [*Searle and Phillips*, 2004, 2007]. The crucial point in that controversy is that the crosscutting dykes are clearly syn to late kinematics (C32 see Figure 3) and dated at 22.7 ± 0.1 Ma (Figure 13), implying that deformation started before that time. Postponing the onset of ductile deformation in NAsz would imply a) to contest the age of C32, b) to infer that temperatures stayed above 400°C more recently than suggested by the Ar data and c) to provide an alternative explanation for the ages of metamorphic and metasomatic zircons and monazites that fill the gap between the last magmatic event and the onset of rapid cooling linked with right-lateral / normal deformation.

The most straightforward interpretation of our data is thus to confirm the analysis of *Lacassin et al*. [2004] that links the Oligo-Miocene magmatism, and the following metamorphism and fluid circulation in the NA range to right-lateral shear in the Karakorum shear zone. Metamorphism and fluid advection is typical of major strike-slip shear zones as documented in several natural examples [e.g. *Leloup et al.*, 1999, and references therein; *Moore et al.*, 2001]. This in turns implies that right-lateral deformation initiated at high temperature in the NAsz prior to ~22 Ma, probably during or just prior to the 25-22 Ma magmatic episode. The deformation pursued under decreasing temperature conditions until

~300°C were reached ~15 to 10 Ma ago [Valli et al., 2007]. Since then right-lateral / normal brittle deformation occurs along the NAaf.

### *5.3. Insights into pre-Tertiary history of the Ayilari rocks*

The Ayilari range is located in the southeastern prolongation of the Ladakh batholith (Figure 1) that emplaced between ~103 and 50 Ma [e.g., *Schärer et al*., 1983; *Weinberg and Dunlap,* 2000; *Schwab et al*., 2004]. Surprisingly, despite the large number of analyzed zircons in our study (~50) we did not find any inherited core recording such crystallization ages (Table 11). As already discussed, the age inheritance patterns of most samples are multi-genetic with zircon grains being derived from several events spanning a long period between the Jurassic and the late Archean (between ~170 and 3000 Ma) (Table 11, Figures 5, 7b, 8b, 9b, 13, 14). This large age span together with the high mica content of the samples (between 13 and 40%) suggests that most of the Ayilari Range Tertiary granitoids initially derive from melting of metasedimentary rocks [*Chappell and White*, 1974], possibly through several melting episodes. This indirectly confirms that the eastern part of the Ladakh batholith emplaced on a continental basement as proposed by Rolland et al. [2000] and Rolland [2002]. The youngest concordant zircon grain ages, older than the Ladakh batholith emplacement, are around 400 Ma. This age yield an upper bound for the deposition of the sediments constituting the protolith. Considering the Tertiary events as lower intercepts, discordant inherited zircons younger than ~400 Ma broadly define a discordia line with this Early Devonian upper intercept (Figures 8b and 9b). This suggests a post Early Devonian deposition of the original sediments. In the absence of any Himalayan age, deposition probably took place prior to the emplacement of the Ladakh batholith. Such sediments possibly correspond to the Paleozoic-Mesozoic Tethyan series, which are actually outcropping on the Qiangtang and Lhasa blocks [*Jiao et al*., 1988].

***5.4. Timing of onset of the KFZ: conflicting constraints from various places along the fault ?***

Because the KFZ stands out as the main active strike-slip fault bounding the Tibetan plateau to the southwest its timing and slip history have been the subject of several studies. Various constraints on the timing of the fault onset have been proposed in different places. These constraints are summarized in table 12 and Figure 17.

Across the Baer basin, Murphy et al. [2000], propose that the South Kailas thrust has been offset 66±5.5 km by the KFZ. The age of this thrust, deduced from the cooling history based on a single Kf Ar data from its footwall [Yin et al., 1999], is ~13Ma. This would constrain the KFZ to be younger than 13 Ma at this location ([9] on Figure 17 and Table 12).

Along the Pangong and Nubra ranges (Figure 1), the KFZ was first thought to be younger than ~5 Ma [*Searle*, 1996]. Since then, the description of ductile deformation in these ranges, in a restraining bend between two strands of the KFZ, and the dating of granitoids led to propose older ages for the onset of deformation [e.g. Searle, 1998]. By linking rapid cooling, starting at ~17Ma according to cooling histories based on Ar data, with transpression along the fault *Dunlap et al*. [1998] proposed that motion on the KFZ started at that time ([3] on Figure 17 and Table 12). Considering that all granitoids, unless few late dykes, are strictly pre-kinematics, led to bracket the onset of right-lateral shear between 15.7 and 13.7 Ma ([1] and [2] on Figure 17 and Table 12), [*Phillips et al.*, 2004, *Searle and Phillips* 2004, 2007; *Phillips and Searle*, 2007].

On the basis of the age constraints at Pangong and Baer, the KFZ might have started in Pangong at ~14 or 17 Ma and propagated to the SE reaching Baer less than 13 Myr ago ([A] on Figure 17, Murphy et al., [2000]). However, this would imply a shear onset after ~13 Ma in the NA range, which is in contradiction with our results ([6] and [7] in Figure 17 and Table 12), (see section 5.2; *Lacassin et al.*, 2004; Valli et al., 2007). It could thus be envisaged that the KFZ nucleated in the North Ayilari 25-22 Ma ago or before, prior to propagate northwestward, reaching Pangong after ~15.7 Ma, and southwestward reaching Baer after 13 Ma, thus reconciling previous interpretations ([B] on Figure 17). This would imply propagation rates on the order of 20 to 30 mm/yr (northwestward), and ≤1 mm/yr (southwestward). Such rates would be very low compared for example with the propagation rates of 138 to 200 mm/yr inferred for the North Anatolian fault [*Armijo et al.*, 1999]. Furthermore, they would not allow the KFZ to reach its total length before present time. More complicated scenarios, such as variations in fault propagation rate or simultaneous initiation in distant parts of the fault cannot be ruled out, but remain conjectures given the dearth of data.

To the contrary, there is evidence that the KFZ was active in Tangtse and Baer prior to ~15 and ~13 Ma respectively [Lacassin et al., 2004a], implying an older history of the KFZ. According to *Murphy et al.* [2000, 2002] the KFZ ends southward in the Gurla Mandhata detachement system (GMDS) (Figure 1), implying that the KFZ started to slip less than 13 Ma ago in the Mt Kailas area. *Lacassin et al.* [2004a] showed that this hypothesis is implausible because (a) there is no demonstrable connection between the KFZ and the GMDS, the ophiolitic rocks in between being not significantly offset (Figure 1); (b) structural mapping in the Kailas range rather indicates that most of the dextral motion is transferred east of the GMDS along the Yarlung Tsangpo suture zone; (c) the South Kailas thrust cannot be used as a marker to define a piercing point because it is a part of the KFZ flower structure mapped in this area. The 13 Ma age derived for this thrust [*Yin et al.*, 1999] is thus only an evidence for KFZ activity at that time. It is thus probable that the KFZ initiated in Baer prior to 13 Ma ago.

Other lines of evidence also concur to suggest that the Tangtse shear zone in the Pangong area was active prior to ~16 Ma. (1) Several generations of variously deformed dykes with late ones less deformed and cross-cutting earlier transposed ones suggest synkinematic intrusion. (2) The field relationships and microstructures depicted by Searle and Phillips [2007, Figure 3] and Phillips and Searle [2007] have been interpreted to show that ductile deformation started after 15.6 and stopped at ~13.7 Ma. However, Ar/Ar thermochronology indicates conditions compatible with ductile deformation (≥300°C) until 10-7 Ma [e.g., *Dunlap et al.,* 1988]. This would imply that right-lateral shear took place during 2 Myr. (15.6-13.7 Ma), then stopped during 4 to 7 Myr, before to resume with brittle deformation along the Karakorum fault. Such strange behaviour would need to be justified (3) As in the Ayilari range, pervasive C/S fabrics affect the Tangtse granite [*Searle et al*., 1998; *Rolland*, 2000]. Such structures are the telltale sign that the granite cooled below solidus during shear [e.g., [*Gapais*, 1989a; 1989b; *Gapais and Barbarin*, 1986]. The fact that strike-slip deformation occurred at and below temperatures close to the granitic solidus (750°C) was indeed mentioned by *Dunlap et al*. [1998, p904] and *Weinberg and Searle* [1998, p885 and 890]. (4) The Tangtse granite is intrusive within granulitic (800°C, 5.5 Kb) and amphibolitic (700-750°C, 4-5 Kb) rocks that have been penetratively deformed in a dextral transpressive regime until greenschist conditions were reached [Rolland et al., in press]. Like the Oligo-Miocene magmatism in the NA range, the intrusion age of the Tangtse granite thus possibly only provides a lower bound to the onset of deformation [Rolland et al., in press].

If, as seems to be the case, the KFZ affected the Tangtse and Baer area prior to ~18 and ~13Ma respectively, a completely different history of the fault zone, with an early Miocene onset along most of its length, should be proposed ([C] on Figure 17). Because the remaining age constraints only provide a minimum age for initiation of faulting it is not possible to fully reconstruct such history. However hints are given by the age of Miocene plutonic rocks that appear to emanate from the KFZ (Figure 17, Table 12, see section 5.5).

A few ages in the NA range and in Tangtse have been interpreted to provide even older constrains for the onset of right-lateral shear: prior to ~35 and ~32 Ma respectively ([5] and [8],Table 12, [D] on Figure 17) [*Lacassin et al*., 2004a; *Rolland et al.,* in press]. However, in the Ayilari range, there is no structural argument to link the Eocene-Oligocene magmatic event with right-lateral shear (see section 5.2). In Tangtse, the age only rests on the last three heating steps of an amphibole that do not define a plateau, and correspond to ~25% of the total gas release. We thus consider this hypothesis ([D] on Figure 17b) as unsubstantiated.

5.5. *Miocene Magmatism along the KFZ*

The Baltoro plutonic unit (Fig. 1) crystallized in two pulses dated at 25.5 ± 0.3 Ma [*Schärer et al*., 1990] ([M2] on Figure 17, Table 12), and 21 ± 0.5 Ma [*Parrish and Tirrul*, 1989; *Schärer et al*., 1990] ([M3] on Figure 17, Table 12), at relatively low temperature (750-600°C) [*Searle et al*., 1992]. The batholith has a sigmoidal shape, with its southern and northern edges striking ~N110°, 100 km west of the KFZ and progressively bending southeastward to become parallel to the KFZ (N142° strike, Figure 17a). South directed thrusting occurred during granite emplacement along the southern edge of the batholith [*Searle et al*., 1992]. The eastern border of the batholith is bounded by the KFZ active strand and shows dextral S-C structures [*Searle et al*., 1998]. Like the Tangtse granite, the Baltoro batholith has been interpreted by *Searle* [1996] and *Searle et al*., [1998] to strictly predate the onset of dextral motion along the KFZ. However, its large-scale sigmoid shape suggests intrusion at least in part synchronous with right-lateral shear along the KFZ, coevally with thrusting along the batholith southern edge and dextral high to medium temperature deformation along its eastern border. In that case, the 25.5 or 21 Ma ages of the granitoid would, as already suggested by *Mahéo et al*. [2004], represent a lower bound for the KFZ timing initiation.

Other evidence for ~20 Ma magmatism exists along the KFZ trace, while little magmatism of this age is observed far from the fault (Figure 17a, [*Mahéo et al.*, 2002; *Schwab et al.*, 2004, and references therein]). ~200 km north of the Baltoro pluton, west of Tash Gurgan, an undeformed alkali granite striking parallel to the KFZ (Figure 17a) crystallized at ~20-18 Ma [*Arnaud*, 1992; *Xie et al.*, 1992], with very rapid cooling from 18 to 11 Ma, according to Ar/Ar data [*Arnaud*, 1992; *Ronghua et al.*, 1996; *Yingwen et al.*, 1992]. ~375 km south-east of the Ayilari range, the Labhar Kangri granite, just south of the Zangbo suture branch of the KFZ (Figures 1, 17a), yields a crystallization age of 21.1 ± 0.3 Ma (section 4.4). The alignment of all these Oligocene-Miocene plutonic units, several of them exhibiting evidence for syn-kinematic emplacement, suggests that the KFZ acted at that time as a heat source through shear heating and/or as a conduit promoting heat advection for magma ascent. This would imply that the KFZ has been a major discontinuity reaching at least into the lower crust. The occurrence of mantle-derived magmatic rocks (lamprophyres) along the KFZ north of the Baltoro granite [*Pognante,* 1991; *Searle et al.*, 1992], and in the Tash Gurgan alkaline complex [*Xie et al.*, 1992], further suggests that the KFZ roots at or below the crust – mantle transition. Furthermore, in the Pangong Range, the occurrence of deformed granulites was interpreted as evidence for heat advection along a lithospheric-scale shear zone [*Rolland*, 2000; *Rolland and Pêcher*, 2001; Rolland et al., 2001].

The KFZ shares many characteristics with the ASRR shear zone in Yunnan (SE Asia) which has been interpreted as the Oligo-Miocene continental transform boundary between South China and Indochina [e.g., *Tapponnier et al.*, 1990; *Leloup et al.*, 1995; *Leloup et al.*, 2001). The kinematic link between motion along the ASRR and sea-floor spreading in the South China Sea [e.g. *Briais et al.*, 1993, *Harrison et al.*, 1996; 2001] requires that the shear zone affects the whole lithosphere. In both cases, >1000 km long continental faults absorb large offsets (see section 5.6) during a time period of a couple of tens of Myr long. In both cases, the corresponding shear zone, where exhumed, is rather narrow (less than 20 km) and shows nearly pure strike-slip deformation coeval with magmatism partly derived from lower crust and mantle partial melting [e.g. Zhang and Schärer, 1999]. This leads us to interpret the KFZ as a lithospheric-scale fault shear zone comparable with the Red River, Altyn-Tagh, and North Anatolian fault zones.

### *5.6. Finite offsets across the KFZ, implication for long-term slip-rate*

The fact that the KFZ is a major boundary that plays an important role in Tibet tectonics is challenged by authors that consider that its long-term slip-rate is low: between 3 and 10 mm/yr [e.g. Phillips and Searle, 2007]. After a discussion on the most reliable finite offsets, our new timing data will allow us to estimate the KFZ long-term slip rate.

The course of the Indus River is offset ~120 km across the fault north of Shiquanhe (Figure 1) (*Gaudemer et al*., 1989). This value only corresponds to a minimum offset on the fault since the incision of the present river course at its present location. Southwest of the active trace of the fault entrenchment probably occurred during or since rapid exhumation in the North Ayilari range ~16 to 12 Ma ago, thus implying a long-term fault rate ≥ 8.5±1.5 mm/yr. [*Valli et al., 2007*].

*Searle et al*. [1998], *Searle and Phillips* [2004] and Phillips and Searle [2007] correlate the Baltoro with the Tangtse granite, which they take to constrain a maximum offset of 120 – 150 km across the fault near Tangtse. However, because the Tangtse granite is located between two strands of the KFZ, this correlation would only provides the offset on the Southern branch of the fault, hence, a lower bound on the total offset. Furthermore, as the Tangtse granite is synkinematic (see section 5.4), it cannot be used to define a finite offset at all.

A more detailed discussion of offsets across the KFZ is limited by the lack of accurate mapping and poor knowledge of geological structures and of their age. The most reliable markers that can be used to define piercing points along the KFZ at this stage thus appear to be major suture zones. The Indus – Tsangpo suture can be followed continuously from the eastern syntaxis to the Kailas area (Figures 1, 17). West of the Kailas, the suture zone is smeared into a ~50 km wide zone bounded to the south by the KFZ southern branch [*Lacassin et al*., 2004a; Tapponnier et al., 1986; Peltzer and Tapponnier, 1988]. This branch possibly connects with the Thanglasgo shear zone within the Ladakh batholith (TSZ, Figure 1) [*Weinberg and Dunlap*, 2000], as suggested by right-lateral shear evidences along the Indus suture zone south of Leh [Stutz and Steck, 1986; de Sigoyer et al., 2004]. Note that according to cooling histories deduced from Ar/Ar data, right-lateral ductile deformation took place in the TSZ prior to 22 Ma [*Weinberg and Dunlap*, 2000; de Sigoyer et al., 2004], in good accordance with an Oligo-Miocene age for the KFZ. Offset of the Indus suture measured on the south branch of the KFZ reaches ~200 km [*Ratsbacher et al*., 1994], or ≥220 km [This study] (Figures 17a, 18, Table 13). A large scale offset ≤400 kmis obtained taking into account the whole Karakorum deformation zone [*Lacassin et al*., 2004a].

Much farther north, the Late Palaeozoic - Early Mesozoic South KunLun suture zone is strongly deflected along the Pamir syntaxis east flank but remains essentially continuous from the western KunLun to the Pamir ranges (Figures 17a, 18) [e.g., *Schwab et al*., 2004]. Between the Indus and the KunLun three other sutures are found on both sides of the KFZ (Figures 17a, 18). However, their precise location and age has been disputed, leading to conflicting offset estimates across the KFZ (Figure 18, Table 13).

In the Pamir, the Tanymas suture is probably an equivalent of the Jinsha suture of Tibet [*Schwab et al*., 2004]. The Jinsha suture and associated rock assemblages in eastern Tibet can be followed westwards within central Tibet only to the LongMuCo area [e.g. Matte et al., 1996; Figure 17] In the absence of detailed mapping, some authors speculate that it extends westwards across the Tianshuihai terrane to reach the KFZ North of the K2 [e.g. Schwab et al., 2004; Yin and Harrison 2000] (Jinsha (a) on Figure 18), which would correspond to a ~100 to 130 km offset on the KFZ. The bulk of the large-scale geological evidence [e.g., Geology publishing house, 1998] suggests instead that this suture has been left-laterally offset and dragged along the Gozha fault implying a much larger apparent offset of 435 to 565 km across the KFZ (Jinsha (b) on Figure 18 and Table 13); [Valli, 2005].

Farther south in the Pamir, the Late Jurassic – Early Cretaceous Rushan – Pshart suture [Pashkov and Shvol'man, 1979; Shvol'man, 1980; Montenat et al., 1986; Burtman and Molnar, 1993; Leven, 1995], is coeval with the Early Cretaceous (100-140 Ma) Bangong suture [Kapp et al., 2005]. The corresponding offset across the KFZ of this characteristic, rather well mapped and well dated feature is ≥400 km [Lacassin et al., 2004a] or ~480 km [This study] (Table 13, Figure 17b, 18). Matching this Late Jurassic suture to the Triassic Jinsha suture on the Tibetan side of the fault [Searle and Philips, 2007] would lead to only ~100 km of offset (Table 13, Figure 18).

The Late Cretaceous (88-80 Ma) Shyok suture of Pakistan [Peterson and windley, 1985 Weinberg et al., 2000] appears to be a remnant of a back-arc basin that formed between 108 and 92 Ma [Rolland et al., 2000]. The most obvious match of the Shyok suture across the Karakorum fault is the Shiquanhe suture. This yield a minimum offset of ~200 km (Figures 17, 18, Table 13) . In this, we follow Matte et al. [1996] who interpret the Shiquanhe mafic and ultramafic rocks as a Late Cretaceous-Paleocene suture continuing eastwards across South Tibet to Xainza. Alternatively, Kapp et al., [2005] interpreted these rocks as far south travelled klippes from the Bangong suture zone, as did Girardeau et al. [Giradeau et al., 1985] for the Xainza – NamCo ultramafics rocks northwest of Lhasa. In that case the Shyok suture would have no counterpart in southern Tibet. Finally despite their different ages, Searle and Phillips [2007] match the Shyok and Bangong sutures across the KFZ, which brings the offset down to ~150 km (table 1, Figure 18).

Figure 18 summarizes these diverging views on suture offsets across the KFZ. One view favour small offsets (italic numbers in Table 13) [Searle and Phillips, 2007; Murphy, 2000]. But the corresponding interpretations raise the following major problems. (1) The Tanymas suture in the Pamir would have no counterpart in Tibet (Figure 18), while most authors agree that it corresponds both in age and geodynamic significance to the Jinsha suture. (2) Because the Rushan-Pshart and the Jinsha sutures not only have a different age but also a different vergency, it is impossible to match them together. (3) Similarly, matching the Shyok suture with the Bangong suture is just as unlikely. In fact the Shyok back-arc basin (90-110 Ma) was forming at a time when the Bangong realm of the Tethys was in its final stage of closure (100-140 Ma). It seems thus clear that the larger offsets of ~550, ~480, and ≥200 from north to south along the KF are the only ones that make sense (Table 13).

Offsets appear to decrease from NW to SE along the KFZ. This might indicate that the Tertiary KFZ initiated in its NW part and/or has a faster slip rate in that section. Alternatively, part of the offset in the NW could be inherited from older deformation phases. For example the two largest offsets, between the Triassic (Jinsha / Tanymas) and the Early Cretaceous (Bangong / Rushan-Pshart) sutures, could have accrued along a proto KFZ. Since there is little additional evidence to argue for such a proto KFZ, we have chosen to calculate the slip rates corresponding to the above offsets assuming that all are of Tertiary age (Table 13). Such rates thus correspond to maximum estimates. Dismissing the new age results presented here and assuming that the KFZ is of upper Miocene age (A on Figure 17b), and considering the most improbable smaller offsets, would yield rates between ~6.6 and 11 mm/yr (Table 13, italic). With the larger, and more realistic, offsets the rates increase in the 15 to 38 mm/yr range (Table 13, bold italic). For an Oligo-Miocene KFZ (C on Figure 17b) the larger offsets yield rates between ≥8 and 27 mm/yr (Table 13, bold).

For the southern half of the KFZ, the long-term rates (≥ 8-10 mm/yr, Table 13) are in good agreement with that deduced from the Indus river offset (≥ 8.5±1.5 mm/yr., Valli et al., 2007], with those derived from Quaternary moraines (10.7±0.7mm/yr, Chevalier et al., 2005], as well as with the geodectic rate of Barnejee and Bürgmann [2002] (11±4 mm/yr). Reasons why other geodetic rates, 3.4±5 mm/yr [Jade at al., 2004] and 1±3 mm/yr [Wright et al., 2004], appear to be lower than even the lowest geologic rate (6.6 mm/yr [Murphy et al., 2000]) remain to be understood.

### *5.7. Conclusion*

The North Ayilari shear zone was right-lateral prior to ~22.7 Ma ago. This suggests that the Karakorum fault zone is active since at least the Oligo-Miocene. The occurrence of several Oligo-Miocene granites outcropping along the fault zone, some of which showing evidence for synkinematic emplacement, suggest that the KFZ may have played an important role in the creation and /or collection of crustal melts. Considering the most realistic reconstructions of suture zones on both sides of the fault yield integrated rates ≤27 mm./yr in the northern strand of the fault zone decreasing to ≥ 8 to 10 mm/yr along the Southern strand. Dismissing the geochronological results presented in this paper and considering a Miocene age for the onset of the KFZ would significantly increase the fault rates. The KFZ cannot be considered as a small transient fault as it appears to have stayed stable through the Miocene, and have absorbed more than 200 km of displacement for an integrated fault rate on the order of 1 cm/yr.

## Acknowledgments

We would like to thank W. J. Dunlap, R. Weinberg and R. Phillips for constructive and detailed reviews of a first version of the paper; as well as Y. Rolland, an anonymous reviewer and L. Ratschbacher for the final version. Field and analytic work were supported by the programs “Intérieur de la Terre” (IT) and “Dynamique et Evolution de la Terre Interne (DYETI)” of CNRS-INSU and by the Institute of Geology, Chinese academy of Geological Sciences, Beijing, China. Access to the Cameca IMS 1270 (CRPG Nancy) was possible in the framework of INSU Service National. This is IPGP contribution X.

**References cited**

Armijo, R., P. Tapponnier, J. L. Mercier, and H. Tonglin (1986), Quaternary extension in southern Tibet : field observations and tectonic implications, *J. Geophys. Res.*, *91* (14), 13,803-13,872.

Armijo, R., P. Tapponnier, and H. Tonglin (1989), Late Cenozoic right-lateral strike-slip faulting in southern Tibet, *J. Geophys. Res., 94*, B3, 2787-2838.

Arnaud, N. (1992), Apports de la thermochronologie $^{40}Ar/^{39}Ar$ sur feldspath potassique à la connaissance de la tectonique cénozoïque d'Asie, Phd thesis, 155 pp., Université de Clermont-Ferrand.

Berthé, D., P. Choukroune, and D. Gapais (1979a), Orientations préférentielles du quartz et orthogneissification progressive en régime cisaillant: l'exemple du cisaillement sud-armoricain, *Bull. Mineral.*, *102*, 265-272.

Berthé, D., P. Choukroune, and P. Jegouzo (1979b), Orthogneiss, mylonite and non coaxial deformation of granites: the example of the South Amorican Shear-Zone, *J. Struct. Geol.*, *1*, 31-42.

Bhutani, R., K. Pande, and N. Desai (2003), Age of the Karakorum fault activation: 40Ar/39Ar geochronological study of Shyok suture zone in northern Ladakh, India Current Science, 84, 1454-1458.

Black, L. P., S. L. Kamo, C. M. Allen, J. N. Aleinikoff, D. W. Davis, R. J. Korsch, and C. Foudoulis (2003), TEMORA 1: a new zircon standard for Phanerozoic U-Pb geochronology, *Chem. Geol.*, *200*, 155-170.

Borges, F. S., and S. H. White (1980), Microstructural and chemical studies of sheared anorthosites, Roneval, South Harris, *J. Struct. Geol.*, *2*, 273-280.

Braun, I., JM. Montel, and C. Nicollet (1998), Electron microprobe dating of monazite from high-grade gneisses and pegmatites of the Kerala Khondalite Belt, southern India, *Chem. Geol.*, *146*, 65-85.

Brunel, M., N. Arnaud, P. Tapponnier, Y. Pan, and Y. Wang (1994), Kongur shan normal fault: type example of mountain building assisted by extension (karakoram fault, eastern Pamir), *Geology*, *22*, 707-710.

Catlos E. J., C. S. Dubey, T. M. Harrison, and M. A. Edwards (2004), Late Miocene movement within the Himalayan Main Central Thrust shear zone, Sikkim, north-east India,, *J. Metam. Geol.* 22 (3), 207-226.

Chappell, B. J., and A. J. R. White (1974), Two contrasting granite types, *Pac. Geol.*, *8*, 173-174.

Cherniak, D. J., and E. B. Watson (2001), Pb diffusion in zircon, *Chem. Geol.*, *172*, 5-24.

Cherniak, D. J., and E. B. Watson (2003), Diffusion in Zircon, in *ZIRCON*, edited by J.M. Hanchar, and P.W.O. Hoskin, pp. 113-143, Mineral. Soc. Am., 53.

Cherniak, D. J., E. B. Watson, T. M. Harrison, and M. Grove (2000), Pb diffusion in monazite: a progress report on a combined RBS/SIMS study, *Eos, Transactions (Suppl)*, *41*, S25.

Cherniak, D. J., E. B. Watson, M. Grove, and T. M. Harrison (2004), Pb diffusion in monazite: A combined RBS/SIMS study, *Geochim. Cosmochim. Acta*, *68* (4), 829-840.

Chevalier, M.-L., F. J. Ryerson, P. Tapponnier, R. C. Finkel, J. Van Der Woerd, Li Haibing, Liu Qing (2005), slip-Rate Measurements on the Karakorum Fault May Imply Secular Variations in Fault Motion, *Science* 21, Vol. 307. no. 5708, pp. 411 – 414.

Cocherie, A., O. Legendre, JJ. Peucat, and A. N. Kouamelan (1998), Geochronology of polygenetic monazites constrained by in situ electron microprobe Th-U-total Pb determination: Implications for lead behaviour in monazite, *Geochim. Cosmochim. Acta*, *62*, 2475-2497.

Compston, W., I. S. Williams, and C. Meyer (1984), U-Pb geochronology of zircons from lunar breccia 73217 using a sensitive high mass-resolution ion microprobe, *J. Geophys. Res.*, *89 Supplement*, B525-B534.

Dahl, P. S. (1997), A crystal-chemical basis for Pb retention and fission-track annealing systematics in U-bearing minerals, with implications for geochronology, *Earth Planet. Sci. Lett.*, *150*, 277-290.

Deloule, E. C., M. Chaussidon, B. P., Glass, and C. Koeberl (2001), U-Pb isotopic study of relict zircon inclusions recovered from muong nong-type tektites, *Geochim. Cosmochim. Acta*, *65* (11), 1833-1838.

Deng, W. M. (1989), Volcanism in Tibet, Journal of Natural Resources, 3, 205-210.

de Sigoyer, J., Guillot, S. and Dick, P., 2004. Exhumation Processes of the high-pressure low-temperature Tso Morari dome in a convergent context (eastern-Ladakh, NW-Himalaya). *Tectonics*, 23, No. 3, TC3003 - 10.1029/2002TC001492.

Dunlap, W. J., R. F. Weinberg, and M. P. Searle (1998), Karakoram fault zone rocks cool in two phases, *J. Geol. Soc. London*, *155*, 903-912.

Eisbacher, G. H. (1970), Deformation mechanics of mylonitic rocks and fractured granites in Cobequid Mountains, Nova Scotia, *Can. Bull. Geol. Soc. Am.*, *81*, 2009-2020.

England, P. C., and G. Houseman (1986), Finite strain calculations of continental deformation, 2. comparison with the India-Asia collision zone, *J. Geophys. Res., 91*, 3664-3676.

Fraser, J. E., M. P. Searle, R. R. Parrish, and S. R. Noble (2001), Chronology of deformation, metamorphism, and magmatism in the southern Karakoram mountains, *Geol. Soc. Am. Bull.*, *113* (11), 1443-1455.

Gapais, D. (1989a), Les Orthogneiss : Structures, mécanismes de déformation et analyse cinématique, *Mem. Doc. CAESS*, *28*, 1-366.

Gapais, D. (1989b), Shear structures within deformed granites: mechanical and thermal indications, *Geology*, *17*, 1144-1147.

Gapais, D., and B. Barbarin (1986), Quartz fabric transition in a cooling syntectonic granite (hermitage massif, France), *Tectonophysics*, *125*, 357-370.

Gardien, V., A. B. Thompson, D. Grujic, and P. Ulmer (1995), Experimental melting of biotite + plagioclase + quartz ± muscovite assemblages and implications for crustal melting, *J. Geophys. Res.*, 100 (B8), 15,581-15,591.

Gates, A. E., and L. Glover (1989), Alleghanian tectono-thermal evolution of the dextral transcurrent hylas zone, Virginia Piedmont, USA, *J. Struct. Geol.*, *11*, 407-419.

Gebauer, D. (1996), A P-T-t-path for an (ultra?-) high-pressure ultramafic/mafic rock-association and its felsic country-rocks based on SHRIMP-dating of magmatic and metamorphic zircon domains; example: Alpe Arami (Central Swiss Alps), *Am. Geophys. Union*, 309-328.

Geology publishing house (1998), Geological map of Qinhai-Xizang plateau and adjacent areas; Geology publishing house, Beijing.

Girardeau, J., J. Marcoux, E. Fourcade, J.P., Bassoulet, T., Youking (1985), Xainxa ultramaphic rocks, central Tibet, China: tectonic environment and geodynamic significance, *Geology*, 13, 330-333.
Gower, J. W., and C. Simpson (1992), Phase boundary mobility in naturally deformed, high-grade quartzofeldspathic rocks: evidence for diffusional creep, *J. Struct. Geol.*, *14* (3), 301-313.
Guillopé, M., and JP. Poirier (1979), Dynamic recrystallisation during creep of single-crystalline halite: an experimental study, *J. Geophys. Res.*, 84, 5557-5567.
Hanchar, J. M., and R. L. Rudnick (1995), Revealing hidden structures: The application of cathodoluminescence and back-scattered electron imaging to dating zircons from lower crust xenoliths, *Lithos*, *36*, 289-303.
Harrison, T.M., P. H. Leloup, F.J. Ryerson, P. Tapponnier, R. Lacassin, and W. Chen (1996), Diachronous initiation of transtension along the Ailao Shan-Red River shear zone, Yunnan and Vietnam, in *The tectonic evolution of Asia*, edited by A. Yin and T.M. Harrison, 208-226, Cambridge Univ. Press, New York.
Harrison, T. M., O. M. Lovera, and M. Grove (1997), New insights into the origin of two contrasting Himalayan granite belts, *Geology*, *25*, 899-902.
Harrison, T. M., M. Grove, K. D. McKeegan, C. D. Coath, O. M. Lovera , and P. Le Fort (1999), Origin and episodic emplacement of the Manaslu intrusive complex, Central Himalaya, *J. Petrol.*, *40* (1), 3-19.
Hirth, G., and J. Tullis (1992), Dislocation creep regimes in quartz aggregates, *J. Struct. Geol.*, *14*, 145-159.
Hollister, L. S., and M. L. Crawford (1986), Melt-enhanced deformation: a major tectonic process, *Geology*, *14*, 558-561.
Hoskin, P. W. O., and U. Schaltegger (2003), The Composition of Zircon and Igneous and Metamorphic Petrogenesis, in *ZIRCON*, edited by J. M. Hanchar, and P. W. O. Hoskin, pp. 26-62, Mineral. Soc. Am., 53.
Jensen, L. N., and J. Starkey (1985), Plagioclase microfabrics in a ductile shear zone from the Jotun Nappe, Norway, *J. Struct. Geol.*, *7* (5), 527-539.
Ji, S., and D. Mainprice (1990), Recrystallization and fabric development in plagioclase, *J. Geol.*, *98*, 65-79.
Jiao S., Y. Zhang, S. Yi, C. Ai, Y. Zhao, Y. Li, H. Wang, J. Xu, J. Hu, and T. Guo (1988), Geological map of Qinhai-Xizang Plateau and adjacent areas, *Map*, Geological Publishing House, Beijing.
Kapp, P., M. A. Murphy, A. Yin, and T. M. Harrison (2003), Mesozoic and Cenozoic tectonic evolution of the Shiquanhe area of western Tibet *Tectonics*, *22* (4), Art. no. 1029.
Kretz, R. (1983), Symbols for rock-forming minerals, *Am. Mineral.*, *68*, 227-279.
Lacassin, R., F. Valli, N. Arnaud, P. H. Leloup, JL. Paquette, H. Li, P. Tapponnier, ML. Chevalier, S. Guillot, G. Mahéo, and Z. Xu (2004a), Large-scale geometry, offset and kinematic evolution of the Karakorum fault, Tibet, *Earth Planet. Sci. Lett.*, *219*, 255-269.
Lacassin R., F. Valli, N. Arnaud, P. H. Leloup, JL. Paquette, Haibing Li, P. Tapponnier, ML. Chevalier, S. Guillot, G. Maheo, and Z. Xu (2004b), Reply to Comment on "Large-scale geometry, offset and kinematic evolution of the Karakorum fault, Tibet', *Earth Planet. Sci. Lett.*, 229 (1-2), 159-163.
Lee, J., I. Williams, and D. J. Ellis (1997), Pb, U and Th diffusion in natural zircon, *Nature*, *390*, 159-163.
Leloup, P. H., T. M. Harrison, F. J. Ryerson, W. Chen, Q. Li, P. Tapponnier, and R. Lacassin (1993), Structural, petrological and thermal evolution of a Tertiary ductile strike-slip shear zone, Diancang shan, Yunnan, *J. Geophys. Res.*, *98* (B4), 6715-6743.

Leloup, P. H., R. Lacassin, P. Tapponnier, D. Zhong, X. Liu, L. Zhang, S. Ji, and P. T. Trinh (1995), The Ailao Shan-Red River shear zone (Yunnan, China), Tertiary transform boundary of Indochina, *Tectonophysics*, *251*, 3-84.

Leloup, P. H., Y. Ricard, J. Battaglia, and R. Lacassin (1999), Shear heating in continental strike-slip shear zones: model and field examples, *Geophys. J. Int.*, *136*, 19-40.

Leloup, P. H., N. Arnaud, R. Lacassin, J. R. Kienast T. M. Harrison, P. T. Trinh, A. Replumaz, and P. Tapponnier (2001), New constraints on the structure, thermochronology and timing of the Ailao Shan - Red River shear zone, *J. Geophys. Res.*, *106(B4)*, 6657-6671.

Liu, J., and Y. Maimaiti (1989), Distribution and ages of Ashikule volcanoes on the West Kunlun mountains, west China, *Bulletin of Glacial Research*, *7*, 187-190.

Liu, Q. (1993), Paléoclimats et contraintes chronologiques sur les mouvements récents dans l'ouest du Tibet: failles du Karakorum et de Longmu Co - Gozha Co, lacs en pull-apart de Longmu Co et de Sumxi Co, *Phd Thesis*, 360 pp., Université Paris 7.

Ludwig, K. R. (2003), Isoplot 3.00 a geochronological toolkit for Microsoft Excel, *Berkley Geochronology Center Special Publication No. 4*.

Mahéo, G., S. Guillot, J. Blichert-Toft, Y. Rolland, and A. Pêcher (2002), A slab breakoff model for the Neogene thermal evolution of South Karakorum and South Tibet, *Earth Planet. Sci. Lett.*, *195* (1-2), 45-58.

Mahéo, G., A. Pêcher, S. Guillot, Y. Rolland, and C. Delacourt (2004), Exhumation of Neogene gneiss dome between two oblique crustal boundaries in south Karakorum (NW, Himalaya, Pakistan). In: " Gneiss Domes in Orogeny", Whitney, D.L., Teyssier, C., and Siddoway, C.S., editors, *Geol. Soc. Am. Spec. Pap.*, 380, 141-154.

Matte, P., P. Tapponnier, N. Arnaud, L. Bourjot, J. P. Avouac, P. Vidal, Q. Liu, Y. Pan, and Y. Wang (1996), Tectonics of Western Tibet, between the Tarim and the Indus, *Earth Planet. Sci. Lett.*, *142*, 311-330.

Miller, C., R. Schuster, U. Klötzli, W. Frank, and F. Purtscheller (1999), Post-collisional potassic and ultrapotassic magmatism in SW Tibet: geochemical and Sr-Nd-Pb-O isotopic constraints for mantle source characteristics and petrogenesis, J. Petrol., 40 (9), 1399-1424.

Ministry of geology of USSR (1989), Geological map of Tadjikistan, USSR republic, and adjacent territories, *Map*, Vsesojuznoi Geol. Inst. Leningrad, Leningrad.

Möller, A., P. J. O'Brien, A. Kennedy, and A. Kröner (2002), Polyphase zircon in ultrahigh-temperature granulites (Rogaland, SW Norway): constraints for Pb diffusion in zircon, *J. Metamorph. Geol.* 20, 727-740.

Montel, J., J. Kornprobst, and D. Vielzeuf (2000), Preservation of old U-Th-Pb ages in shielded monazite: example from Beni Bousera Hercynian kinzigites (Morocco), *J. Metamorph. Geol.* 18, 335-342.

Moore, D. E., S. Hickman, D. A. Lockner, and P. F. Dobson (2001), Hydrothermal minerals and microstructures in the Silangkitang geothermal field along the Great Sumatran fault zone, Sumatra, Indonesia, *Geol. Soc. Am. Bull.*, *113* (9), 1179-1192.

Murphy, M. A., A. Yin, P. Kapp, T. M. Harrison, L. Ding, J. Guo (2000), Southward propagation of the Karakoram fault system, Southwest Tibet; timing and magnitude of slip, *Geology (Boulder)*, *28* (5), 451-454.

Murphy, M. A., A. Yin, P. Kapp, T. M. Harrison, C. E. Manning, F. J. Ryerson, L. Ding, and J. Guo (2002), Structural evolution of the Gurla Mandhata detachment system, Southwest Tibet; implications for the eastward extent of the Karakoram fault system, *Geol. Soc. Am. Bull.*, *114* (4), 428-447.

Olesen, N. O. (1987), Plagioclase fabric development in a high-grade shear zone, Jotunheimen, Norway, *Tectonophysics*, *142*, 291-308.

Olsen, T. S., and D. L. Kohlstedt (1985), Natural deformation and recrystallisation of some intermediate plagioclase feldspars, *Tectonophysics*, *111*, 107-131.

Paquette J.L., and C. Pin (2001), A new miniaturized extraction chromatography method for precise U-Pb zircon geochronology, *Chem. Geol., 176*/1-4, 313-321.

Parrish, R. R. (1987), An improved micro-capsule for zircon dissolution in U-Pb geochronology, *Chem. Geol.*, *66*, 99-102.

Parrish, R. R., and R. Tirrul (1989), U-Pb age of the Baltoro granite, northwest Himalaya, and implications for monazite U-Pb systematics, *Geology*, *17*, 1076-1079.

Passchier, C. W. (1982), Mylonitic deformation in the Saint Barthélemy Massif, French Pyrenees, with emphasis on the genetic relationship between ultramylonite and pseudotachylyte, *GUA Pap. Geol. Ser. 1*, *16*, 1-173.

Passchier, C. W., and R. A. J. Trouw (1996), *Microtectonics*, 289 pp., Springer-Verlag, Berlin.

Peltzer, G., and P. Tapponnier (1988), Formation and evolution of strike-slip faults, rifts, and basins during the India-Asia collision: an experimental approach, *Journal of Geophysical Research, 93*, 15085-15117.

Phillips, R. J., R. R. Parrish, and M. P. Searle (2004), Age constraints on ductile deformation and long-term slip rates along the Karakoram fault zone, Ladakh, *Earth Planet. Sci. Lett.*, *226*, 305-319.

Phillips, R. J., and M. P. Searle (2007), Macrostructural and microstructural architecture of the Karakoram fault: relationship between magmatism and strike-slip faulting, *Tectonics*, *26*, TC3017, doi:10.1029/2006TC001946.

Pognante U. (1991), Shoshonitic and ultrapotassic post-collisional dykes from northern Karakorum (Sinkiang, China), *Lithos* 26 (3-4), 305-316.

Pryer, L. L. (1993), Microstructures in feldspars from a major crustal thrust zone: the Grenville Front, Ontario, Canada, *J. Struct. Geol.*, *15*, 21-36.

Ratschbacher, L., Frisch, W., Liu, G. and C.C. Cheng (1994), Distributed deformation in Southern and Western Tibet as result of the India-Asia collision. *J. Geophys. Res.*, 99, B10, 19917-19945.

Ritts, B. D., and U. Biffi (2000), Magnitude of post-Middle Jurassic (Bajocian) displacement on the Altyn Tagh fault, NW China, *Geol. Soc. Am. Bull.*, *112*, 61-74.

Ritts, B. D., Y. J. Yue, and S. A., Graham (2004), Oligocene-Miocene tectonics and sedimentation along the Altyn Tagh Fault, northern Tibetan Plateau: Analysis of the Xorkol, Subei, and Aksay basins *J. Geol*, *112* (2), 207-229.

Rolland, Y. (2002), From intra-oceanic convergence to post-collisional evolution; example of the India-Asia convergence in NW Himalaya, from Cretaceous to present, In: Rosenbaum, G. and Lister, G. S. (eds.), Reconstruction of the evolution of the Alpine-Himalayan Orogen , *Journal of the Virtual Explorer*, 8, 193-216.

Rolland, Y., Pecher, A., and Picard, C. (2000), Middle Cretaceous back-arc formation and arc evolution along the Asian margin: the Shyok Suture Zone in northern Ladakh (NW Himalaya): Tectonophysics, v. 325, p. 145-173.

Rolland, Y., and A. Pêcher (2001), The Pangong granulites of the Karakoram Fault (Western Tibet): vertical extrusion within a lithosphere-scale fault ?, *C. R. Acad. Sci.*, *332*, 363-370.

Rolland, Y., A. Pêcher, G. Mahéo, I. M. Villa, Syn-kinematic emplacement of the Pangong metamorphic and magmatic complex along the Karakorum Fault (N Ladakh), J. Asian Earth Sciences, In press.

Ronghua, X., Z. Yuquan, X. Yingwen, P. Vidal, N. O. Arnaud, Z. Qiaoda and D. Z. (1996), Isotopic geochemistry of plutonic rocks. Geological evolution of the Karakorum and Kunlun mountains. P. Yusheng. Beijing, *Seismological press*, 137-186.

Rubatto, D., and D. Gebauer (1998), Use of cathodoluminescence for U-Pb zircon dating by ion microprobe (SHRIMP): some examples from high-pressure rocks of the Western Alps, in *Cathodoluminescence in Geosciences*, edited by M. Pagel, V. Barbin, P. Blanc, and D. Ohnenstetter, pp. 373-400, Springer-Verlag, Berlin.

Rubatto, D., I. S. Williams, and I. S. Buick (2001), Zircon and monazite response to prograde metamorphism in the Reynolds Range, Central Australia, *Contrib. Mineral. Petrol.*, *140*, 458-468.

Schärer, U. (1984), The effect of initial $^{230}$Th disequilibrium on young U-Pb ages: the Makalu case, Himalaya, *Earth Planet. Sci. Lett.*, 67, 191-204.

Schärer, U., J. Hamet, and C. J. Allègre (1983), The Transhimalaya (Gangdese) plutonism in the Ladhak region: a U-Pb and Rb-Sr study, *Earth Planet. Sci. Lett.*, *67*, 327-339.

Schärer, U., T. M. Harrison, and M. P. Searle (1990), Age, cooling history and origin of post-collisional leucogranites in the Karakoram batholith; a multi-system isotope study N. Pakistan, *J. Geol.*, *98*, 233-251.

Schärer, U., J., Kornprobst, M. O. Beslier, G. Boillot, and J. Girardeau (1995), Gabbro and related rock emplacement crust: U-Pb geochronological and geochemical constraints for the Galicia passive margin (Spain), *Earth Planet. Sci. Lett.*, *130*, 187-200.

Schwab, M., L. Ratschbacher, W. Siebel, M. McWilliams, V. Minaev, V. Lutkov, F. Chen, K. Stanek, B., Nelson, W. Frisch, and J. L. Wooden (2004), Assembly of the Pamirs: Age and origin of magmatic belts from the southern Tien Shan to the southern Pamirs and their relation to Tibet, *Tectonics*, *23*, TC4002, doi:10.1029/2003TC001583.

Searle, M. P. (1991), Geology and Tectonics of the Karakoram Mountains, *Map 2538*, John Wiley and Sons, Chichester.

Searle, M. P. (1996), Geological evidence against large-scale pre-Holocene offsets along the Karakoram Fault: Implications for the limited extrusion of the Tibetan plateau, *Tectonics*, *15* (1), 171-186.

Searle, M. P., and R. J. Phillips (2004a), A comment on "Large-scale geometry, offset, and kinematic evolution of the Karakoram fault, Tibet" by R. Lacassin et al. *Earth Planet. Sci. Lett.*, 229 (1-2), 155-158.

Searle, M. P., and R. J. Phillips (2007), Relationships between right-lateral shear along the Karakorum fault and metamorphism, magmatism, exhumation and uplift: evidence from the K2-Gasherbrum-Pangong ranges, north Pakistan and Ladakh, *Journal of the Geological Society, London*, 164, 439-450.

Searle, M. P., M. B. Crawford, and A. J. Rex (1992), Field relations, geochemistry, origin and emplacement of the Baltoro granite, central Karakoram, *Transactions of the Royal Society of Edinburgh, Earth Science*, *83*, 519-538.

Searle, M. P., R. F. Weinberg, and W. J. Dunlap (1998), Transpressional tectonics along the Karakoram fault zone, northern Ladakh: constraints on Tibetan extrusion, in *Continental Transpressional and Transtensional Tectonics,* edited by R. E. Holdsworth, R. A. Strachan, and J. F. Dewey, Geol. Soc., London, Spec. Pub., 135, 307-326.

Seydoux-Guillaume, AM., JL. Paquette, M. Wiedenbeck, JM. Montel, and W. Heinrich (2002), Experimental resetting of the U-Th-Pb systems in monazite, *Chem. Geol.*, *191* (1-3), 165-181.

Simpson, C., and R. P. Wintsch (1989), Evidence for deformation-induced K-feldspar replacement by myemekite, *J. Metam. Geol.*, *7*, 261-275.

Smith, H. A., and B. J. Giletti (1997), Lead diffusion in monazite, *Geochim. Cosmochim. Acta*, *61*, 1047-1055.

Spear, F. S., and R. R. Parrish (1996), PTt evolution of the Valhalla Complex, British Columbia, Canada, *J. Petrol., 37*, 733-765.

Stacey, J. S., and J. D. Kramers (1975), Approximation of terrestrial lead isotope evolution by a two-stage model, *Earth Planet. Sci. Lett.*, 26, 207-221.

Steck, A. (2003), Geology of the NW Indian Himalaya, *Eclog. Geol. Helv.*, *96* (2), 147-196.

Stern, R. A. (1997), The GSC sensitive high resolution ion microprobe (SHRIMP) : analytical techniques of zircon U-Th-Pb age determinations and performance evaluation. Radiogenic age and isotopic studies: report 10, *Geol. Surv. Can., Curr. Res.*, 1-31.

Stern, R. A., and N. Sanborn (1998), Monazite U-Pb and Th-Ph geochronology by high-resolution secondary ionmass spectrometry ; in Radiogenic age and isotopic studies: report 11, *Geol. Surv. Can., Curr. Res.*, 1-18.

Stern, R. A., and Y. Amelin (2003), Assessment of errors in SIMS zircon U-Pb geochronology using a natural zircon standard and NIST SRM 610 glass, *Chemical Geol.*, 197 (1-4), 111-142.

Stesky, R. M. (1978), Mechanisms of high temperature frictional sliding in Westerly granite, *Can. J. Earth Sci.*, *15*, 361-375.

Stesky, R. M., W. F. Brace, D. K. Riley, and P. Y. F. Robin (1974), Friction in faulted rock at high temperature and pressure, *Tectonophysics*, *23*, 177-203.

Stünitz, H. (1998), Syndeformational recrystallization - dynamic or compositionally induced?, *Contrib. Mineral. Petrol.*, *131*, 219-236.

Stutz, E. and A. Steck (1986), La terminaison occidentale du cristallin du Tso Morari (Haut Himalaya, Laddakh méridional, Inde), *Eclogae Geol. Helv.*, 79, 253-269.

Tapponnier, P., G. Peltzer and R. Armijo (1986), On the mechanics of the collision between India and Asia, in *Collision Tectonics*, *Geol. Soc. London Spec. Pub.*, 19, 115-157.

Tapponnier, P., Xu Zhiqin, Roger, F., Meyer, B., Arnaud, N., Wittlinger, G., and Yang Jingsui (2001), Oblique stepwise rise and growth of the Tibet plateau, *Science*, 294, 1671-1677.

Tera, F., and G. Wasserburg (1972), U-Th-Pb systematics in three Apollo 14 basalts and the problem of initial Pb in lunar rocks, *Earth Planet. Sci. Lett.*, *14*, 281-304.

Thompson, A. B., and J. A. D. Connolly (1995), Melting of the continental crust: some thermal and petrological constraints on anatexis in continental collision zones and other tectonic settings, *J. Geophys. Res.*, *100* (B8), 15,565-15579.

Tsurumi, J., H. Hosonuma, and K. Kanagawa (2003), Strain localization due to a positive feedback of deformation and myrmekite-forming reaction in granite and aplite mylonites along the Hatagawa Shear Zone of NE Japan, *J. Struct. Geol.*, *25*, 557-574.

Tullis, Y. E., and R. A. Yund (1987), Transition from cataclastic flow to dislocation creep of feldspar: mechanisms and microstructures, *Geology*, *15*, 606-609.

Tullis, T. E., and R. A. Yund (1991), Diffusion creep in feldspar aggregates: experimental evidence, *J. Struct. Geol.*, *13*, 987-1000.

Valli, F. (2005), Décrochements lithosphériques dans l'Ouest du plateau du Tibet : Géométrie, âge, décalages cumulés et vitesse de glissement long-terme sur la Faille du Karakorum, *Phd Thesis*, 404 pp., Institut de Physique du Globe de Paris.

Valli, F., N. Arnaud, P. H. Leloup, E. R. Sobel, G. Mahéo, R. Lacassin, S. Guillot, H. Li, P. Tapponnier, and Z. Xu (2007), Twenty million years of continuous deformation along the Karakorum fault, western Tibet: A thermochronological analysis, *Tectonics*, 26, TC4004, doi:10.1029/2005TC001913.

Vavra, G., D. Gebauer, R. Schmid, and W. Compston (1996), Multiple zircon growth and recrystallization during polyphase Late Carboniferous to Triassic metamorphism in granulites of the Ivrea Zone (Southern Alps): an ion microprobe (SRHIMP) study, *Contrib. Mineral. Petrol.*, *122*, 337-358.

Weinberg, R. F., and M. P. Searle (1998), The Pangong Injection Complex, Indian Karakoram: A case of pervasive granite flow through hot viscous crust, In: Granitic magma dynamics, Clemens J. D. (convener), *J. Geol. Soc. London*, 155 (5), 883-891.

Weinberg, R. F., and W. J. Dunlap (2000), Growth and deformation of the Ladakh batholith, northwest Himalayas: implications for timing of continental collision and origin of calc-alkaline batholiths, *J. Geol.*, 108, 303-320.

Weinberg, R. F., W. J. Dunlap, and M. Whitehouse (2000), New field, structural and geochronological data from the Shyok and Nubra valleys, northern Ladakh: linking Kohistan to Tibet, in *Tectonics of the Nanga Parbat syntaxis and the western Himalaya*, edited by M. A. Khan, P. J. Treloar, M. P. Searle, M. Q. Jan, pp. 253-275, Geol. Soc. London Spec. Pub.

White, J. C., and C. K. Mawer (1986), Extreme ductility of feldspars from a mylonite, Parry Sound, Canada, *J. Struct. Geol.*, *8*, 133-143.

White, S. (1975), Tectonic deformation and recrystallisation of oligoclase, *Contrib. Mineral. Petrol.*, *50*, 287-304.

Wiedenbeck, M., P. Alle, F. Corfu, W. L. Griffin, M. Meier, F. Oberli, A. Von Quadt, J. C. Roddick, and W. Spiegel (1995), Three natural zircon standards for U-Th-Pb, Lu-Hf, trace element and REE analyses, *Geostandards Newsletter*, *19* (1), 1-23.

Xie, Y., Y. Zhang, R. Xu, N. Arnaud, and P. Vidal (1992), Characteristics and geological implication of the alkaline complex pluton of Taxkorgan, in *International symposium on the Karakorum and Kunlun mountains*, Kashi.

Yin et al., GSA Bulletin, 1999, v111, n 11, p1644-1664.

Yue, Y., B. D. Ritts, and S. A. Graham (2001), Initiation and long-term slip history of the Altyn Tagh fault, *International Geology Review*, *43*, 1087-1093.

**Tables:**

**Table 1:** Table 1: Location (see also Figures 1, 2) and description of dated samples. Fo: foliation, Li: lineation, az: azimuth, Mz: monazite, Zr: zircon

**Table 2:** Migmatitic gneiss L89 zircon SHRIMP II data. Results are presented by increasing $^{206}Pb/^{238}U$ ages. CL domains (within brackets when unclear): C, core; R, Rim; O oscillatory; n.d. not defined. Type, type of event on which the analyzed domain will provide an age constrain, Ma, magmatic; Me, Metamorphic. Th, and U concentration calculated following Stern [1997]. n.s., not significant. * represent the radiogenic component.

**Table 3:** Migmatitic gneiss L89 monazite SHRIMP II data. Results are presented by ascending $^{206}Pb/^{238}U$ ages. Structural location refer to the shape and position of the monazite crystal with respect to the surrounding minerals (Figure 10): It, interstitial; Ic, included, and the following abbreviation indicates the mineral in which the monazite is included. Bt., biotite; fs., Feldspar; Chl, Chlorite. Th and U concentrations are calculated following Stern and Stanborn [1998]. * represent the radiogenic component.

**Table 4:** Sample C43 sheared two-mica leucogranitoid zircons SHRIMP II data. Similar caption as Table 2.

**Table 5:** C32 (= K1C32 of *Lacassin et al.* [2004a]) and C43 ID-TIMS U–Pb isotope data for monazite (m) and zircon (z). [ ] number of grains of the analyzed fraction. ab. = air abraded, an. = anhedral, cl. = colourless, lp. = long prismatic, need. = needle shaped (acicular), pi. =

pink, sp. = short prismatic , un. = unabraded, ye. = Yellow. The ± numbers represent the errors made on the last digit.

**Table 6:** Leucocratic mylonite P34 zircon SHRIMP II data. Same caption as Table 2. Re, re-crystallized.

**Table 7:** Sheared two-mica granitoid P18 zircons SHRIMP II data. Same caption as Table 2.

**Table 8:** Sheared two-mica granitoid P18 Monazite SHRIMP II data. Same caption as Table 2.

**Table 9:** Sheared biotite-rich granitoid P20 zircon Cameca IMS 1270 data. Similar caption as Table 2.

**Table 10:** K2P30 ID-TIMS U–Pb isotope data for zircon. Same caption as Table 5.

**Table 11:** Summary of ID-TIMS, SHRIMP II and Cameca IMS 1270 ages. Average ages in Ma of zircon/monazite grains populations are reported in bold with the corresponding 95% confidence level error (xx.x±x.x). Coresponding individual ages range of the population (xx.x – xx.x)with extremum 2 σ errors (+x.x, -x.x) and number of individual ages [n] are also given. Magmatic and, metamorphic / Hydrothermal zircons are distinguished from their crystal shape, color, Th/U ratio, U content and BSE – CL patterns, see text for details.

**Table 12:** Published timing constraints ages of shearing onset and Miocene magmatism along the KFZ. Only the longitude along the fault is given for location. See Figure 17 and text sections 5.4 and 5.5.

**Table 13:** Estimates of suture zones offsets across the KFZ and corresponding finite fault rates. Preferred offsets are in bold. Some offsets of *Lacassin et al*. [2004] were measured for the whole ~80 km wide Karakorum deformation zone. In this study, corresponding offsets are measured from piercing points on the trace of the active fault. In any case, uncertainties on measured offsets are difficult to estimate but could reach a few tenths of kilometres. Rates are calculated using initiation ages [A] (italic) and [C] shown in Figure 17b. Preferred rates are bold. See text section 5.6 and Figure 18.

**Figure Captions:**

**Figure 1:** structural map of western Tibet showing Karakorum fault zone and adjacent units. Inset shows location in large-scale Asian active tectonic framework. Faults are mapped from *Brunel et al.* [1994], *Lacassin et al.* [2004a], *Ministry of Geology of USSR* [1989], *Tapponnier et al.* [2001], and *Weinberg and Dunlap* [2000]. The Oligo-Miocene magmatic intrusions are mapped from this study, *Dunlap et al.* [1998], *Lacassin et al.* [2004a], *Phillips et al.* [2004], *Searle* [1991], and *Searle et al.* [1992; 1998]. Contours for the ultrapotassic and potassic volcanism, together with North and High Himalayan granites are from [*Arnaud,* 1992; *Deng,* 1989; *Harrison et al.,* 1997; 1999; *Jiao et al.,* 1988; *Liu et Maimaiti*, 1989; *Miller et al.,* 1999]. PU, Plutonic Unit; GMDS, Gurla Mandhata detachement system; TSZ, Thanglasgo Shear Zone; SF Shigar fault; SKF South Karakorum fault; MBT Main boundary thrust; MMT main mantle thrust; MCT main central thrust; MKT main Karakorum thrust. Different grey levels highlight the main blocks and the ophiolitic sutures separating them. Map projection is UTM 44, ellipsoid WGS84.

**Figure 2:** Geology of the North Ayilari range and samples location. **(a)** Geological map of the North Ayilari (NA) range between Zhaxigang and Gar. Drawn from field observations along the four cross-sections depicted in green (see detailed sections in Figure 4 of *Valli et al.* [2007]), and satellite image interpretation (Landsat 7, Spot 5, and SRTM DEM). Light shading outlines topography. Section A-B corresponds to (b). Numbers near foliations symbols give the foliation dip. South West boundary of the North Ayilari dextral shear zone is crudely depicted by a dashed red line. Projection is UTM 44, ellipsoid WGS84. Figure 3 pictures are located. **(b)** Generalized cross-section of North Ayilari (NA) range northeastern flank, across the North Ayilari shear zone (NAsz) and active fault (NAaf). Drawn from extrapolation between field observations along cross sections shown in (a). U-Th/Pb samples are located with black arrows. Note that because magmatic rocks mapping (a) is mostly based on reflectance properties while section (b) is draw from direct field observations, the map is less detailed and the two legends differ.

**Figure 3:** North Ayilari range pictures showing structural relationships between magmatic and metamorphic rocks. **(a)** Flat lying migmatitic gneisses, section 1, see Figure 2. Lc: leucosome. The gneisses exhibit a N 140 trending lineation and top to the SE shear criteria (see b). **(b-d)** Rock thin sections perpendicular to foliation and parallel to lineation. **(b)** C/S structures in migmatitic gneisses (see a) indicating top to the SE shearing. Sample L89 (Figure 2). **(c)** Dextral shear planes. Sample P18, section 3 (Fig. 2). **(d)** σ-type feldspar mantled by dynamically re-crystallized grains in low stress areas; asymmetry indicates dextral shear sense (sample P34, section 2, Figure 2). **(e - g)** Variously deformed generations of syn-kinematic leucocratic dykes intruding the Kfz HT foliation. **(e)** Highly deformed leucocratic dykes (TLD) transposed parallel to the surrounding N140 trending HT foliation of the NAsz. Knife gives scale. **(f)** Outcrop 3A, section 3, see Figure 2 for location. TLD: transposed and highly deformed veins (see e), CLD: less deformed cross cutting veins (sample C32). Hammer gives scale, view from SW. **(g)** Leucocratic dykes transposed parallel to the NAsz HT foliation (TLD). Section 3, see Figure 2 for location. **(h)** undeformed leucocratic dyke (LD) crosscutting migmatitic gneisses. ML: melanosome. Hammer gives scale. Boulder falling from the flanks of a valley between section 1 and 2, see Figure 2a for location.

**Figure 4:** Examples of CL images of dated zircons. Ellipses show ion probe spots with corresponding $^{206}$Pb/$^{238}$U or $^{207}$Pb/$^{206}$Pb ages and Th/U ratio **a)** Tertiary zircons from migmatitic gneiss L89 (section 1, Figures 2, 3a-b, Table 2). **b)** zircons from C43 leucocratic orthogneiss (section 4, Figure 2, Table 4). **c)** mylonitic leucocratic gneiss P34 (section 2, Figure 2, Table 6). **d)** two-mica ortho-gneiss P18. Zircon grain Z3 exhibits a core surrounded by a darker rim while Zircon grain Z41 shows uniform oscillatory zoning without any clear rim-core domains (Table 7).

**Figure 5:** $^{206}$Pb/$^{238}$U vs. $^{207}$Pb/$^{235}$U Concordia diagram of SHRIMP II in-situ zircons ages of L89 migmatitic leucosome (section 1, Figures 2, 3a-b).

**Figure 6:** $^{208}$Pb/$^{232}$Th ages from in situ IMS 1270 microprobe dating of L89 migmatitic gneiss monazite grains (section 1, figures 2, 3a-b). Each bar shows result and uncertainty for one grain, and ages are grouped according to their structural position. The mineral phases in which monazites are included are specified. Bt., Biotite; fs, Feldspar; Chl, Chlorite. Errors are given at 2$\sigma$. Light gray rectangles represent the preferred mean ages for interstitial and included monazite populations (see text for details). Note that the vertical scale changes above 60 Ma.

**Figure 7:** U-Pb SHRIMP II ages of zircons from C43 leucocratic orthogneiss (section 4, Figure 2). **a**: Tertiary ages plotted in a Tera-Wasserburg diagram; white and black diamonds correspond to hydrothermal zircon rims and core, respectively. **b**: Magmatic zircon core ages plotted in a $^{206}$Pb/$^{238}$U vs. $^{207}$Pb/$^{235}$U Concordia diagram (Table 4).

**Figure 8:** U-Pb SHRIMP II ages of leucocratic mylonitic orthogneiss P34 zircons (section 2, Figures 2, 3d, Table 6). Same caption as Figure 7.

**Figure 9** U-Pb SHRIMP II results of zircons from the two-mica ortho-gneiss P18 (section 3, Figures 2, 3c, Table 7). **a**: Tertiary zircon ages plotted in a Tera-Wasserburg diagram; white and black diamonds correspond to zircon rims and the central part of uniformly zoned grains respectively; grey diamonds correspond to metamorphosed magmatic rims. **b**: Ages of CL bright zircon cores plotted in a $^{206}$Pb/$^{238}$U vs. $^{207}$Pb/$^{235}$U concordia diagram.

**Figure 10:** BSE images of monazites from the two-mica orthogneiss P18 (section 3, Figures 2, 3c, Table 8). Right: view of monazite surroundings, arrows point towards monazite location in the thin sections. Ap, apatite; Bt, biotite; K-fs, K-feldspar; Qtz, quartz; Pl, plagioclase. Left: detail of monazite crystals with ion probe spots and corresponding $^{208}$Pb/$^{232}$Th ages (2$\sigma$ error, Table 8).

**Figure 11:** $^{208}$Pb/$^{232}$Th ages from in situ IMS 1270 microprobe dating of monazites in the two-mica ortho-gneiss P18 (section 3, Figures 2, 3c, Table 8). Caption similar to Figure 7.

**Figure 12:** Tera-Wasserburg diagram of IMS1270 in-situ analyses of zircons from the biotite-rich gneiss P20 (section 3, Figure 2, Table 9).

**Figure 13:** Concordia diagram of ID-TIMS conventional multi-grain analysis of zircons (white and grey circles) and monazites (grey diamonds) from the crosscutting leucocratic dyke C32 (section 3, Figures 2, 3f). Errors smaller than symbols. See data in table 5.

**Figure 14:** Concordia diagrams ($^{206}Pb/^{238}U$ vs. $^{207}Pb/^{235}U$) of ID-TIMS multi-grain analysis of zircons from the Labhar Kangri granite K2P30 (Figure 1, Table 10).

**Figure 15:** Summary of Tertiary U-Th-Pb results. North Ayilari shear zone on left and Labhar Kangri on right. Zircons mean ages appear as diamonds, and monazites as circles. Error bars are $2\sigma$. No error bars are shown when they are smaller than symbol. Black and white diamonds are magmatic, and metamorphic/hydrothermal grains, respectively. Corresponding age ranges are respectively outlined by grey shade and hachure. See text sections 5.1 and 5.2 for details.

**Figure 16:** North Ayilari shear zone cooling history.

U-Th/Pb ages [This study] and Ar/Ar-FT-U/He colling histories [Valli et al., 2007] plotted as a function of temperature. Ages are plotted with a $2\sigma$ confidence level. The magmatic zircons and monazites are taken as constraining granitoid crystallization at ca 750-800°C [Clemens, 2003]. Closure temperatures of metamorphic / metasomatic zircons and monazites are unknown within a 700-400°C range and could plot anywhere in the dashed box, most ages being within the gray area (see text for discussion).

**Figure 17:** Constraints on KFZ initiation timing. **a)** Location of Post Eocene magmatism and suture zones in west Tibet. Oligo-Miocene magmatism along the KFZ shown in red. Faults are as on Figure 1. Ultrapotassic and potassic volcanism (orange) mapped from *Arnaud* [1992], *Deng* [1989], *Jiao et al.* [1988], *Liu et Maimaiti* [1989], *Miller et al.* [1999]. Contours of High and North Himalayan granites from *Harrison et al.* [1997; 1999]. Plutonic units along KFZ from this study, *Arnaud* [1992], *Dunlap et al.* [1998], *Jiao et al.* [1988], *Lacassin et al.* [2004a], *Phillips et al.* [2004], *Searle* [1991], *Searle et al.* [1992; 1998]. Map projection is World Mercator WGS84. LMC: Long Mu Co. **b)** Age constraints (Table 12) plotted as a function of distance along the fault. Origin of the x axis corresponding to NA section 3. Oligo-Miocene magmatic events plotted as red dots, constraints on the onset of the KFZ in green (see table 12). Four hypotheses (A to D) for the onset of the KFZ are depicted. See text section 5.4 for details.

**Figure 18:** Main sutures zones on both side of KFZ and proposed matches across it. Age of suturing and vergence of each suture are indicated. E. Early, L. Late, Pz Paleozoic, Mz Mesozoic, Tr Triassic, J Jurassic, K Cretaceous. North branch of KFZ is artificially widened in order to visualize the offsets (double arrows). Total offset of the Indus-Tzangpo suture for whole Karakorum deformation zone is also indicated, offset on North branch of KFZ being impossible to pin down because KFZ follows the suture. Offset values in km. Preferred matches are in colour while gray ones are proposed by Murphy et al.[2000] (Kailas thrust and molasses) and Searle and Phillips [2007]. See Table 13 and text section 5.6 for details.

| Sample | Range/section | lat (° ' ".) | long (° ' ".) | altitude (m) | Facies | structure | Zr U/Pb results | Mz U/Pb results |
|---|---|---|---|---|---|---|---|---|
| | | | | | | | | |
| L89 | North Ayilari / section 1 | N32°26'44.63" | E79°33'36.55" | 5046 | migmatitic leucosome | Fo: N60, 5N; Li az 140 | Fig. 5, Table 2 | Fig. 6, Table 3 |
| P34 | North Ayilari / section 2 | N32°25'00.40" | E79°42'06.10" | 4573 | leucocratic mylonitic gneiss | Fo: N134, 37N; Li az 134 | Fig. 8, Table 6 | |
| P18 | North Ayilari / section 3 | N32°23'28.90" | E79°43'35.00" | 4501 | two micas orthogneiss | Fo: N140, 50N; Li az 139 | Fig. 9, Table 7 | Fig. 11, Table 8 |
| P20 | North Ayilari / section 3 | N32°23'19.20" | E79°43'27.70" | 4633 | biotite-rich gneiss | Fo: N145 37N; Li az 139 | Fig. 12, Table 9 | |
| C32 | North Ayilari / section 3 | N32°23'17.60" | E79°43'25.30" | 4637 | leucocratic dyke | mild deformation, cross-cuts NW-SE foliation | Fig. 13, Table 5 | Fig. 13, Table 5 |
| C43 | North Ayilari / section 4 | N32°19'22.70" | E79°44'25.30" | 4797 | leucocratic orthogneiss | Little deformation, C/S structures | Fig. 7, Table 4 | Table 5 |
| K2P30 | Labhar Kangri | N30°28'59.20" | E83°02'22.30" | 5451 | granite | no deformation | Fig. 14, Table 10 | |

**Table 1:** Location (see also Figures 1, 2) and description of dated samples. Fo: foliation, Li: lineation, az: azimuth, Mz: monazite, Zr: zircon

| Spot name | Age (Ma) 206/238 | ± (2σ) | Age (Ma) 207/235 | ± (2σ) | Age (Ma) 207/206 | ± (2σ) | CL domain | 206/238 | ± % | 207/235 | ± % | U (ppm) | Th (ppm) | Th/U | Type | $^{206}Pb^*$ (ppm) | % com Pb |
|---|---|---|---|---|---|---|---|---|---|---|---|---|---|---|---|---|---|
| z34 | 23.4 | 4,0 | - | - | n.s. | | n.d. | 0.00363 | 17.4 | - | - | 1579 | 2497 | 1.75 | Ma | 9.6 | 52.7 |
| z28 | 34.7 | 2.4 | 33.1 | 18.8 | n.s. | | OC | 0.00539 | 6.8 | 0.0331 | 58 | 3041 | 3305 | 1.12 | Ma | 16 | 15.1 |
| z29 | 82.3 | 6.2 | 173 | 62 | 1711 | 690 | n.d. | 0.01284 | 7.6 | 0.1855 | 39.2 | 1126 | 55 | 0.05 | Ma-Me | 15 | 25.5 |
| z52 | 204 | 12 | 240 | 29 | 606 | 260 | n.d. | 0.03216 | 5.8 | 0.2664 | 13.6 | 2175 | 43 | 0.02 | Ma-Me | 63 | 4.7 |
| z27 | 333 | 20 | 342.1 | 64.6 | 404 | 470 | n.d. | 0.05301 | 6.2 | 0.4006 | 22.2 | 615 | 25 | 0.04 | Ma-Me | 29 | 3.1 |
| z36 | 342 | 21 | 351 | 56 | 408 | 390 | n.d. | 0.05452 | 6.4 | 0.4127 | 19 | 874 | 24 | 0.03 | Ma-Me | 43 | 4.5 |
| z40 | 349 | 20 | 340 | 30 | n.s. | | n.d. | 0.05557 | 6 | 0.3973 | 10.6 | 636 | 279 | 0.45 | Ma | 31 | 3.2 |
| z41 | 393 | 24 | 365 | 132 | n.s. | | n.d. | 0.06289 | 6.4 | 0.4319 | 43 | 483 | 242 | 0.52 | Ma | 29 | 12.6 |
| z30-2 | 395 | 23 | 413 | 55 | 517 | 330 | n.d. | 0.06319 | 5.8 | 0.5023 | 16.2 | 1140 | 79 | 0.07 | Ma-Me | 65 | 4.5 |
| z39-1 | 443 | 27 | 408 | 51 | n.s. | | n.d. | 0.07118 | 6.2 | 0.494 | 15.2 | 897 | 44 | 0.05 | Ma-Me | 57 | 2.6 |
| z39-2 | 446 | 25 | 410 | 32 | n.s. | | n.d. | 0.07159 | 5.8 | 0.4968 | 9.6 | 876 | 32 | 0.04 | Ma-Me | 54 | 0.2 |
| z38 | 452 | 36 | 548 | 128 | 970 | 580 | C | 0.07258 | 8.2 | 0.715 | 30.2 | 560 | 56 | 0.1 | Ma-Me | 40 | 14.3 |
| z30-1 | 474 | 28 | 450 | 79 | n.s. | | n.d. | 0.07633 | 6 | 0.5579 | 21.6 | 982 | 55 | 0.06 | Ma-Me | 69 | 6.9 |
| z51 | 498 | 28 | 529 | 45 | 667 | 200 | n.d. | 0.08023 | 5.8 | 0.6835 | 11 | 1851 | 142 | 0.08 | Ma-Me | 132 | 3.7 |
| z26 | 500 | 32 | 440 | 131.1 | n.s. | | n.d. | 0.08059 | 6.6 | 0.5429 | 36.6 | 1122 | 187 | 0.17 | Ma | 90 | 14.1 |
| z42 | 535 | 30 | 642 | 114 | 1038 | 460 | n.d. | 0.08655 | 5.8 | 0.8815 | 23.8 | 733 | 224 | 0.32 | Ma | 55 | 5.8 |
| z33 | 1463 | 83 | 2006 | 59 | 2624 | 40 | n.d. | 0.25476 | 6.4 | 6.2121 | 6.8 | 635 | 122 | 0.2 | Ma | 140 | 1.2 |

**Table 2:** Migmatitic gneiss L89 zircon SHRIMP II data. Results are presented by increasing $^{206}Pb/^{238}U$ ages. CL domains (within brackets when unclear): C, core; R, Rim; O oscillatory; n.d. not defined. Type, type of event on which the analyzed domain will provide an age constrain, Ma, magmatic; Me, Metamorphic. Th, and U concentration calculated following Stern [1997]. n.s., not significant. * represent the radiogenic component.

| Spot name | Age (Ma) 208/232 | ± (2σ) | 208/232 | ± % | Th (%) | U (ppm) | Th/U | 208Pb* (ppm) | % com 208Pb | Structural location |
|---|---|---|---|---|---|---|---|---|---|---|
| m29-2 | 13.1 | 5.1 | 0.000650 | 39,0 | 10.2 | 1395 | 72.9 | 32 | 7.3 | Ic Bt |
| m38-2 | 14.9 | 3.6 | 0.000736 | 24.4 | 7.3 | 3071 | 23.8 | 10 | 22.8 | Ic Bt |
| m2 | 15.3 | 4.2 | 0.000759 | 27.6 | 4.9 | 6942 | 7.0 | 21 | 29.5 | It |
| m24 | 16.5 | 3.6 | 0.000818 | 22,0 | 5.9 | 7859 | 7.5 | 30 | 26.7 | It |
| m32 | 16.7 | 7.2 | 0.000828 | 43.4 | 4.7 | 5010 | 9.4 | 10 | 58.8 | It |
| m38-1 | 17.8 | 2.7 | 0.000882 | 15,0 | 4.7 | 2307 | 20.5 | 28 | 7.7 | Ic Bt |
| m18 | 17.9 | 3.7 | 0.000888 | 20.6 | 5 | 3128 | 16.1 | 23 | 21.1 | Ic Chl |
| m33-1 | 19.3 | 2.2 | 0.000956 | 11.4 | 5.9 | 4569 | 13.0 | 45 | 4.9 | It |
| m29-1 | 19.4 | 4.8 | 0.000959 | 24.8 | 9.3 | 957 | 97.1 | 26 | 10.8 | Ic Bt |
| m33-2 | 21.8 | 2.6 | 0.001081 | 11.8 | 7.2 | 8687 | 8.3 | 59 | 11.4 | It |
| m25 | 23.1 | 6.9 | 0.001144 | 30,0 | 4.6 | 5713 | 8.1 | 21 | 51.1 | Ic Chl |
| m3-2 | 23.3 | 3.7 | 0.001152 | 16,0 | 6.7 | 5836 | 11.5 | 46 | 18.2 | Ic Bt |
| m3-1 | 25.4 | 3.6 | 0.001255 | 14.4 | 5.7 | 3638 | 15.6 | 52 | 8.0 | Ic Bt |
| m1-2 | 152 | 14 | 0.007545 | 9.4 | 6.5 | 3835 | 17.0 | 319 | 10.0 | Ic Bt |
| m1-1 | 248 | 11 | 0.012370 | 4.4 | 4.8 | 5846 | 8.2 | 478 | 6.4 | Ic Bt |

**Table 3:** Migmatitic gneiss L89 monazite SHRIMP II data. Results are presented by ascending $^{206}Pb/^{238}U$ ages. Structural location refer to the shape and position of the monazite crystal with respect to the surrounding minerals (Figure 10): It, interstitial; Ic, included, and the following abbreviation indicates the mineral in which the monazite is included. Bt., biotite; fs., Feldspar; Chl, Chlorite. Th and U concentrations are calculated following Stern and Stanborn [1998]. * represent the radiogenic component.

| Spot name | Age (Ma) 206/238 | ± (2σ) | Age (Ma) 207/235 | ± (2σ) | Age (Ma) 207/206 | ± (2σ) | CL domain | 206/238 | ± % | 207/235 | ± % | U (ppm) | Th (ppm) | Th/U | Type | $^{206}$Pb* (ppm) | % com Pb |
|---|---|---|---|---|---|---|---|---|---|---|---|---|---|---|---|---|---|
| z244-2 | 13,0 | 0.8 | 11.7 | 2,0 | n.s. | | R | 0.00202 | 5.8 | 0.0116 | 10.4 | 6795 | 15 | <0.01 | Hy | 12 | 0.3 |
| z240 | 14.3 | 0.8 | 13.6 | 1.1 | n.s. | | R | 0.00222 | 5.7 | 0.0135 | 7.4 | 18440 | 335 | 0.02 | Hy | 35 | 0.4 |
| z210-2 | 14.9 | 1,0 | 15,0 | 2.5 | n.s. | | (OR) | 0.00231 | 6.6 | 0.0149 | 16.6 | 7392 | 17 | <0.01 | Hy | 15 | 1.4 |
| z227-3 | 16.7 | 1.1 | 14.9 | 3.1 | n.s. | | (OR) | 0.00259 | 6.7 | 0.0148 | 21.2 | 8724 | 67 | 0.01 | Hy | 20 | 0.8 |
| z219-1 | 17.2 | 1.1 | 17,0 | 1.3 | n.s. | | R | 0.00267 | 6.4 | 0.0169 | 7.8 | 19795 | 160 | 0.01 | Hy | 45 | 0.3 |
| z220-1 | 18.3 | 1.3 | 18.5 | 3.5 | n.s. | | OR | 0.00284 | 7.2 | 0.0184 | 19.3 | 5787 | 307 | 0.05 | Hy | 14 | 1.4 |
| z225-3 | 18.9 | 1.3 | 20.8 | 2.4 | n.s. | | R | 0.00293 | 6.8 | 0.0207 | 11.9 | 13827 | 51 | <0.01 | Hy | 35 | 0.7 |
| z239-2 | 20,0 | 1.3 | 20.9 | 1.9 | n.s. | | R | 0.00311 | 6.6 | 0.0208 | 9.4 | 9725 | 33 | <0.01 | Hy | 26 | 1,0 |
| z244-1 | 21.7 | 1.4 | 13.1 | 6.4 | n.s. | | C | 0.00337 | 6.2 | 0.013 | 20.6 | 1379 | 119 | 0.09 | Me | 4 | 1.9 |
| z236-2 | 22.2 | 1.4 | 22.5 | 1.8 | n.s. | | R | 0.00345 | 6.5 | 0.0224 | 8.1 | 16522 | 113 | 0.01 | Hy | 49 | 0.4 |
| z227-2 | 25.2 | 1.7 | 25.4 | 2.7 | n.s. | | (OR) | 0.00392 | 6.7 | 0.0254 | 10.8 | 16711 | 159 | 0.01 | Hy | 57 | 0.7 |
| z220-2 | 170 | 14 | 180 | 27 | 315 | 320 | C | 0.02673 | 8.1 | 0.1942 | 16.5 | 555 | 99 | 0.18 | Ma | 13 | - |
| z225-1 | 256 | 21 | 624 | 42 | 2368 | 53 | C | 0.04049 | 8.4 | 0.8485 | 9,0 | 2000 | 155 | 0.08 | Ma | 70 | 9.8 |
| z238-1 | 343 | 19 | 350 | 19 | 437 | 56 | OR | 0.05463 | 2.9 | 0.4121 | 3.3 | 1042 | 240 | 0.24 | Ma | 49 | 2.1 |
| z231-1 | 474 | 27 | 480 | 31 | 554 | 120 | C | 0.07637 | 5.8 | 0.6048 | 8.2 | 679 | 188 | 0.29 | Ma | 45 | 0.3 |
| z210-1 | 622 | 49 | 1417 | 69 | 2962 | 54 | C | 0.10135 | 8.3 | 3.0387 | 9,0 | 478 | 86 | 0.19 | Ma | 42 | 12.6 |
| z227-1 | 891 | 54 | 917 | 43 | 981 | 60 | C | 0.14816 | 6.5 | 1.4672 | 7.2 | 949 | 311 | 0.34 | Ma | 121 | 0.2 |
| z219-2 | 1018 | 61 | 1240 | 49 | 1650 | 42 | C | 0.17101 | 6.5 | 2.3915 | 6.8 | 767 | 421 | 0.57 | Ma | 113 | 3.6 |
| z239-1 | 1542 | 88 | 1642 | 55 | 1773 | 36 | C | 0.27021 | 6.4 | 4.0398 | 6.7 | 712 | 203 | 0.29 | Ma | 166 | 1.8 |
| z216-1 | 1805 | 90 | 2066 | 51 | 2342 | 18 | OC | 0.32286 | 5.7 | 6.6488 | 5.8 | 541 | 219 | 0.42 | Ma | 150 | 1.2 |
| z236-1 | 2271 | 130 | 2350 | 69 | 2419 | 54 | C | 0.42231 | 6.8 | 9.1145 | 7.5 | 101 | 214 | 2.19 | Ma | 37 | 2.9 |

**Table 4:** Sample C43 leucocratic orthogneiss zircons SHRIMP II data. Similar caption as Table 2.

| # | Fraction (µm) | Wt. (mg) | U (ppm) | Pb* (ppm) | 206Pb/204Pb | 208Pb/206Pb | 206Pb/238U | 207Pb/235U | 207Pb/206Pb | 206Pb/238U | 207Pb/235U | 207Pb/206Pb | correl. coeff. |
|---|---|---|---|---|---|---|---|---|---|---|---|---|---|
| | | | | | | *atomic* | *ratios* | | | | *apparent ages* | | |
| **C32 leucocratic dyke** | | | | | | | | | | | | | |
| z1 | <100 [24] need.cl.un. | 0.055 | 5 224 | 16.4 | 2542 | 0.0722 | 0.00353 ± 1 | 0.0227 ± 1 | 0.0502 ± 3 | 22.7 | 22.8 | 204 | 0.59 |
| z2 | <100 [19] need.cl.un. | 0.034 | 4 031 | 23.5 | 2945 | 0.0819 | 0.00602 ± 2 | 0.0441 ± 3 | 0.0531 ± 3 | 38.7 | 43.8 | 331 | 0.62 |
| z3 | >100 [8] sp.pi.un. | 0.112 | 1 688 | 12.1 | 3318 | 0.0936 | 0.00726 ± 2 | 0.0583 ± 3 | 0.0582 ± 2 | 46.6 | 57.5 | 538 | 0.67 |
| z4 | >100 [8] sp.pi.ab. | 0.032 | 4 577 | 40.3 | 699 | 0.144 | 0.00822 ± 2 | 0.0692 ± 5 | 0.0610 ± 4 | 52.8 | 67.9 | 640 | 0.49 |
| z5 | >100 [13] sp.pi.ab. | 0.032 | 3 593 | 32.9 | 4346 | 0.1015 | 0.00942 ± 2 | 0.0840 ± 3 | 0.0647 ± 2 | 60.4 | 81.9 | 763 | 0.68 |
| m1 | <100 [8] ye.an. | 0.038 | 10 531 | 93.2 | 489 | 2.6295 | 0.00245 ± 3 | 0.0156 ± 2 | - | 15.7 | 15.7 | - | 0.91 |
| m2 | <100 [5] ye.an. | 0.028 | 7 475 | 84.2 | 449 | 3.6697 | 0.00246 ± 1 | 0.0158 ± 1 | - | 15.9 | 15.9 | - | 0.78 |
| **C43 leucocratic orthogneiss** | | | | | | | | | | | | | |
| m1 | < 100 [4] ye.an. | 0.025 | 15 106 | 78.6 | 785 | 1.2583 | 0.00222 ± 1 | 0.0142 ± 1 | - | 14.3 | 14.3 | - | 0.77 |
| m2 | <100 [5] ye.an. | 0.029 | 19 557 | 86.2 | 993 | 0.9096 | 0.00220 ± 1 | 0.0141 ± 1 | - | 14.2 | 14.2 | - | 0.85 |

**Table 5:** C32 (= K1C32 of *Lacassin et al*. [2004a]) and C43 ID-TIMS U–Pb isotope data for monazite (m) and zircon (z). [ ] number of grains of the analyzed fraction. ab. = air abraded, an. = anhedral, cl. = colourless, lp. = long prismatic, need. = needle shaped (acicular), pi. = pink, sp. = short prismatic , un. = unabraded, ye. = Yellow. The ± numbers represent the errors made on the last digit.

| Spot name | Age (Ma) 206/238 | ± (2σ) | Age (Ma) 207/235 | ± (2σ) | Age (Ma) 207/206 | ± (2σ) | CL domain | 206/238 | ± % | 207/235 | ± % | U (ppm) | Th (ppm) | Th/U | Type | $^{206}$Pb* (ppm) | % com Pb |
|---|---|---|---|---|---|---|---|---|---|---|---|---|---|---|---|---|---|
| z147-2 | 18.2 | 1.2 | 20.6 | 3,0 | n.s. | | OR | 0.00283 | 6.7 | 0.0205 | 11.4 | 1362 | 86 | 0.07 | Hy | 3 | 0.9 |
| z120-2 | 20,0 | 1.2 | 21.2 | 2.7 | n.s. | | OR | 0.00311 | 6,0 | 0.0211 | 10.2 | 2542 | 15 | 0.01 | Hy | 7 | 0.6 |
| z120-1 | 20.9 | 2.2 | - | - | n.s. | | ReC | 0.00324 | 9.3 | - | - | 230 | 2 | 0.01 | Me | 1 | 1.4 |
| z147-3 | 23.8 | 1.5 | 22.3 | 6.7 | n.s. | | OR | 0.00369 | 6.1 | 0.0222 | 11.7 | 2057 | 121 | 0.06 | Hy | 7 | 1.1 |
| z156-2 | 26.2 | 1.7 | 26.1 | 4.3 | n.s. | | (O)R | 0.00407 | 6.4 | 0.026 | 10.7 | 2479 | 106 | 0.04 | Hy | 9 | 1.5 |
| z122-2 | 26.9 | 1.6 | 22.9 | 4.4 | n.s. | | (O)R | 0.00419 | 6,0 | 0.0228 | 9.6 | 1776 | 54 | 0.03 | Hy | 6 | 0.2 |
| z147-1 | 270 | 16 | 296 | 22.7 | 611 | 91 | C | 0.04277 | 5.9 | 0.3387 | 7.3 | 509 | 64 | 0.13 | Ma | 19 | 0.9 |
| z156-1 | 287 | 18 | 310 | 48 | 774 | 210 | C | 0.0456 | 6.2 | 0.3565 | 12,0 | 171 | 143 | 0.86 | Ma | 7 | 6.1 |
| z145-3 | 317 | 21 | 414 | 180 | 1047 | 1000 | OR | 0.05032 | 6.8 | 0.5033 | 50.9 | 879 | 85 | 0.1 | Ma | 42 | 10.2 |
| z145-1 | 331 | 31 | 352 | 32.2 | 546 | 110 | OR | 0.05271 | 9.6 | 0.4146 | 10.8 | 1063 | 106 | 0.1 | Ma | 48 | 0,0 |
| z153-1 | 336 | 20 | 332 | 55.5 | | | C | 0.05357 | 5.9 | 0.3864 | 16.7 | 446 | 196 | 0.45 | Ma | 21 | 3,0 |
| z122-1 | 477 | 27 | 692 | 38 | 1509 | 89 | C | 0.07681 | 5.8 | 0.977 | 7.5 | 335 | 87 | 0.27 | Ma | 22 | 5.4 |
| z125-1 | 546 | 33 | 701 | 46.2 | 1325 | 87 | ReC | 0.08843 | 6.3 | 0.9941 | 7.8 | 1280 | 187 | 0.15 | Ma | 98 | 1.7 |
| z122-3 | 573 | 32 | 876 | 45 | 1777 | 86 | C | 0.09295 | 5.9 | 1.3688 | 7.6 | 270 | 85 | 0.33 | Ma | 22 | 6.9 |
| z144-1 | 700 | 39 | 802 | 36.5 | 1138 | 55 | C | 0.11461 | 5.9 | 1.203 | 6.6 | 641 | 120 | 0.19 | Ma | 63 | 0.6 |
| z145-2 | 764 | 43 | 799 | 40.8 | 942 | 85 | OC | 0.12584 | 6,0 | 1.1972 | 7.3 | 496 | 165 | 0.34 | Ma | 54 | 1.9 |
| z124-1 | 1105 | 59 | 1229 | 45.9 | 1485 | 50 | C | 0.18703 | 5.8 | 2.3562 | 6.4 | 254 | 106 | 0.43 | Ma | 41 | 0.9 |

**Table 6:** Leucocratic orthogneiss P34 zircon SHRIMP II data. Same caption as Table 2. Re, re-crystallized.

| Spot name | Age (Ma) 206/238 | ± (2σ) | Age (Ma) 207/235 | ± (2σ) | Age (Ma) 207/206 | ± (2σ) | CL domain | 206/238 | ± % | 207/235 | ± % | U (ppm) | Th (ppm) | Th/U | Type | $^{206}Pb^*$ (ppm) | % com Pb |
|---|---|---|---|---|---|---|---|---|---|---|---|---|---|---|---|---|---|
| z1-1 | 19.8 | 1.4 | 23 | 3,0 | n.s. | | OR | 0.00307 | 7,0 | 0.0229 | 13.2 | 2715 | 27 | 0.01 | Ma-Me | 7 | 1.2 |
| z3-2 | 20.3 | 1.7 | 30.5 | 8.3 | n.s. | | OR | 0.00315 | 8.4 | 0.0305 | 27.6 | 2198 | 204 | 0.1 | Ma | 6 | 2.1 |
| z34-2 | 21.1 | 1.4 | 25.8 | 6.3 | n.s. | | OR | 0.00327 | 6.7 | 0.0258 | 24.5 | 3292 | 1305 | 0.41 | Ma | 9 | 2.9 |
| z53-2 | 21.6 | 1.5 | 23.1 | 7.6 | n.s. | | R | 0.00336 | 7,0 | 0.0231 | 33.4 | 2733 | 407 | 0.15 | Ma | 8 | 4.5 |
| z3-3 | 22.2 | 1.5 | 25.2 | 2.8 | n.s. | | OR | 0.00346 | 6.7 | 0.0251 | 11.3 | 4883 | 240 | 0.05 | Ma-Me | 15 | 1.4 |
| z25-2 | 22.8 | 1.6 | 30.6 | 4,0 | n.s. | | OR | 0.00354 | 7.1 | 0.0306 | 13.2 | 3139 | 510 | 0.17 | Ma | 10 | 2.6 |
| z41-3 | 23.3 | 1.8 | 25.7 | 15.3 | n.s. | | OR | 0.00362 | 7.9 | 0.0256 | 60.2 | 2522 | 376 | 0.15 | Ma | 8.2 | 3.9 |
| z30-2 | 24.4 | 1.8 | 28.4 | 13,0 | n.s. | | R | 0.00379 | 7.3 | 0.0283 | 46.4 | 3722 | 503 | 0.14 | Ma | 12 | 3.1 |
| z34-3 | 25.2 | 1.9 | 28.1 | 9.4 | n.s. | | OR | 0.00391 | 7.5 | 0.0281 | 33.8 | 4762 | 853 | 0.19 | Ma | 16 | 3,0 |
| z1-4 | 26.8 | 1.8 | 25.5 | 2.9 | n.s. | | OR | 0.00416 | 6.6 | 0.0255 | 11.4 | 3171 | 49 | 0.02 | Ma-Me | 11 | 0.8 |
| z8-2 | 27.3 | 2,0 | 27.1 | 11.5 | n.s. | | OR | 0.00424 | 7.3 | 0.0271 | 42.9 | 1525 | 282 | 0.19 | Ma | 6 | 3 |
| z53-3 | 27.4 | 1.9 | 26.3 | 7.1 | n.s. | | (O)R | 0.00426 | 6.9 | 0.0263 | 27.4 | 5617 | 742 | 0.14 | Ma | 21 | 2.4 |
| z41-1 | 32,7 | 2,3 | 31.9 | 8.2 | n.s. | | OC | 0.00508 | 7.1 | 0.0319 | 26.1 | 2237 | 3026 | 1.4 | Ma | 10 | 2.7 |
| z41-2 | 34,8 | 2,2 | 38.8 | 3,0 | n.s. | | OC | 0.00541 | 6.5 | 0.0389 | 7.9 | 5857 | 1174 | 0.21 | Ma | 27 | 0.2 |
| z8-1 | 35,9 | 2,5 | 38.6 | 11.9 | n.s. | | OC | 0.00559 | 6.9 | 0.0388 | 31.3 | 2349 | 611 | 0.27 | Ma | 12 | 2.4 |
| z18-2 | 44.8 | 3,0 | 56.8 | 15.7 | n.s. | | C-R | 0.00697 | 6.8 | 0.0575 | 28.5 | 1807 | 164 | 0.09 | Ma-Me | 11 | 2.9 |
| z34-1 | 181 | 13 | 198 | 75 | 415 | 900 | C | 0.0284 | 7,0 | 0.2156 | 41.6 | 381 | 98 | 0.27 | Ma | 10 | 3.5 |
| z53-1 | 294 | 19 | 302 | 56 | 367 | 450 | C | 0.04658 | 6.7 | 0.3462 | 21.4 | 321 | 136 | 0.44 | Ma | 13 | 1.9 |
| z1-5 | 325 | 29 | 416 | 72 | 958 | 380 | OC | 0.05171 | 9,0 | 0.5064 | 21,0 | 210 | 114 | 0.56 | Ma | 9.4 | - |
| z18-1 | 396 | 25 | 425 | 44 | 590 | 230 | C | 0.06328 | 6.6 | 0.5202 | 12.5 | 551 | 299 | 0.56 | Ma | 30 | 1.8 |
| z25-1 | 438 | 27 | 484 | 29 | 709 | 79 | C | 0.07024 | 6.4 | 0.6103 | 7.5 | 869 | 310 | 0.37 | Ma | 53 | 0.9 |
| z30-1 | 442 | 28 | 461 | 38 | 555 | 170 | C | 0.07104 | 6.6 | 0.5746 | 10.2 | 365 | 179 | 0.51 | Ma | 22 | 1.3 |
| z3-1 | 736 | 48 | 800 | 57 | 984 | 150 | C | 0.12095 | 6.9 | 1.1997 | 10.3 | 198 | 143 | 0.75 | Ma | 21 | 1.6 |
| z48-1 | 1771 | 106 | 1802 | 104 | 1837 | 180 | C | 0.31625 | 6.9 | 4.8964 | 12.3 | 159 | 106 | 0.69 | Ma | 43 | 1.8 |

**Table 7:** Sheared two-mica orthogneiss P18 zircons SHRIMP II data. Same caption as Table 2.

| Spot name | Age (Ma) 208/232 | ± (2σ) | 208/232 | ± % | Th (Wt%) | U (ppm) | Th/U Wt | 208Pb* (ppm) | % com 208Pb | Structural location |
|---|---|---|---|---|---|---|---|---|---|---|
| m15 | 13.5 | 1.7 | 0.000666 | 12.7 | 7.8 | 2026 | 31 | 52 | 1.3 | It |
| m16-b | 16.8 | 2.1 | 0.000826 | 12.6 | 4.6 | 545 | 18 | 38 | 24.5 | It |
| m4 | 16.9 | 2.1 | 0.000835 | 12.7 | 7.1 | 5214 | 14 | 59 | 4.8 | It |
| m6-b | 17.4 | 2.2 | 0.000859 | 12.7 | 8.5 | 2021 | 18 | 73 | 0.7 | It |
| m12 | 17.7 | 2.2 | 0.000876 | 12.6 | 2.1 | 531 | 65 | 18 | 3.9 | It |
| m22 | 18.1 | 2.4 | 0.000894 | 13.1 | 8.8 | 2648 | 21 | 79 | 2.4 | It |
| m16-a | 18.3 | 2.3 | 0.000906 | 12.7 | 7.4 | 1844 | 44 | 67 | 1.3 | It |
| m7 | 18.3 | 2.3 | 0.000908 | 12.7 | 10.2 | 1640 | 29 | 92 | 0.3 | It |
| m19 | 18.5 | 2.3 | 0.000917 | 12.6 | 5.1 | 977 | 51 | 47 | 0.6 | It |
| m9 | 19.3 | 2.7 | 0.000939 | 14.2 | 6.2 | 586 | 62 | 58 | 56.9 | It |
| m6-a | 19.5 | 2.5 | 0.000964 | 12.9 | 8.5 | 2021 | 26 | 82 | 0.7 | It |
| m10 | 19.9 | 2.6 | 0.000986 | 12.9 | 8.9 | 2439 | 26 | 87 | 3.1 | It |
| m5 | 23,0 | 3.7 | 0.001137 | 16.2 | 8 | 1889 | 33 | 91 | 0.1 | It |
| m3-b | 23.2 | 3,0 | 0.001148 | 12.8 | 8.4 | 2562 | 24 | 97 | 1.1 | It |
| m3-a | 23.7 | 3,0 | 0.001174 | 12.6 | 7.4 | 1939 | 16 | 87 | 0.1 | It |
| m11-a | 24.1 | 3.1 | 0.001193 | 13,0 | 8.1 | 5428 | 17 | 97 | 0.1 | Ic Bt |
| m8 | 24.2 | 3.1 | 0.001196 | 12.6 | 7.2 | 1631 | 30 | 86 | 2.4 | Ic Fs |
| m14 | 25.5 | 3.5 | 0.001263 | 13.5 | 8.6 | 5024 | 24 | 108 | 0.2 | Ic Fs |
| m2 | 27.9 | 3.6 | 0.001383 | 12.8 | 9.3 | 1040 | 60 | 128 | 0.1 | Ic Bt |

**Table 8:** two-micas orthogneiss P18 Monazite SHRIMP II data. Same caption as Table 2.

| Spot name | Age (Ma) 206/238 | ± (2σ) | Age (Ma) 207/235 | ± (2σ) | Age (Ma) 207/206 | CL domain | 206/238 | ± % | 207/235 | ± % | U (ppm) | Th (ppm) | Th/U | | $^{206}$Pb* (ppm) | % com Pb |
|---|---|---|---|---|---|---|---|---|---|---|---|---|---|---|---|---|
| z23 | 19.9 | 1.6 | 24.6 | 6.1 | n.s. | n.d. | 0.00309 | 8.2 | 0.0245 | 25 | 3882 | 5514 | 1.42 | Ma | 10 | 5.5 |
| z24 | 20.1 | 1.2 | 20.9 | 1.5 | n.s. | n.d. | 0.00313 | 6.2 | 0.0208 | 7.4 | 2523 | 777 | 0.31 | Ma | 7 | 0.2 |
| z18 | 21.2 | 1.3 | 21.9 | 1.5 | n.s. | O | 0.0033 | 6.4 | 0.0218 | 7,0 | 1640 | 909 | 0.55 | Ma | 5 | 0.2 |
| z27-2 | 23.6 | 1.6 | 25,0 | 3.7 | n.s. | n.d. | 0.00367 | 6.8 | 0.0249 | 14.8 | 1014 | 258 | 0.25 | Ma | 3 | 1.8 |
| z27-1 | 23.9 | 6.9 | 22.6 | 49.1 | n.s. | n.d. | 0.00371 | 29.2 | 0.0225 | 219 | 1750 | 274 | 0.16 | Ma | 6 | 22.2 |

**Table 9:** biotite-rich gneiss P20 zircon Cameca IMS 1270 data. Similar caption as Table 2.

| n° | Fraction (µm) | Wt. (mg) | U (ppm) | Pb rad (ppm) | 206Pb / 204Pb | 208Pb / 206Pb | 206Pb / 238U | 207Pb / 235U | 207Pb / 206Pb | 206Pb / 238U | 207Pb / 235U | 207Pb / 206Pb | correl. coeff. |
|---|---|---|---|---|---|---|---|---|---|---|---|---|---|
| | | | | | | *atomic* | *ratios* | | | | *apparent ages* | | |
| 1 | >100 [21] need.cl.un. | 0.192 | 691 | 2.42 | 434 | 0.1663 | 0.00328 ± 3 | 0.0213 ± 5 | 0.0471 ± 9 | 21.1 | 21.4 | 53 | 0.52 |
| 2 | >150 [5] lp.pi.un. | 0.23 | 598 | 3.35 | 809 | 0.1558 | 0.00518 ± 1 | 0.0451 ± 1 | 0.0632 ± 1 | 33.3 | 44.8 | 713 | 0.83 |
| 3 | >150 [4] lp.pi.un. | 0.107 | 1 238 | 12.2 | 1957 | 0.0896 | 0.00994 ± 2 | 0.0727 ± 2 | 0.0530 ± 1 | 63.8 | 71.2 | 329 | 0.82 |
| 4 | >150 [7] sp.ye.un. | 0.241 | 833 | 10.9 | 2023 | 0.0968 | 0.01306 ± 5 | 0.0998 ± 4 | 0.0554 ± 1 | 83.6 | 96.6 | 430 | 0.88 |
| 5 | >150 [8] sp.ye.un. | 0.246 | 811 | 11.2 | 1682 | 0.1105 | 0.01359 ± 4 | 0.1034 ± 3 | 0.0552 ± 1 | 87,0 | 99.9 | 421 | 0.86 |
| 6 | >150 [6] sp.ye.ab. | 0.178 | 614 | 14.5 | 1461 | 0.0929 | 0.02362 ± 7 | 0.1826 ± 8 | 0.0561 ± 1 | 150.5 | 170 | 456 | 0.76 |

**Table 10:** K2P30 ID-TIMS U–Pb isotope data for zircon. Same caption as Table 5.

| Transect | 1 | 1 | 2 | 3 | 3 | 3 | 3 | 3 | 4 | 4 | Labhar Kangri |
|---|---|---|---|---|---|---|---|---|---|---|---|
| Samples | Migmatitic gneiss **L89** | Migmatitic gneiss **L89** | Leucocratic orthogneiss **P34** | Two-mica orthogneiss **P18** | Two-mica orthogneiss **P18** | Biotite-rich gneiss **P20** | Leucocratic dyke **C32** | Leucocratic dyke **C32** | Leucocratic orthogneiss **C43** | Leucocratic orthogneiss **C43** | Granite **K2P30** |
| Method | SHRIMP II | SHRIMP II | SHRIMP II | SHRIMP II | IMS-1270 | IMS-1270 | ID-TIMS | ID-TIMS | SHRIMP II | ID-TIMS | ID-TIMS |
| Mineral | Zircon | Monazite | Zircon | Zircon | Monazite | Zircon | Zircon | Monazite | Zircon | Monazite | Zircon |
| Inheritance | **~300 - 2620** [15] | **> 150** [2] | **~300 - 1800** [11] | **~180 - 1800** [8] | | | **~1300** [4] | | **~170 - 3000** [10] | | **~490 - 1450** [5] |
| Magmatic | **34.7** ± 2.4 [1] | | | **34.4** ± 1.3 [3] | | | **32.5** ± 2.6 [4] | | | | |
| Magmatic | **23.4** ± 4.0 [1] | **24.2** ± 2.4 (25.4 - 23.1 +3.6, -6.9) [3] | | **23.3** +4 -2.2 (27.4 - 19.8 +1.9, - 1.7) [9] | **25.2** ± 1.6 (27.9 - 24.1 +3.6, -3.1) [4] | **21.7** ± 3.6 (23.9 - 19.9 +6.9, -1.6) [5] | **22.7** ± 0.1 [1] | | | | **21.1** ± 0.3 [1] |
| Metamorphic or Hydrothermal | | **18.2** ± 1.8 (21.8 - 13.1 +2.6, -5.1) [10] | **22.1** ± 4.7 (26.9 - 18.2 +1.6, -1.2) [6] | | **18.8** ± 2.8 (23.7 - 13.5 +3.0, -1.7) [15] | | | **15.8** ± 0.2 [2] | **21.7** ± 1.4 [1] | **14.4** ± 0.7 [2] | |
| Metamorphic or Hydrothermal | | | | | | | | | **17.8** +4.4 -3.4 (25.2 - 13.1 +1.7, -0.8) [10] | | |

**Table 11:**Summary of ID-TIMS, SHRIMP II and Cameca IMS 1270 ages. Average ages in Ma of zircon/monazite grains populations are reported in bold with the corresponding 95% confidence level error (**xx.x**±x.x). Coresponding individual ages range of the population (xx.x – xx.x)with extremum 2 $\sigma$ errors (+x.x, -x.x) and number of individual ages [n] are also given. Magmatic and, metamorphic / Hydrothermal zircons are distinguished from their crystal shape, color, Th/U ratio, U content and BSE – CL patterns, see text for details.

onset age of right-lateral deformations along the KFZ

| ref Figure 17 | Age | location | type of age constrain (sample) | Reference | Inferences |
|---|---|---|---|---|---|
| [1] | between 15.9 and 13.7 Ma | Nubra plutonic unit E77°37'-E77°45' | bracketed by the age of deformed (P38) and little deformed (P37) dykes | Phillips et al., 2004 | All protolithes of orthogneiss are stricktly synkinematic |
| [2] | between 15.6 and 13.7 Ma | Pangong range Tangtse E78°10' | bracketed by the age of deformed (P11) and little deformed (P8) dykes | Phillips et al., 2004 | All protolithes of orthogneiss are stricktly synkinematic |
| [3] | ~17 Ma | Pangong range Tangtse E78°10' | Cooling history based on Ar data | Dunlap et al., 1998 | First phase of rapid cooling due to transpretional exhumation |
| [4] | prior to ~18 Ma | Pangong range Tangtse E78°10' | Age of the Tangtse migmatites and granite (O22 and 215, Searle et al. 1998) | Rolland et al., in press | Tangtse granite and migmatites are synkinematic |
| [5] | prior to ~32 Ma | Pangong range Tangtse E78°10' | Amphibole oldest Ar steps (L450) | Rolland et al., in press | Tangtse granulites are synkinematic |
| [6] | prior to ~23 Ma | North Ayilari (NA) sz E79°40' | Age of syntectonic dyke (2nd magmatic episode, C32) | Lacassin et al., 2004 this study | 2nd phase (~25-22 Ma) of magmatism is synkinematic |
| [7] | prior to ~21 Ma | North Ayilari (NA) sz E79°40' | Minimum age of ductile deformation from cooling history based on Ar data | Valli et al., 2007 | |
| [8] | prior to ~35 Ma | North Ayilari (NA) sz E79°40' | Age of 1st magmatic episode in the NA range (L89, P18, C32) | Lacassin et al., 2004 | All Tertiary magmatic episodes are synkinematic |
| [9] | After ~13Ma | Baer basin E80°30' | Age of the South Kailas thrust from Ar cooling history (Yin et al., 1999) | Murphy et al., 2000 | South Kailas thrust antecedent to the KFZ |

Magmatism

| ref Figure 17 | Age | location | | comment (sample) | Reference |
|---|---|---|---|---|---|
| [M1] | 20-18 Ma | W of Tash Gorgan | | | Arnaud, 1992<br>Xie et al., 1992 |
| [M2] | 25.5±0.3 Ma | baltoro batolith | ~E77° | 1st pulse of magmatism (K11) | Schärer et al., 1990 |
| [M3] | 21±0.5 Ma | baltoro batolith | ~E77° | 2nd pulse of magmatism (K10, H4, H8) | Parrish and Tirrul, 1989<br>Schärer et al., 1990 |
| [M4] | ~16-15 Ma | Nubra plutonic unit E77°37'-E77°45' | | samples P38 and 021 | Phillips et al., 2004<br>Weinberg et al., 2000 |
| [M5] | 18.5±1.5 Ma | Pangong range Tangtse E78°10' | | Tangtse granite (215) and migmatites (O22) | Searle et al., 1998 |
| [M6] | ~25-22 Ma | North Ayilari (NA) E79°40' | | 2nd magmatic episode (P18, P20, P34, C32, C43 and L89) | this study |
| [M7] | 21.1±0.3 Ma | Labhar-Kangri | | (K2P30) | this study |

**Table 12:** Published timing constraints ages of shearing onset and Miocene magmatism along the KFZ. Only the longitude along the fault is given for location. See Figure 17 and text sections 5.4 and 5.5.

| **Suture zone West of the Karakorum fault zone** | | | **Match East of the Karakorum fault** | | | **offset** | | **Finite fault rate** | | | |
|---|---|---|---|---|---|---|---|---|---|---|---|
| | | | | | | | | Oligo-Miocene KKF [C] | | Miocene KKF [A] | |
| name | Suturing age | reference | name | Suturing age | reference | amount (km) | reference | age (Ma) | rate (mm/yr.) | age (Ma) | rate (mm/yr.) |
| Tanymas | Triasic | Schwab et al., 2004 | Jinsha (a) | Triasic | Schwab et al., 2004 Yin and Harrison 2000 | 100-130 | Schwab et al., 2004 | 21 | 5 | 15 | *8* |
| | | | Jinsha (b) | Triasic | Matte et al., 1996 | **~435-565** | Valli, 2005 | 21 | **21-27** | 15 | ***29-38*** |
| Rushan - Pshart | Late Jurassic-Early Cretaceous | Pashkov and Shvol'man, 1979; Shvol'man, 1980; Montenat et al., 1986; Burtman and Molnar, 1993; Leven, 1995 | Jinsha (a) | Triasic | Schwab et al., 2004 Yin and Harrison 2000 | ~ 100 | Searle and Philips, 2007 | 22 | 5 | 15 | *7* |
| | | | Bangong | Early K (100-140 Ma) | Kapp et al. 2005 | ≥ 400 | Lacassin et al., 2004a | 23 | ≥17 | 15 | 27 |
| | | | Bangong | Early K (100-140 Ma) | Kapp et al. 2005 | **480** | This study | 23 | **21** | 15 | ***32*** |
| Shyok | late K (88-80 Ma) | Peterson and windley, 1985 Weinberg et al., 2000 | Bangong | Early K (100-140 Ma) | Kapp et al. 2005 | ~150 | Searle and Philips, 2007 | 25 | 6 | 14 | *11* |
| | | | Shiquanhe | Late K? | Matte et al., 1996 | 280 | Lacassin et al., 2004a (whole Karakorum def. zone) | 25 | 11 | 13 | 22 |
| | | | | | | **≥200** | This study | 25 | **≥8** | 13 | ***≥15*** |
| Indus | Tertiary | | Yarlung-Tzangpo | Tertiary | | ≤400 | Lacassin et al., 2004a (whole Karakorum def. zone) | 23 | 17 | 10 | 40 |
| | | | | | | **≥ 220** | This study | 23 | **≥10** | 10 | ***≥22*** |
| | | | | | | ~200 | Ratsbacher et al., 1994 | 23 | 9 | 10 | 20 |
| | | | | | | 66 | Murphy et al., 2000 | 23 | 3 | 10 | 7 |

**Table 13:** Estimates of suture zones offsets across the KFZ and corresponding finite fault rates. Preferred offsets are in bold. Some offsets of *Lacassin et al.* [2004] were measured for the whole ~80 km wide Karakorum deformation zone. In this study, corresponding offsets are measured from piercing points on the trace of the active fault. In any case, uncertainties on measured offsets are difficult to estimate but could reach a few tenths of kilometres. Rates are calculated using initiation ages [A] (italic) and [C] shown in Figure 17b. Preferred rates are bold. See text section 5.6 and Figure 18.

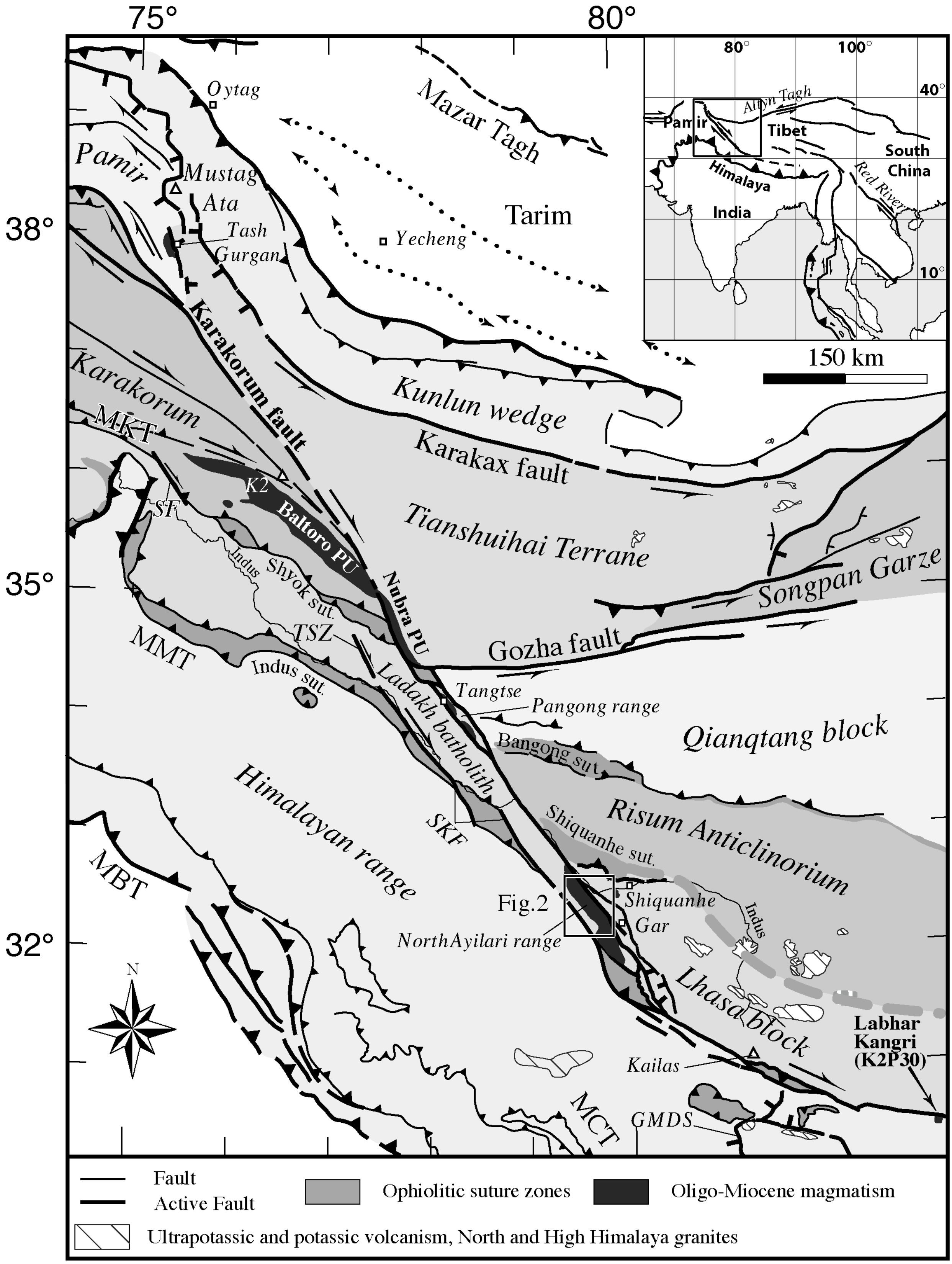
75°
80°
38°
35°
32°
80°
100°
40°
10°
Altyn Tagh
Pamir
Tibet
South
China
Himalaya
Red River
India
150 km
Oytag
Mazar Tagh
Pamir
Mustag
Ata
Tash
Gurgan
Yecheng
Tarim
Karakorum fault
Karakorum
MKT
Kunlun wedge
Karakax fault
K2
Baltoro PU
SF
Tianshuihai Terrane
Indus
Shyok sut.
Nubra PU
Songpan Garze
TSZ
MMT
Gozha fault
Indus sut.
Ladakh batholith
Tangtse
Pangong range
Qianqtang block
Bangong sut.
Himalayan range
SKF
Risum Anticlinorium
Shiquanhe sut.
MBT
Fig.2
Shiquanhe
Gar
Indus
NorthAyilari range
N
Lhasa block
Labhar
Kangri
(K2P30)
Kailas
MCT
GMDS
Fault
Active Fault
Ophiolitic suture zones
Oligo-Miocene magmatism
Ultrapotassic and potassic volcanism, North and High Himalaya granites

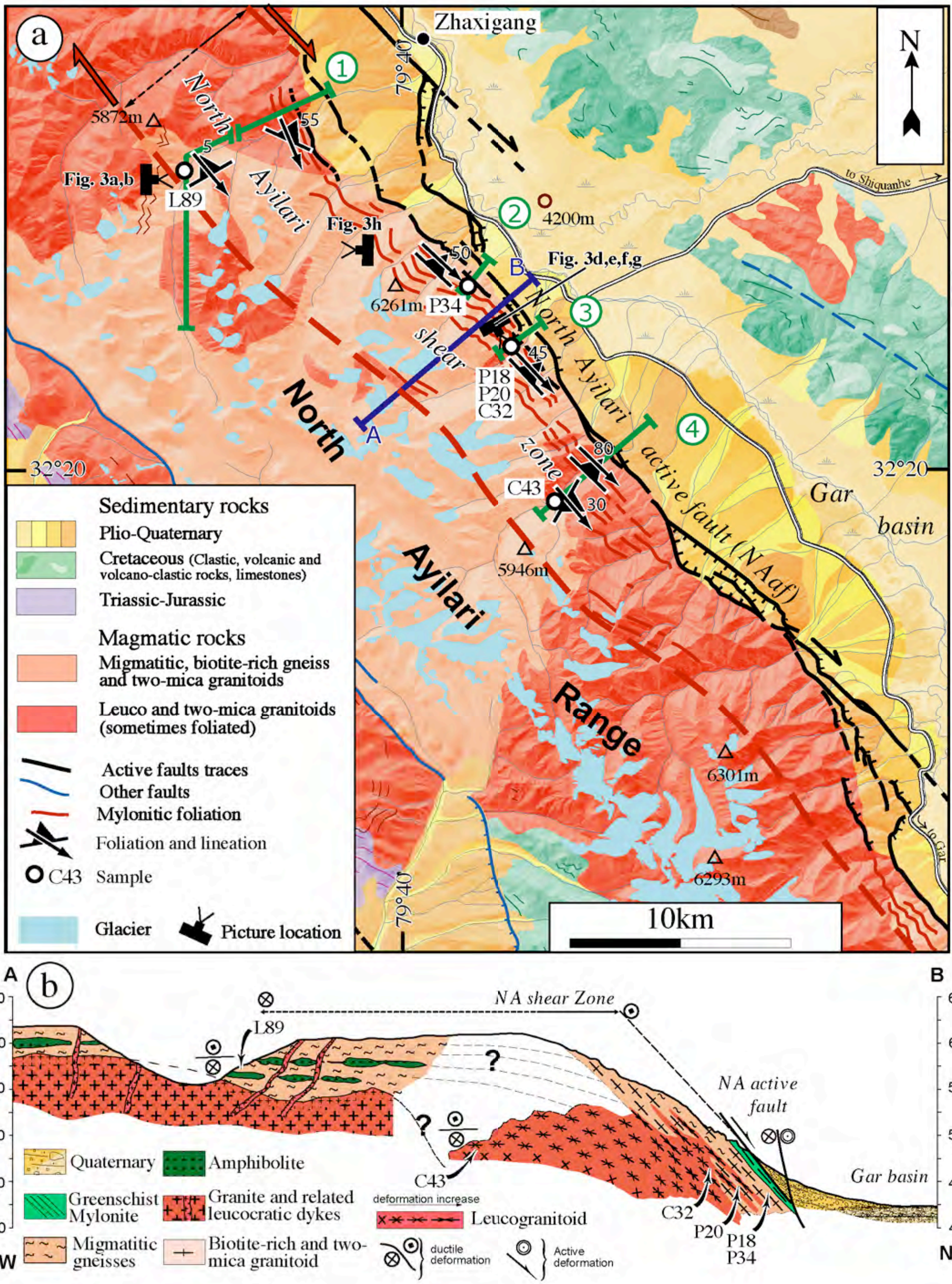
a
Zhaxigang
N
79°40
North
Ayilari
5872m
55
5
Fig. 3a,b
L89
Fig. 3h
4200m
50
Fig. 3d,e,f,g
6261m
P34
B
shear
North
Ayilari
45
P18
P20
C32
A
North
zone
80
active fault (NAaf)
C43
30
5946m
Ayilari
Range
6301m
6293m
32°20
Gar
basin
to Shiquanhe
to Gar
10km
Sedimentary rocks
Plio-Quaternary
Cretaceous (Clastic, volcanic and volcano-clastic rocks, limestones)
Triassic-Jurassic
Magmatic rocks
Migmatitic, biotite-rich gneiss and two-mica granitoids
Leuco and two-mica granitoids (sometimes foliated)
Active faults traces
Other faults
Mylonitic foliation
Foliation and lineation
C43 Sample
Glacier
Picture location
b
A
B
SW
NE
NA shear Zone
NA active fault
Gar basin
L89
C43
C32
P20
P18
P34
6500
6000
5500
5000
4500
4000
Quaternary
Amphibolite
Greenschist Mylonite
Granite and related leucocratic dykes
deformation increase
Leucogranitoid
Migmatitic gneisses
Biotite-rich and two-mica granitoid
ductile deformation
Active deformation

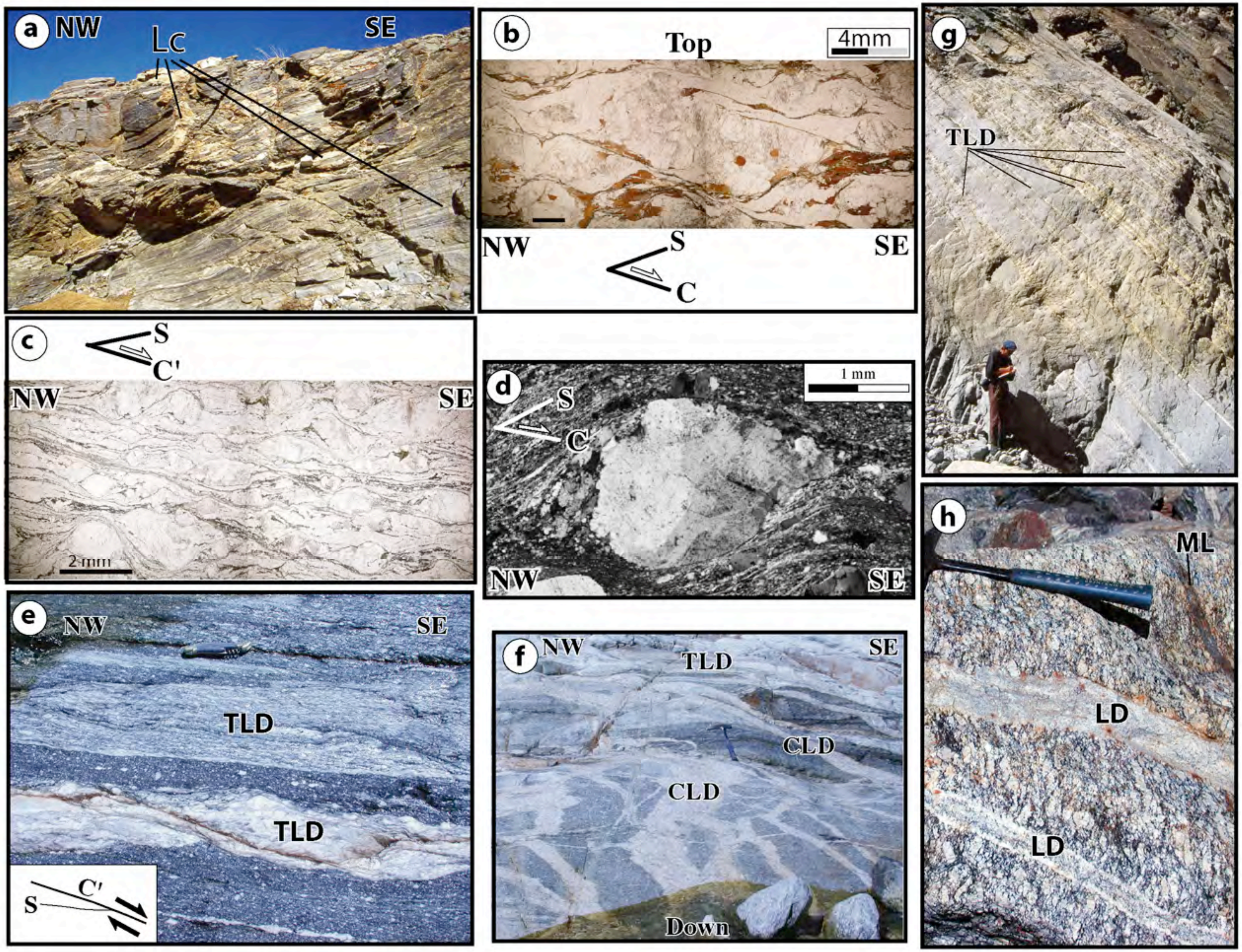

a
NW
Lc
SE
b
Top
4mm
NW
S
C
SE
c
S
C'
NW
SE
2 mm
d
1 mm
S
C
NW
SE
e
NW
SE
TLD
TLD
C'
S
f
NW
TLD
SE
CLD
CLD
Down
g
TLD
h
ML
LD
LD

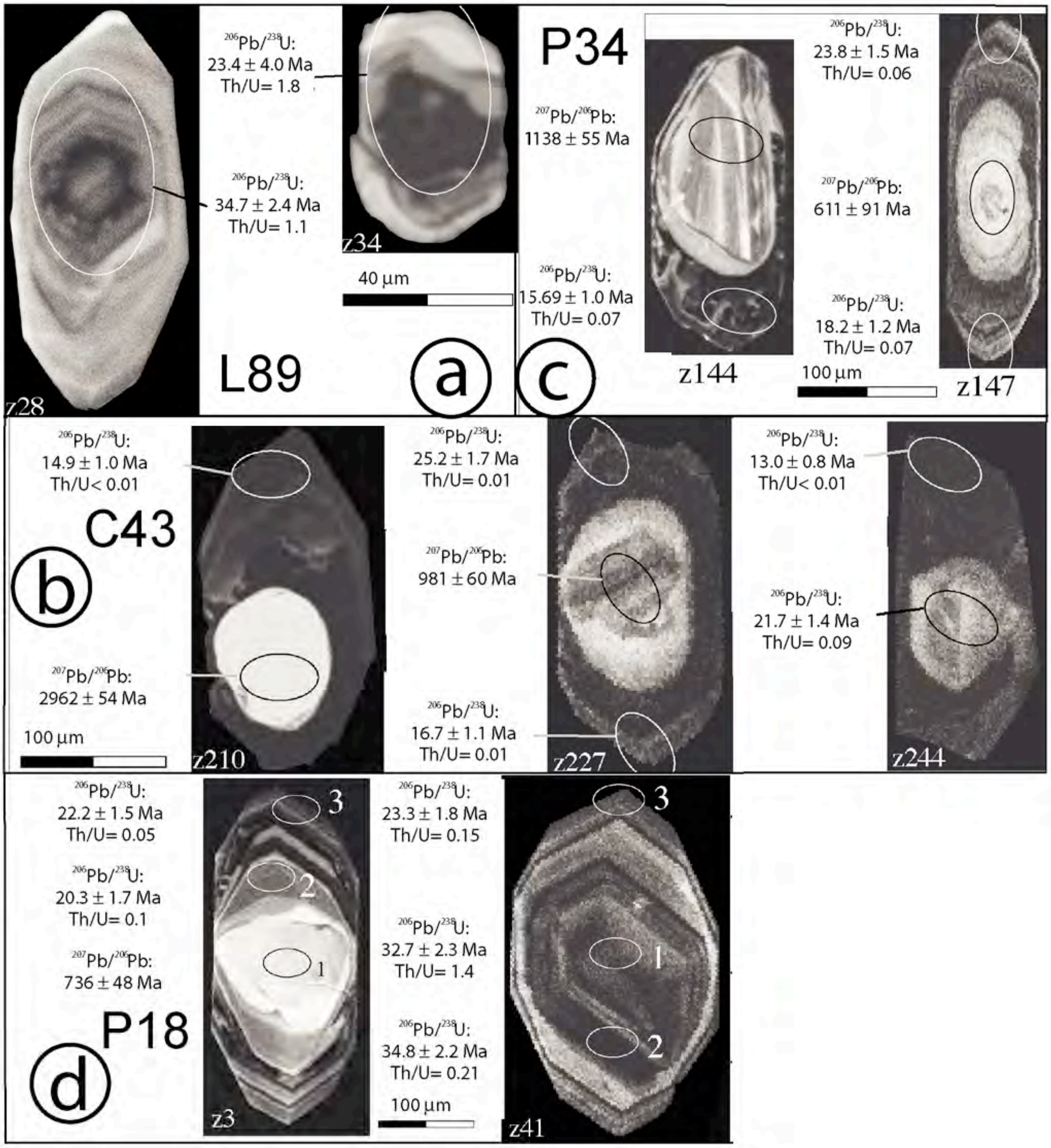

z28
$^{206}Pb/^{238}U$: 23.4 ± 4.0 Ma Th/U= 1.8
$^{206}Pb/^{238}U$: 34.7 ± 2.4 Ma Th/U= 1.1
z34
40 µm
L89
a
P34
$^{207}Pb/^{206}Pb$: 1138 ± 55 Ma
$^{206}Pb/^{238}U$: 15.69 ± 1.0 Ma Th/U= 0.07
c
z144
$^{206}Pb/^{238}U$: 23.8 ± 1.5 Ma Th/U= 0.06
$^{207}Pb/^{206}Pb$: 611 ± 91 Ma
$^{206}Pb/^{238}U$: 18.2 ± 1.2 Ma Th/U= 0.07
100 µm
z147
$^{206}Pb/^{238}U$: 14.9 ± 1.0 Ma Th/U< 0.01
C43
b
$^{207}Pb/^{206}Pb$: 2962 ± 54 Ma
100 µm
z210
$^{206}Pb/^{238}U$: 25.2 ± 1.7 Ma Th/U= 0.01
$^{207}Pb/^{206}Pb$: 981 ± 60 Ma
$^{206}Pb/^{238}U$: 16.7 ± 1.1 Ma Th/U= 0.01
z227
$^{206}Pb/^{238}U$: 13.0 ± 0.8 Ma Th/U< 0.01
$^{206}Pb/^{238}U$: 21.7 ± 1.4 Ma Th/U= 0.09
z244
$^{206}Pb/^{238}U$: 22.2 ± 1.5 Ma Th/U= 0.05
$^{206}Pb/^{238}U$: 20.3 ± 1.7 Ma Th/U= 0.1
$^{207}Pb/^{206}Pb$: 736 ± 48 Ma
P18
d
z3
$^{206}Pb/^{238}U$: 23.3 ± 1.8 Ma Th/U= 0.15
$^{206}Pb/^{238}U$: 32.7 ± 2.3 Ma Th/U= 1.4
$^{206}Pb/^{238}U$: 34.8 ± 2.2 Ma Th/U= 0.21
100 µm
z41


Figure 4

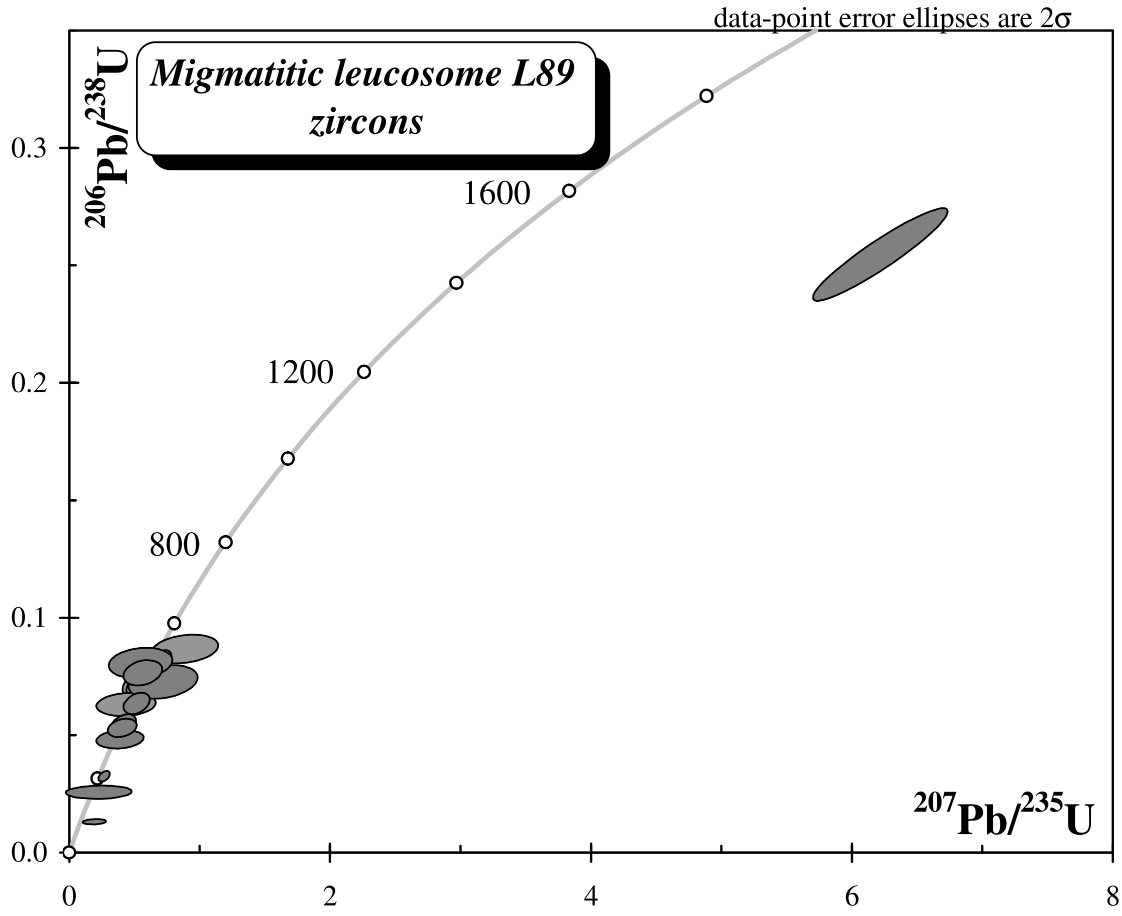
data-point error ellipses are 2σ
Migmatitic leucosome L89
zircons
206Pb/238U
207Pb/235U
0.0
0.1
0.2
0.3
0
2
4
6
8
800
1200
1600

Figure 5

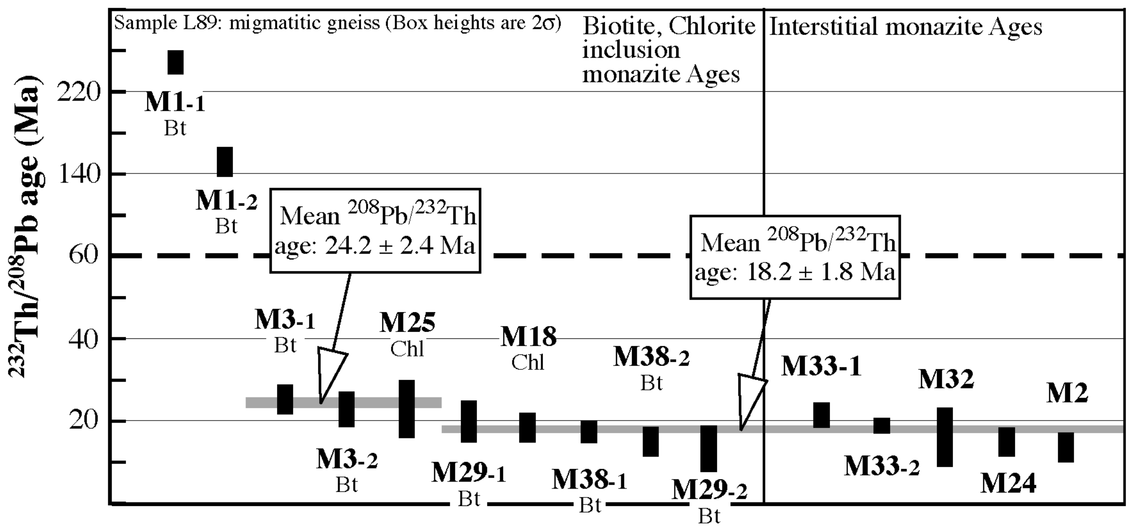

Sample L89: migmatitic gneiss (Box heights are 2σ)
Biotite, Chlorite inclusion monazite Ages
Interstitial monazite Ages
232Th/208Pb age (Ma)
220
140
60
40
20
Mean 208Pb/232Th age: 24.2 ± 2.4 Ma
Mean 208Pb/232Th age: 18.2 ± 1.8 Ma
M1-1 Bt
M1-2 Bt
M3-1 Bt
M3-2 Bt
M25 Chl
M29-1 Bt
M18 Chl
M38-1 Bt
M38-2 Bt
M29-2 Bt
M33-1
M33-2
M32
M24
M2


Figure 6

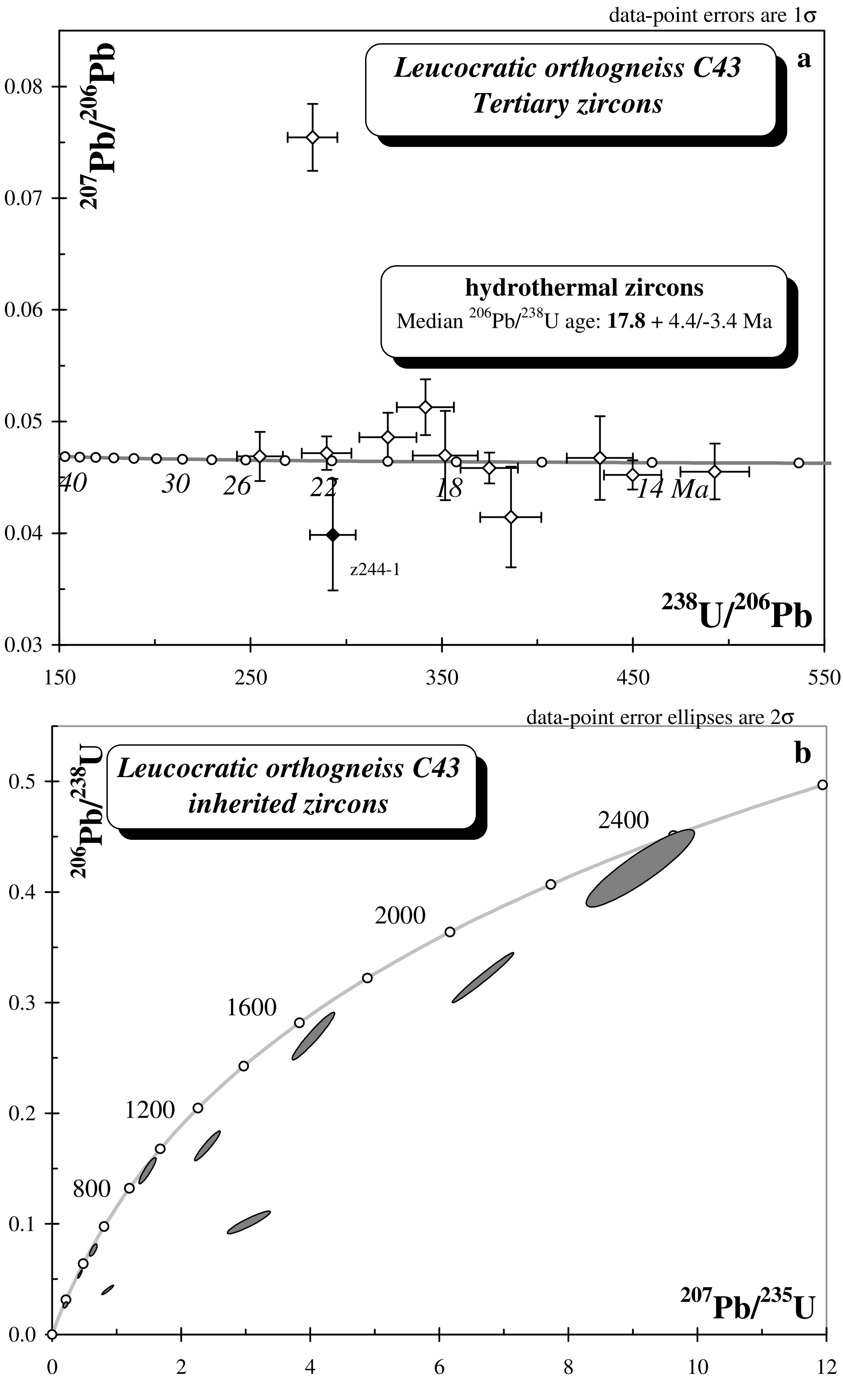
data-point errors are 1σ
Leucocratic orthogneiss C43
Tertiary zircons
a
hydrothermal zircons
Median 206Pb/238U age: 17.8 + 4.4/-3.4 Ma
207Pb/206Pb
238U/206Pb
z244-1
40
30
26
22
18
14 Ma
0.08
0.07
0.06
0.05
0.04
0.03
150
250
350
450
550
data-point error ellipses are 2σ
Leucocratic orthogneiss C43
inherited zircons
b
206Pb/238U
207Pb/235U
2400
2000
1600
1200
800
0.5
0.4
0.3
0.2
0.1
0.0
0
2
4
6
8
10
12

Figure 7

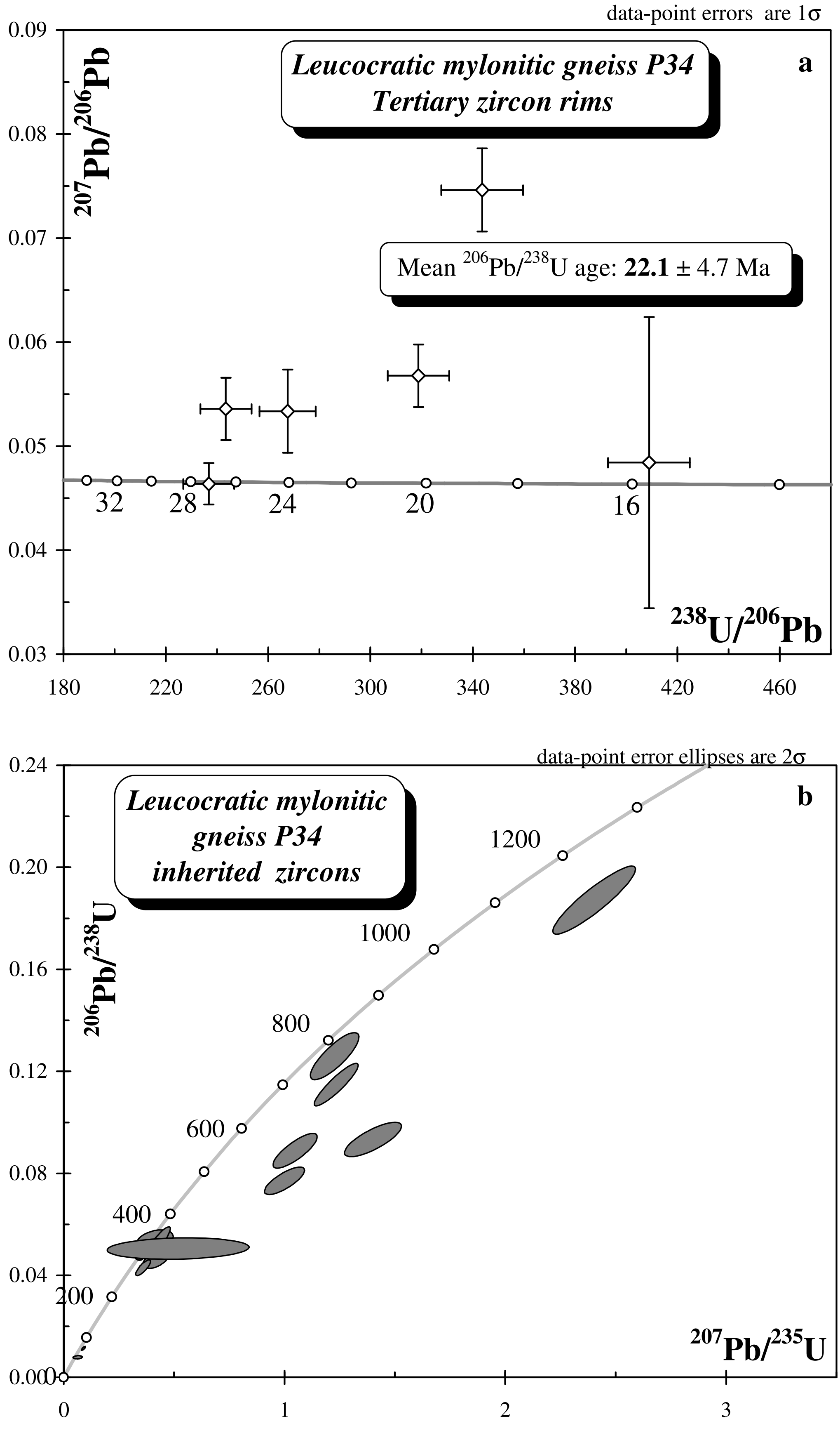

data-point errors are 1σ
Leucocratic mylonitic gneiss P34
Tertiary zircon rims
a
Mean 206Pb/238U age: 22.1 ± 4.7 Ma
207Pb/206Pb
238U/206Pb
32
28
24
20
16
0.09
0.08
0.07
0.06
0.05
0.04
0.03
180
220
260
300
340
380
420
460
data-point error ellipses are 2σ
Leucocratic mylonitic gneiss P34 inherited zircons
b
206Pb/238U
207Pb/235U
1200
1000
800
600
400
200
0
0.24
0.20
0.16
0.12
0.08
0.04
0.00
0
1
2
3


Figure 8

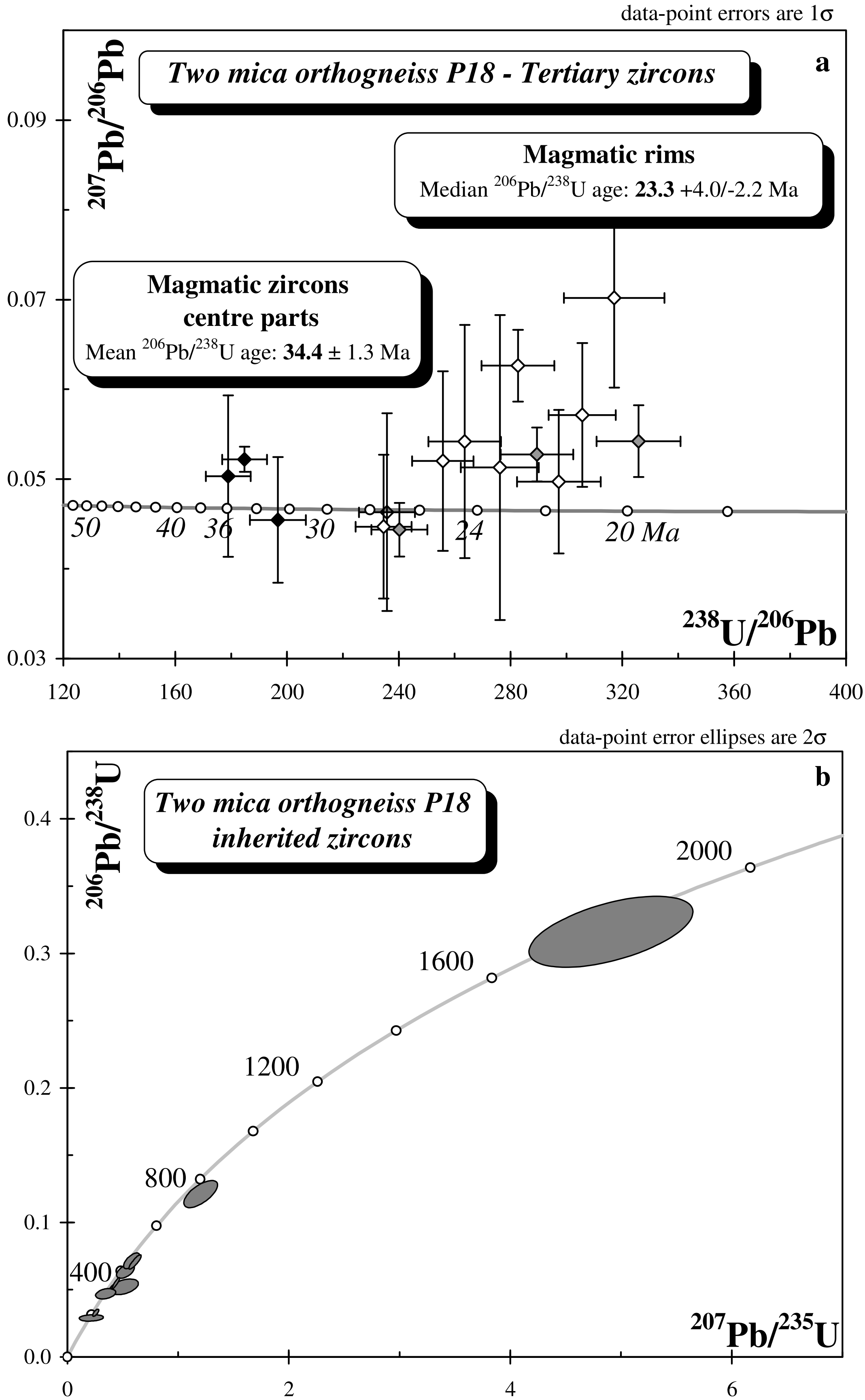

data-point errors are 1σ
Two mica orthogneiss P18 - Tertiary zircons
a
Magmatic rims
Median 206Pb/238U age: 23.3 +4.0/-2.2 Ma
Magmatic zircons
centre parts
Mean 206Pb/238U age: 34.4 ± 1.3 Ma
207Pb/206Pb
238U/206Pb
0.09
0.07
0.05
0.03
120
160
200
240
280
320
360
400
50
40
36
30
24
20 Ma
data-point error ellipses are 2σ
Two mica orthogneiss P18
inherited zircons
b
206Pb/238U
207Pb/235U
0.4
0.3
0.2
0.1
0.0
0
2
4
6
2000
1600
1200
800
400


Figure 9

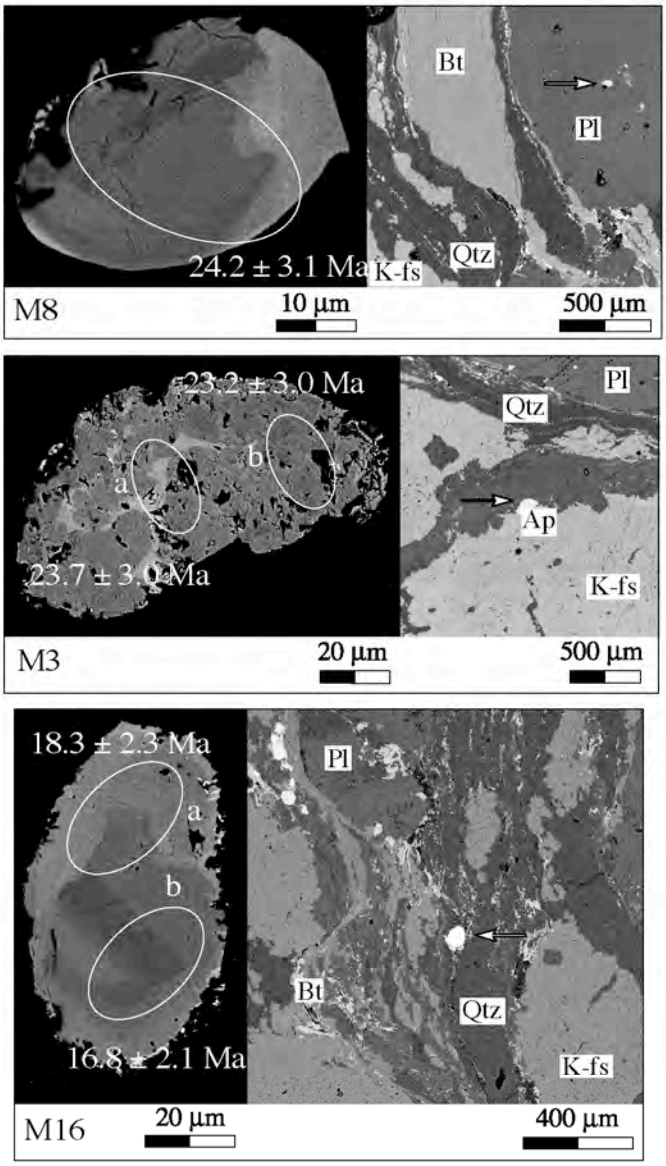
24.2 ± 3.1 Ma
Bt
Pl
Qtz
K-fs
M8
10 µm
500 µm
23.2 ± 3.0 Ma
a
b
23.7 ± 3.0 Ma
Pl
Qtz
Ap
K-fs
M3
20 µm
500 µm
18.3 ± 2.3 Ma
a
b
16.8 ± 2.1 Ma
Pl
Bt
Qtz
K-fs
M16
20 µm
400 µm

Figure 10

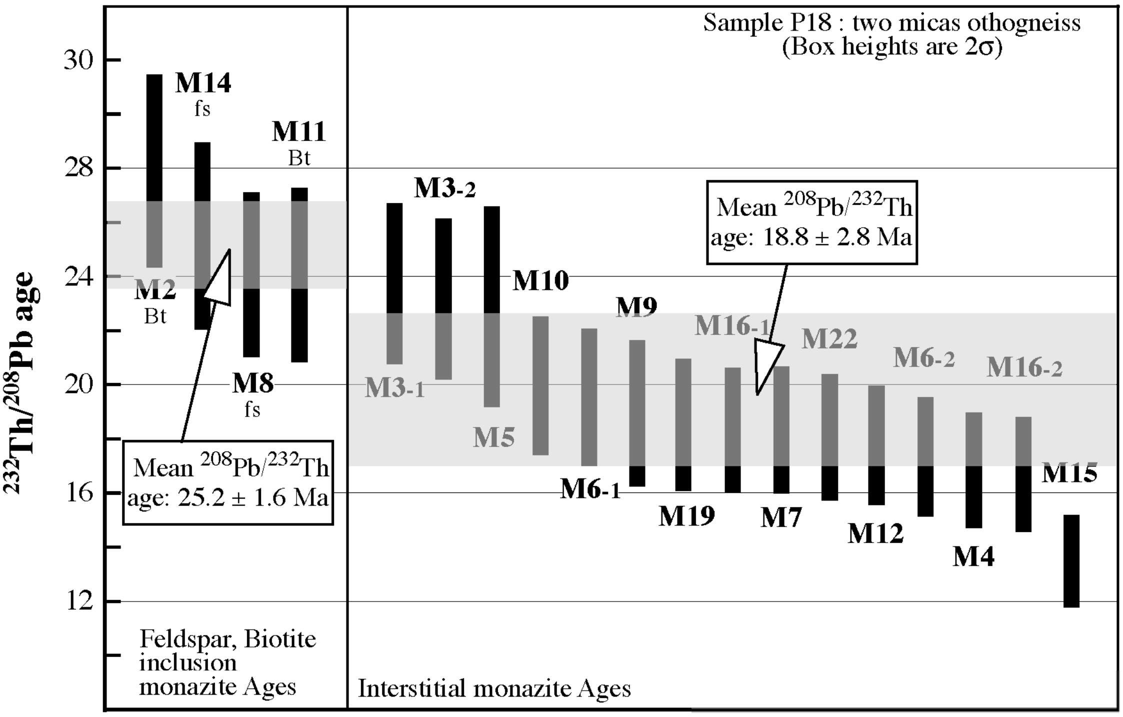
Sample P18 : two micas othogneiss
(Box heights are 2σ)
232Th/208Pb age
30
28
24
20
16
12
M14
fs
M11
Bt
M2
Bt
M8
fs
Mean 208Pb/232Th age: 25.2 ± 1.6 Ma
Feldspar, Biotite inclusion monazite Ages
M3-2
M3-1
M5
M10
M9
M6-1
M19
M16-1
M7
M22
M12
M6-2
M4
M16-2
M15
Mean 208Pb/232Th age: 18.8 ± 2.8 Ma
Interstitial monazite Ages

Figure 11

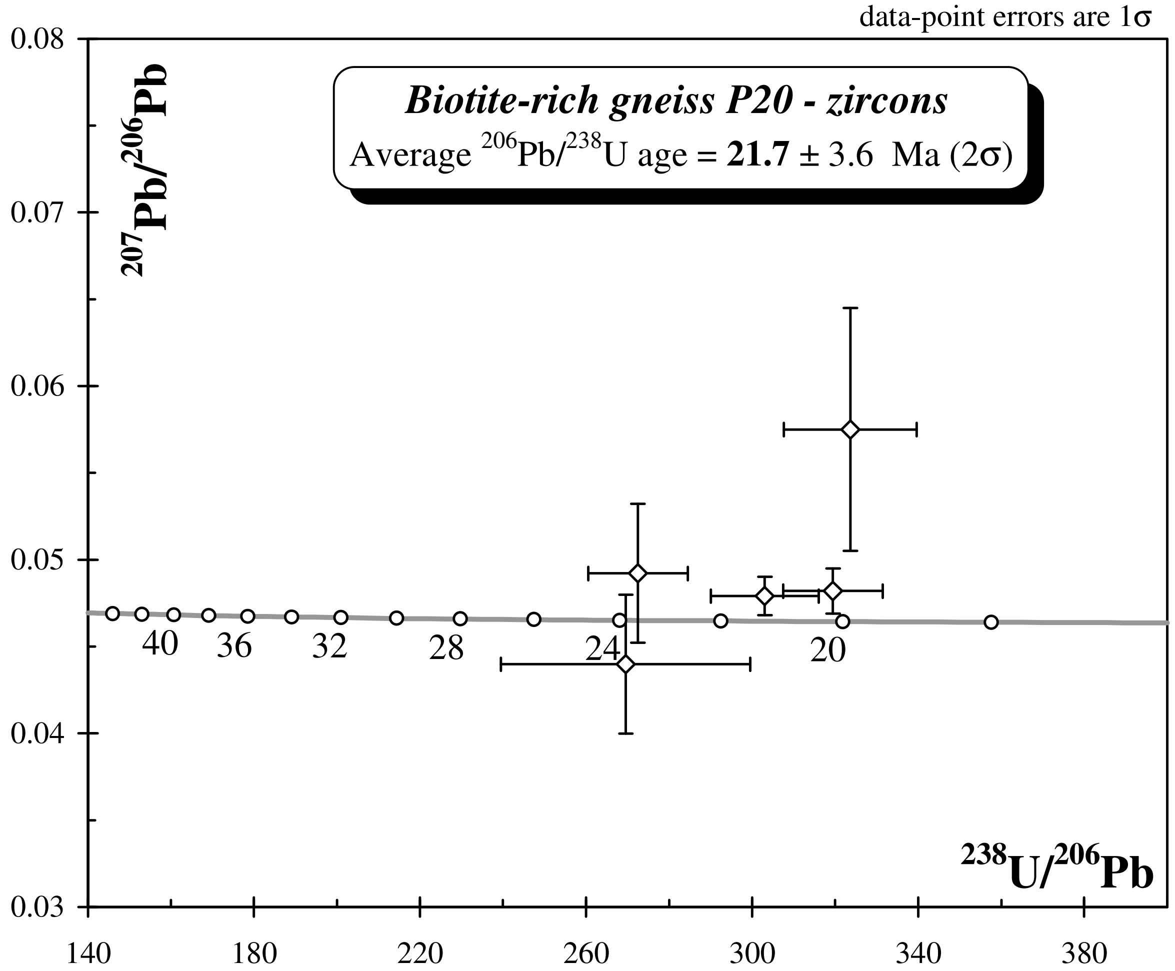
data-point errors are 1σ
Biotite-rich gneiss P20 - zircons
Average 206Pb/238U age = 21.7 ± 3.6 Ma (2σ)
207Pb/206Pb
238U/206Pb
0.08
0.07
0.06
0.05
0.04
0.03
140
180
220
260
300
340
380
40
36
32
28
24
20

Figure 12

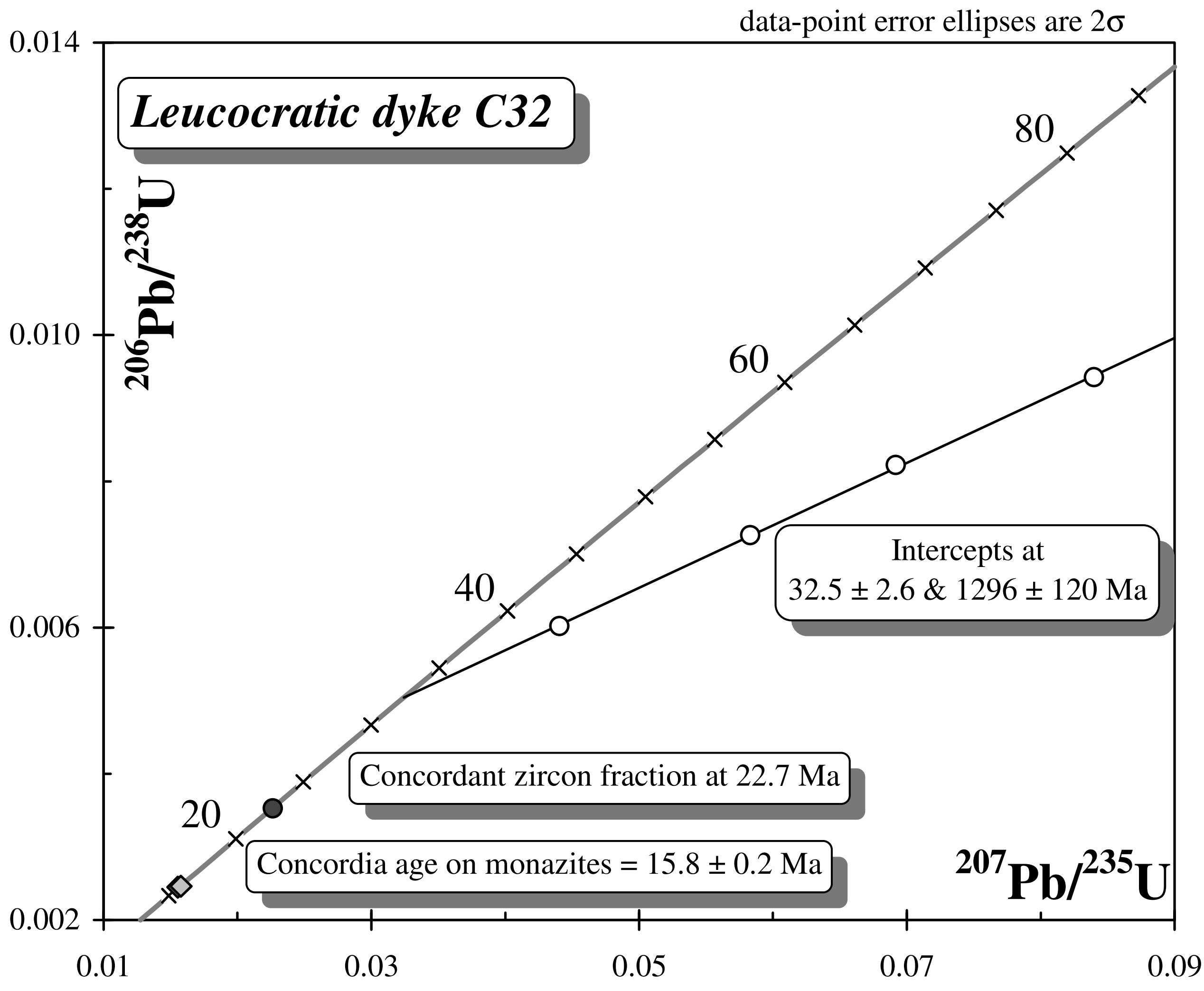
data-point error ellipses are 2σ
Leucocratic dyke C32
206Pb/238U
0.014
0.010
0.006
0.002
80
60
40
20
Intercepts at
32.5 ± 2.6 & 1296 ± 120 Ma
Concordant zircon fraction at 22.7 Ma
Concordia age on monazites = 15.8 ± 0.2 Ma
207Pb/235U
0.01
0.03
0.05
0.07
0.09

Figure 13

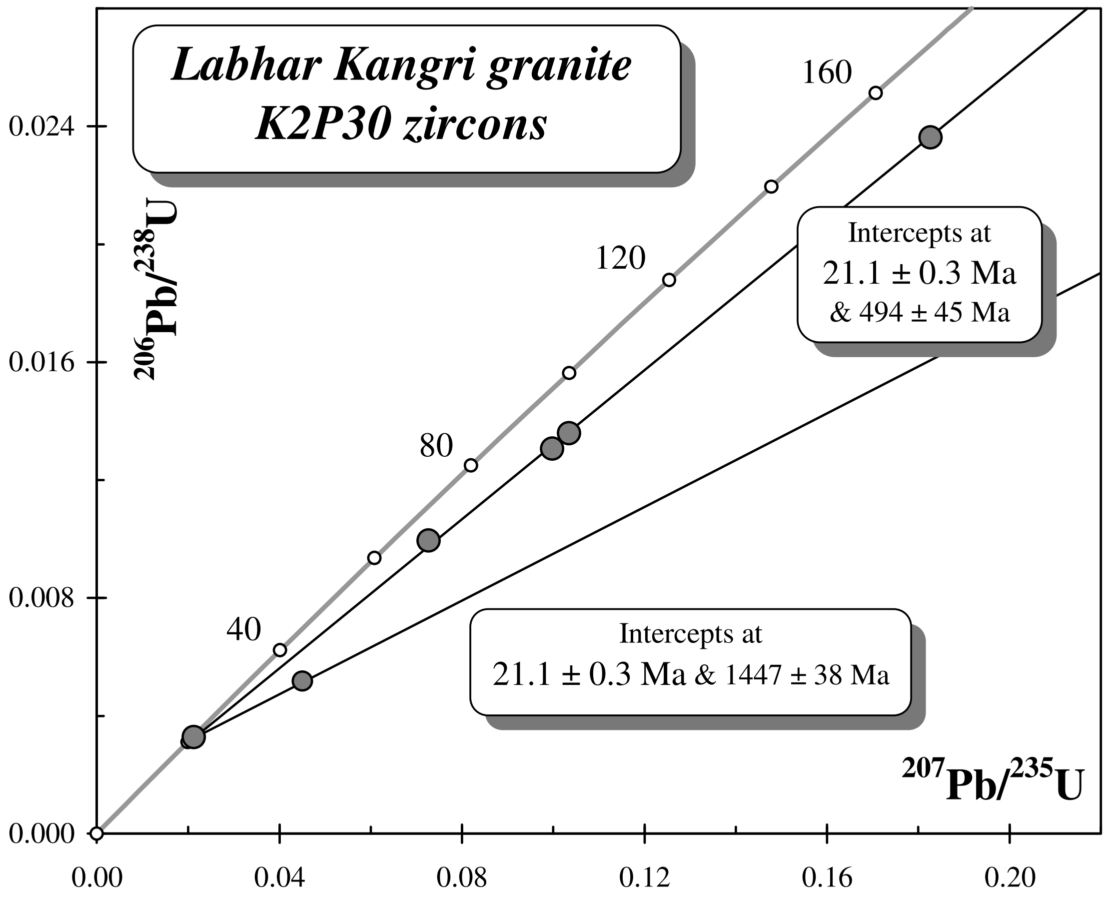
Labhar Kangri granite
K2P30 zircons
Intercepts at
21.1 ± 0.3 Ma
& 494 ± 45 Ma
Intercepts at
21.1 ± 0.3 Ma & 1447 ± 38 Ma
160
120
80
40
0.024
0.016
0.008
0.000
0.00
0.04
0.08
0.12
0.16
0.20
$^{206}Pb/^{238}U$
$^{207}Pb/^{235}U$

Figure 14

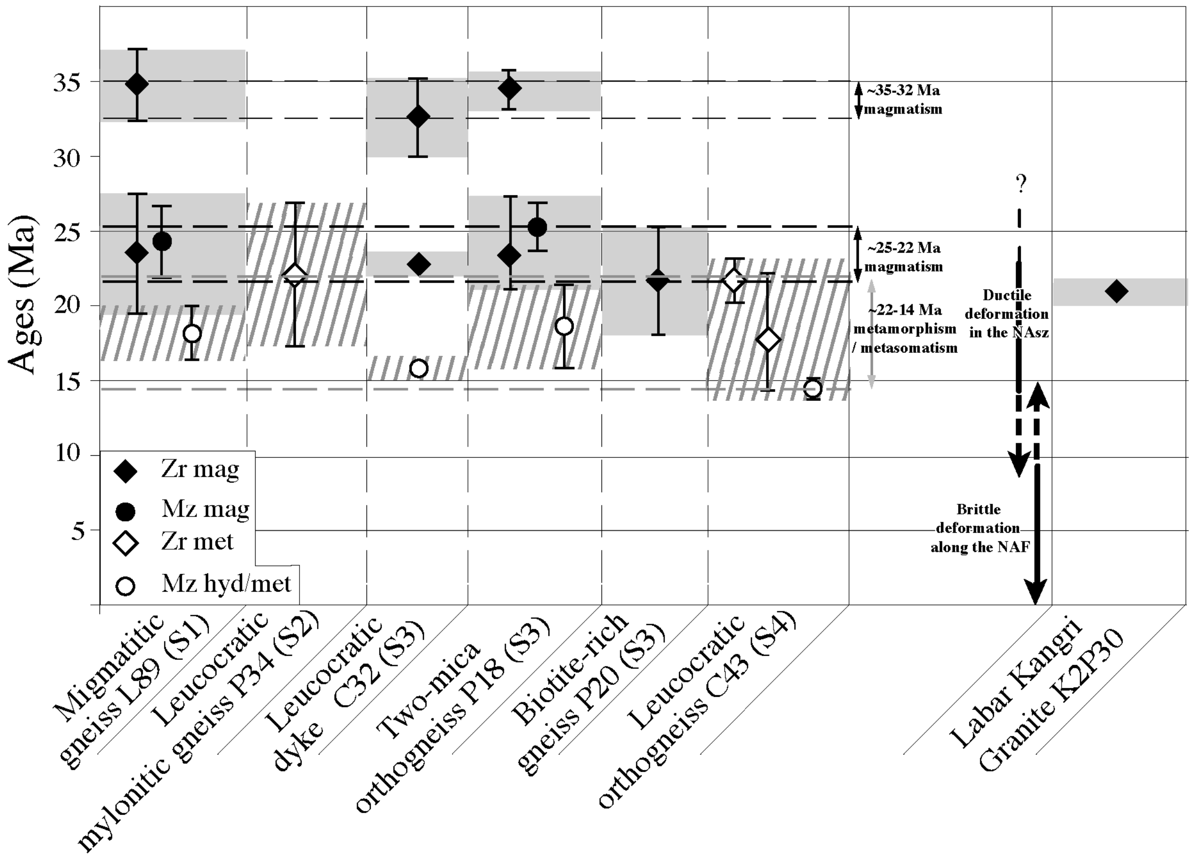
Ages (Ma)
35
30
25
20
15
10
5
~35-32 Ma magmatism
~25-22 Ma magmatism
~22-14 Ma metamorphism / metasomatism
?
Ductile deformation in the NAsz
Brittle deformation along the NAF
Zr mag
Mz mag
Zr met
Mz hyd/met
Migmatitic gneiss L89 (S1)
Leucocratic mylonitic gneiss P34 (S2)
Leucocratic dyke C32 (S3)
Two-mica orthogneiss P18 (S3)
Biotite-rich gneiss P20 (S3)
Leucocratic orthogneiss C43 (S4)
Labar Kangri Granite K2P30

Figure 15

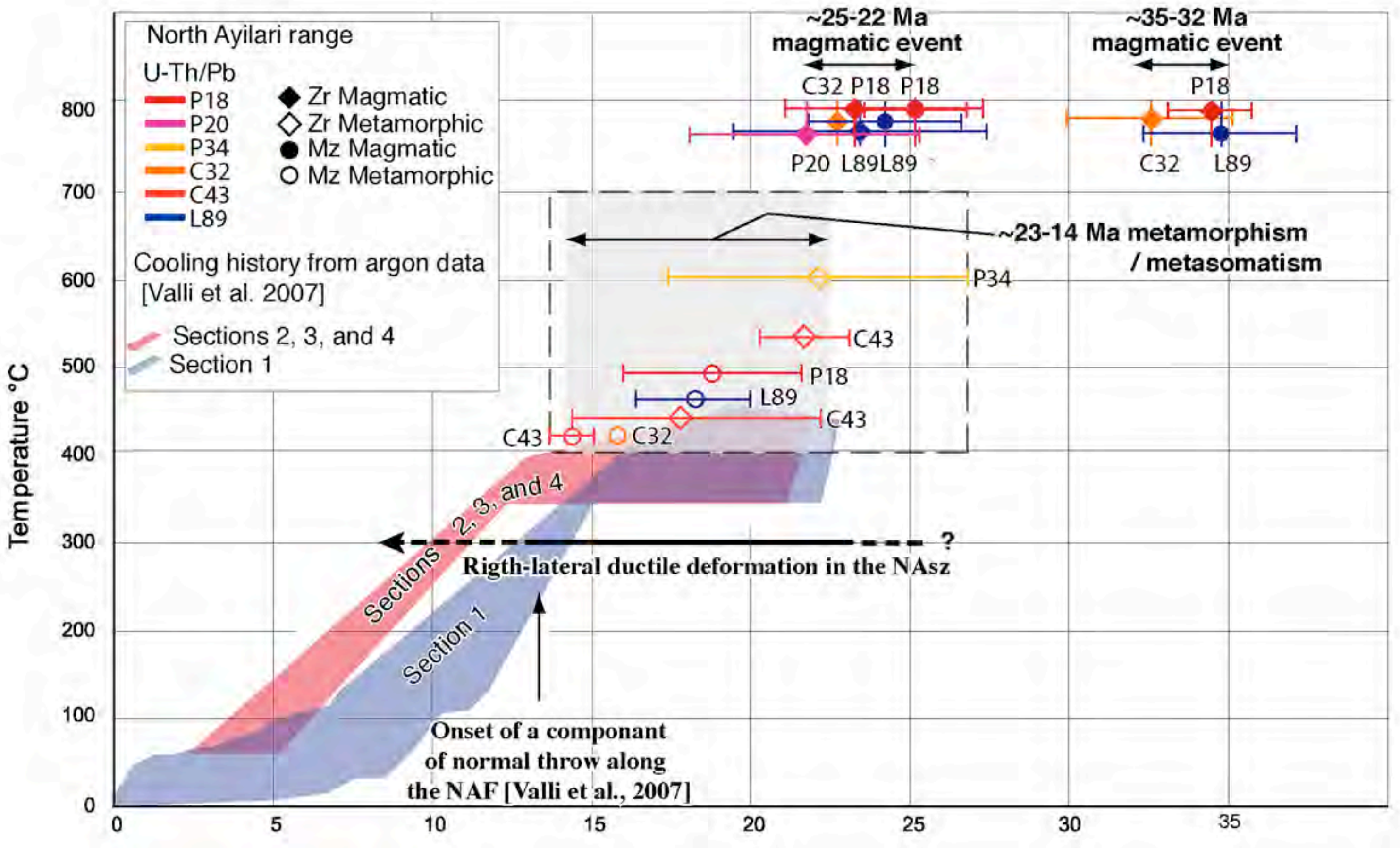

North Ayilari range
U-Th/Pb
P18
P20
P34
C32
C43
L89
Zr Magmatic
Zr Metamorphic
Mz Magmatic
Mz Metamorphic
Cooling history from argon data [Valli et al. 2007]
Sections 2, 3, and 4
Section 1
~25-22 Ma magmatic event
~35-32 Ma magmatic event
~23-14 Ma metamorphism / metasomatism
Rigth-lateral ductile deformation in the NAsz
?
Onset of a componant of normal throw along the NAF [Valli et al., 2007]
Temperature °C
0
100
200
300
400
500
600
700
800
0
5
10
15
20
25
30
35

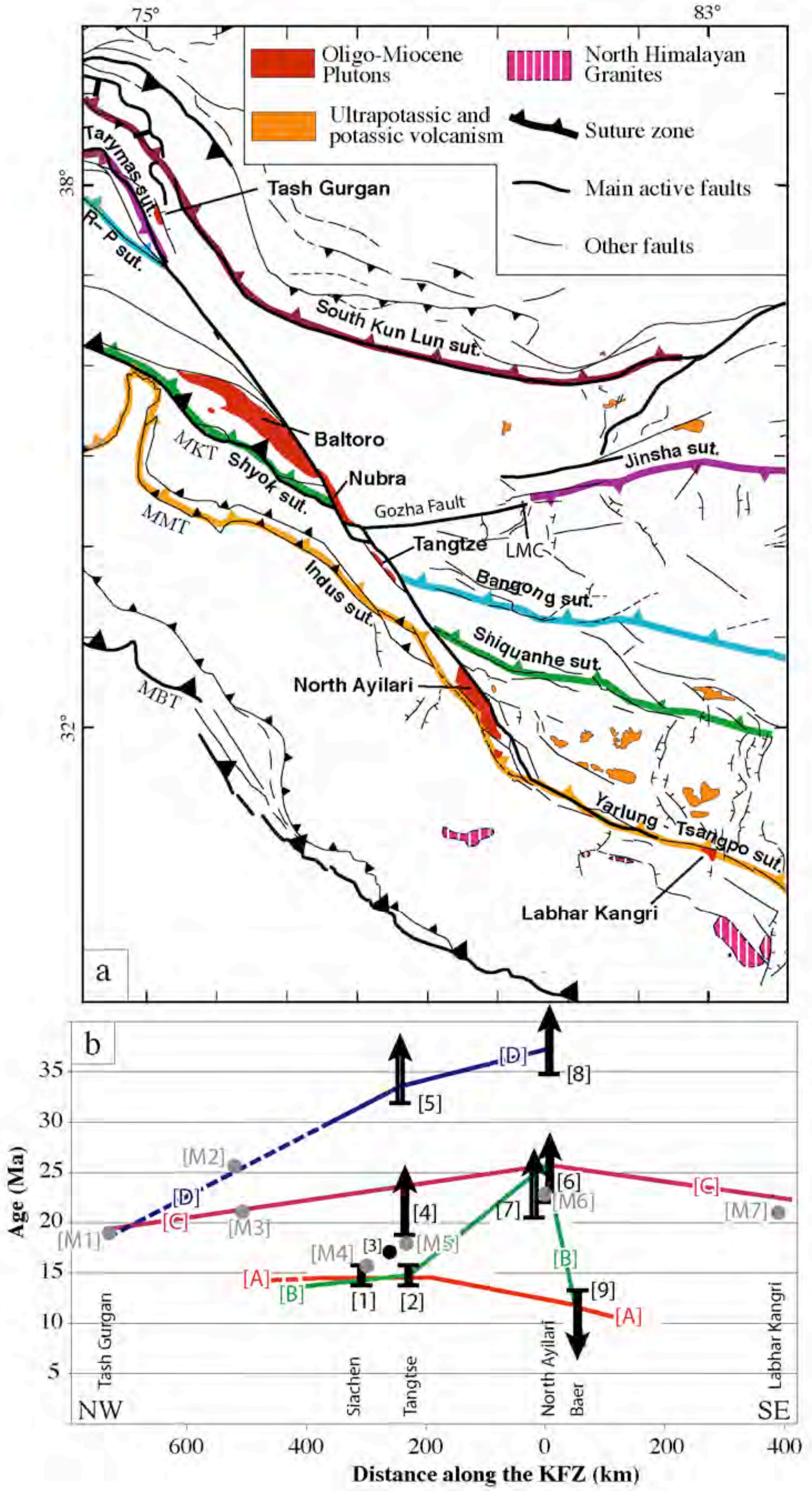

75°
83°
38°
32°
Oligo-Miocene Plutons
North Himalayan Granites
Ultrapotassic and potassic volcanism
Suture zone
Main active faults
Other faults
Tarymas sut.
R- P sut.
Tash Gurgan
South Kun Lun sut.
Baltoro
MKT
Shyok sut.
Nubra
Gozha Fault
Jinsha sut.
MMT
Tangtze
LMC
Bangong sut.
Indus sut.
Shiquanhe sut.
North Ayilari
MBT
Yarlung - Tsangpo sut.
Labhar Kangri
a
b
Age (Ma)
Distance along the KFZ (km)
NW
SE
Tash Gurgan
Siachen
Tangtse
North Ayilari
Baer
Labhar Kangri
[A]
[B]
[C]
[D]
[M1]
[M2]
[M3]
[M4]
[M5]
[M6]
[M7]
[1]
[2]
[3]
[4]
[5]
[6]
[7]
[8]
[9]

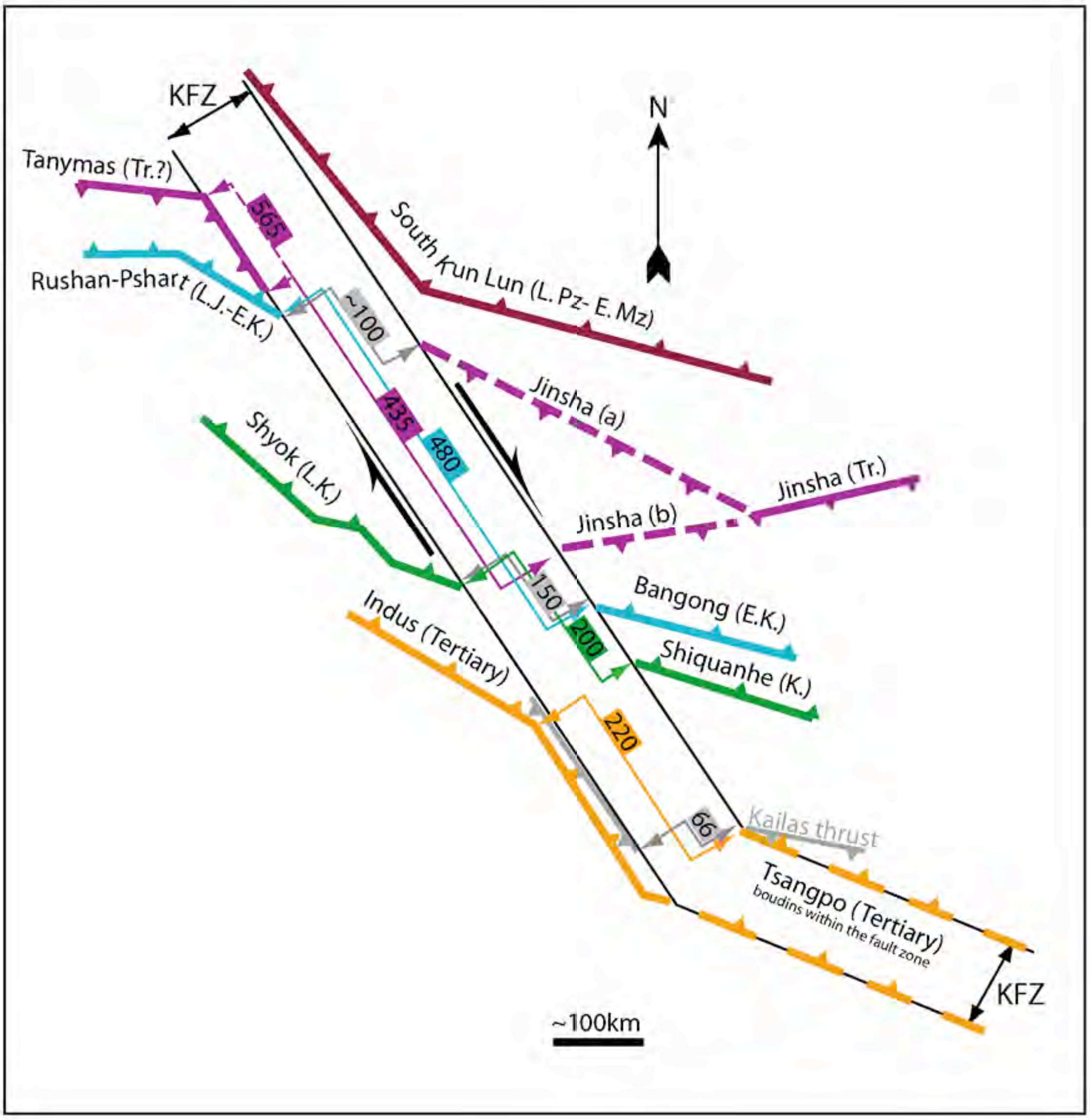

KFZ
N
Tanymas (Tr.?)
565
Rushan-Pshart (L.J.-E.K.)
South Kun Lun (L. Pz- E. Mz)
~100
Jinsha (a)
435
480
Shyok (L.K.)
Jinsha (Tr.)
Jinsha (b)
150
Bangong (E.K.)
200
Shiquanhe (K.)
Indus (Tertiary)
220
66
Kailas thrust
Tsangpo (Tertiary)
boudins within the fault zone
KFZ
~100km